How Could the Aegean Sea Be Affected After Chemical Tanker Collisions in the Strait of Çanakkale (Dardanelles)?

Hasan Bora USLUER1*

¹T.R. Galatasaray University, Maritime Vocational School, 34220, Ortaköy-Beşiktaş/İstanbul, Turkiye.

*Corresponding Author email: hbusluer@gsu.edu.tr

Abstract

Today's technology and requirements directly affect human needs. According to the International Maritime Organization - IMO, more than 90% of all needs in the world are transported by Maritime Transportation, and ships have a very important role in this regard. It is known that most of the maritime and producing countries are interested in energy transportation and that these kinds of transportation modes are very important for the development of countres. In this context, the navigation in important passages and canals around the world affects both human life and the marine environment. The Straits of Istanbul and Çanakkale, which are major parts of the Turkish Straits Sea Area-TSSA, are undoubtedly important natural waterways. If precautions are not taken, especially after an accident that may occur in the Çanakkale Strait, pollution will reach the Aegean Sea due to currents. The study describes insights into pollution impacts and prevention activities.

Keywords

Turkish Straits Sea Area(TSSA), Strait of Çanakkale (Dardanelle), Marine Pollution Simulation, Strategy of Maritime Management•

1. INTRODUCTION

The Turkish Straits Sea Area (TSSA) is an essential waterway that connects the Caspian Sea to the Mediterranean, serving as a vital route for maritime transportation. Additionally, it provides crucial habitat for marine life. The frequent passage of ships highlights the urgent need to address carbon gas emissions, which the International Maritime Organization (IMO) considers a significant concern for the shipping industry. To protect both local and global maritime environments, it is imperative to focus on key waterways that constitute the primary routes for ships serving various international ports, particularly the Turkish Straits. The Strait of Istanbul, Çanakkale, and the Sea of Marmara. The Strait's well-known names, Boshporus and Dardanelles, come from ancient times and are a great example of the world's natural seaways, such as a valley [1,2,3].

The Republic of Turkey has historically held a strategic geopolitical position, bridging the Asian and European continents through its straits. The TSSA consists of three main components: the Strait of Istanbul, the Çanakkale Strait, and the Sea of Marmara.

2 Usluer

The straits are commonly known as the Bosphorus and the Dardanelles, names that date back to ancient times, exemplifying the world's natural waterways, much like a valley. Turkish authorities no longer include "Bosphorus" and "Dardanelles" on maps featuring geographical names. The entire maritime area of the Turkish Straits falls under Turkey's sovereign territory. It is governed by the internal water regime as stipulated by the United Nations Convention on the Law of the Sea (UNCLOS).

The TSSA is a crucial corridor for energy transportation, offering the safest and most convenient route between the Mediterranean and the Black Sea. Since 1936, the Turkish Straits have been managed in accordance with the Montreux Convention, which establishes treaty obligations.



Figure 1: Turkish Strait Sea Area Overview (5)

The Turkish Straits are home to a diverse range of marine life, but they have also been subjected to heavy traffic from marine creatures and vessels for centuries. In recent years, there has been a notable increase in the types and quantities of hazardous cargo transported by the Black Sea coastal states and the Central Asian Turkic Republics, which are environmentally connected to the sea. This increase has also led to larger ships with greater tonnage passing through the Straits. Advancements in technology have contributed to a rise in the number of ships navigating these waters, heightening the risk of environmental and security threats for the Turkish Straits Marine Area and the surrounding residential regions due to hazardous materials in transit. The high density of maritime traffic in the Turkish Straits makes navigation challenging. Accidents, negligence, and other factors frequently result in oil spills during ship operations, leading to serious environmental consequences. One study simulated the potential pollution from a ship the size of the Independent tanker, which was involved in a significant marine accident in the Strait of Istanbul (Bosphorus) in 1979. The study aimed to predict how this pollution would spread to the Aegean Sea. In recent years, the TSSA has emerged as a significant trade route, gaining increased importance due to the emphasis placed on energy transportation and the movement of oil, petroleum products, and chemicals by developed nations. Turkey's unique geography experiences all four seasons, leading to distinct climatic effects. It offers special conditions for both marine and terrestrial environments, featuring diverse atmospheric and oceanographic conditions and rich plant and animal diversity.

2. THE STRAIT OF CANAKKALE MARINE SCIENCE STATUS

The Strait of Çanakkale, a unique feature of the Turkish Strait Maritime Area (TSSA), is nearly 20 nautical miles longer than the Strait of Istanbul. Its natural structure, morphology, and geographical characteristics significantly differ from those of the Strait of Istanbul, making it an intriguing subject for study. The Strait of Çanakkale represents 22.56% of the TSSA and exhibits a determined northeast-southwest current and wind direction. The strait's spatial significance is particularly evident in the narrow sections between Biga and the Gallipoli Peninsula, as well as in the northern and southern regions, where it reaches an average depth of 55 to 90 meters. [6,7,8,9]



Figure 2: The Strait of Çanakkale and 1915 Çanakkale Bridge [10]

The narrowest point between Kilitbahir and Çanakkale is only 1,300 meters wide, while the widest point, between the shores of Intepe and Domuz Dere, spans a significant 8,135 meters. The TSSA plays a crucial role in sea currents in this area. The primary current is the surface current that flows from the Black Sea to the Aegean Sea via the Sea of Marmara. Additionally, an undercurrent originates from the first layer of the Mediterranean Sea and flows through the Aegean Sea toward the Sea of Marmara [11,12,13].

3. COLLISION EFFECTS AFTER TANKER ACCIDENT ON THE STRAITS OF ÇANAKKALE AND HOW IT'S IMULATE?

The incident called the most critical accident in the Turkish Straits occurred on November 15, 1979, and involved a collision between the tanker M/T Independenta and the vessel M/V Evriali. The accident took place in front of Haydarpaşa Port. Following the collision, M/T Independenta leaked over 30,000 tons of crude oil into the Marmara Sea, resulting in an estimated 100,000 tons of pollution. This significant amount of oil severely impacted the Strait of Istanbul and the Sea of Marmara, raising serious concerns about the long-term environmental consequences. The search and rescue operations, fire extinguishing efforts, and environmental cleanup took approximately two months. Tragically, the accident claimed the lives of 42 sailors and resulted in many injuries. In addition to the human toll, the explosion caused by the collision inflicted damage on the coastline of the Anatolian side and affected settlements up to 6 kilometers away [12,13].



Figure 3: M/T Independenta Disaster photos after collision

In designing the study, the goal was to gain insights by simulating the potential damage to the Aegean Sea in the event of an accident similar to the Independenta tanker incident in the Strait of Çanakkale. To achieve this, the dimensions of the Independenta tanker were incorporated into the simulation as a reference for the ship's specifications. Additionally, chemical cargoes transported from Black Sea ports were included to ensure the simulation accurately reflects current conditions.

Following a leakage incident at coordinates 40° 24.133 N, 026° 41.882 E, near Gallipoli, the leak reached the Aegean Sea by time t+27 [11].

4 Usluer



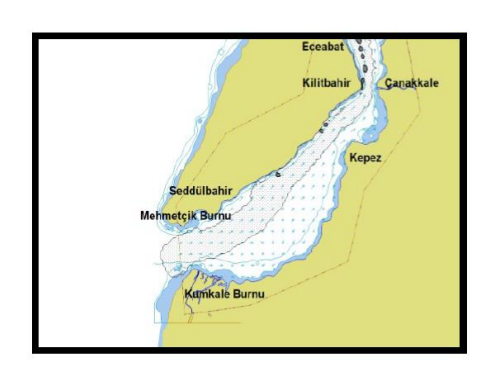
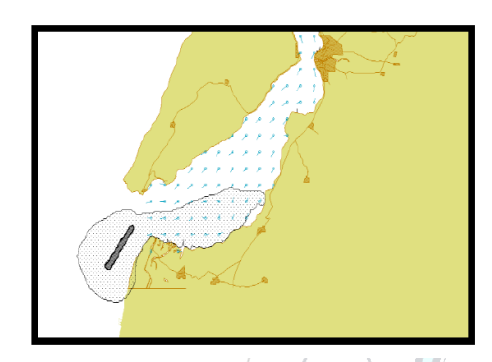


Figure 4: The oil spilled in front of Gallipoli

Oil leakage began due to grounding at 40° 11.832' N, 026° 23.466' E, in front of Cape Nara, and reached the Aegean Sea at t+24 hours.



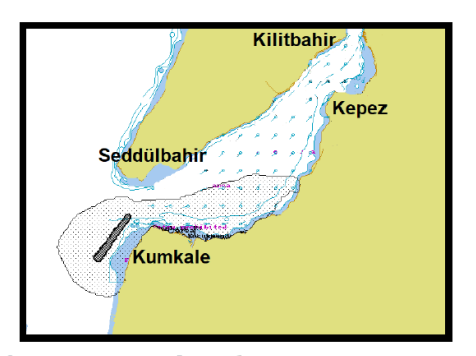


Figure 5: The oil spilled at the point of Nara

The oil leak began due to a grounding accident at 40° 08.815 N, 026° 23.570 E, near Çanakkale, and reached the Aegean Sea at time t+24 [12,13].

4. RESULTS

A thorough examination of the Strait of Çanakkale reveals a concerning probability of accidents, as highlighted by historical accident statistics. Notably, regions between Gelibolu and Çardak, Cape Nara, Kilitbahir, Çanakkale, Kumkale, and İntepe are critically vulnerable. Pollution issues are particularly alarming in the waters between Gallipoli and Çardak, extending to Cape Nara, where contaminants are seeping into the Aegean Sea, exacerbating environmental degradation. This study underscores that if a tanker incident occurs without prompt intervention, the pollution effects can escalate significantly over time. The challenges of addressing oil spills are particularly acute in the narrowest sections of the strait, such as Nara-Eceabat and Kilitbahir-Çanakkale, where strong currents complicate response efforts. Immediate action within the first hour is essential to mitigate the damage effectively. While the 1915 bridge construction substantially benefits land traffic, the reality of potential accidents and ship-related explosions can't be ignored. To confront these dangers head-on, we must create collaborative work plans and establish clear responsibility protocols. Equally crucial is fostering coordination with our coastal neighbors, highlighting the necessity of international cooperation to preserve the integrity of our territorial waters, especially in the Aegean Sea. Acting now is vital for a cleaner and safer maritime environment.

ACKNOWLEDGMENT

The Corresponding Author gratefully acknowledge the support of Galatasaray University, Scientific Research Support Programme under grant number of SOA-2023-1162.

CONFLICT OF INTEREST STATEMENT

The author declares that there is no conflict of interest.

REFERENCES

- [1]. H.B.USLUER, The Effects of Marine Sciences on Maritime Transportation and Marine Environment at Turkish Straits, Pg.9-16, 5th INTERNATIONAL CONFERENCE ON ENVIRONMENTAL SCIENCE AND TECHNOLOGY, Bosna Herzegovina, 2019
- [2]. H.,B.,Usluer, G.B.Alkan,"Importance of the Marine Science and Charting about Environmental Planning, Management and Policies at the Turkish Straits", EJSDR European Journal of Sustainable Development Research, Pg.16-25,2016
- [3]. Usluer, H. B., Bora, A. G., & Gazioglu, C., (2022). What if the Independenta or Nassia tanker accidents had happened in the Strait of Canakkale (Dardanelle)?. *OCEAN ENGINEERING*, vol.260, 1-12.
- [4]. Usluer, H.B., Gazioğlu, C., Bora, A.G., 'Simulation of Marine Pollution from a Tanker Accident at the Çanakkale Strait (Dardanelle)' 6th INTERNATIONAL CONFERENCE ON ENVIRONMENTAL SCIENCE AND TECHNOLOGY, Belgrade, 2020
- [5]. (2018) USLUER, H.B., OĞUZÜLGEN, S., Chapter I, REMARKABLE ACCIDENTS AT THE ISTANBUL STRAIT, Oil Spill along the Turkish Straits Sea Area; Accidents, Environmental Pollution, Socio-Economic Impacts and Protection, TUDAV
- [6]. (2018) ALPAR, B., USLUER, H.B., AYDIN,Ş. , Chapter II, GEOGRAPHIC AND BATHYMETRIC RESTRICTIONS ALONG THE TURKISH STRAITS SEA AREA, Oil Spill along the Turkish Straits Sea Area; Accidents, Environmental Pollution, Socio-Economic Impacts and Protection, TUDAV
- [7]. (1996) Alpar, B., H. Yüce, and E. Doğan, 1996. Gas-charged late Quaternary sediments in Strait of Çanakkale (Dardanelles). Turkish Journal of Marine Sciences, 2(3), 155–169.
- [8]. http://www.vda.org.tr/upload/duyuru/T%C3%9CRK%20BO%C4%9EAZLARI%20DEN%C4%B0Z%20TRAK%20BO%C4%B0K%20DEN%C4%B0Z%20TRAK%20BO%C4%B0K%C4%B0K%C4%B0X%20TRAK%20BO%C4%B0K%C4%B0K%C4%B0%C4%
- [9]. Beşiktepe, Ş., Sur, H. İ., Özsoy, E., Latif, M. A., Oğuz, T., Ünlüata, Ü. (1994). The circulation and hydrography of the Marmara Sea. Progress in Oceanography, 34 (4), 285-334.
- [10]. https://www.aa.com.tr/tr/yasam/1915-canakkale-koprusunde-son-hazirliklar-yapiliyor/2535611
- [11]. Beşiktepe, Ş. T., Özsoy, E., Latif, M. A., Oğuz, T. (2000). Marmara Denizi'nin hidrografisi ve dolaşımı. B.Öztürk, M.Kadıoğlu, H.Öztürk, (Eds.), Marmara Denizi 2000 Sempozyumu Bildiriler Kitabı (s. 314-326). İstanbul: Türk Deniz Araştırmaları Vakfı (TÜDAV).
- [12]. A.G.BORA, Master Thesis, SIMULATED ACCIDENT RISK ASSESSMENT OF TANKERS CARRYING CRUDE OIL IN CANAKKALE STRAIT, 2019
- [13]. Usluer, H.B., Gazioğlu, C., Bora, A.G., "Simulation of Marine Pollution from a Tanker Accident at the Çanakkale Strait (Dardanelle)" 6th INTERNATIONAL CONFERENCE ON ENVIRONMENTAL SCIENCE AND TECHNOLOGY, Belgrade, 2020

Analysis of Solar Radiation and Remote Sensing Indices for Coastal Management in Oman

Mohammadu Bello Danbatta, Nasser Al-Azri*, Nabeel Al-Rawahi

Department of Mechanical and Industrial Engineering, College of Engineering, Sultan Qaboos University, P.O. Box 50, Muscat, Sultanate of Oman.

*Corresponding Author email: nalazri@squ.edu.om

Abstract

This study examines the seasonal variations in temperature, chlorophyll indices, and solar radiation to enhance coastal management strategies along the coast of Muscat, Oman. Temperature data, measured in Kelvin, revealed a clear warming trend from winter to summer, with mean values increasing from 299.37 K in January to 311.05 K in October. The Chlorophyll-a Index (CAI) and the Normalized Difference Chlorophyll Index (NDCI) were analyzed to assess marine productivity and vegetation health. Results showed negative CAI values in the winter months, indicating lower chlorophyll concentrations, which gradually improved by October. The NDCI remained positive across all months, with the highest mean observed in January, suggesting active photosynthetic vegetation during this period. Solar radiation, measured as All Sky Surface Shortwave Downward Irradiance (kW-hr/m2), peaked in April and July, aligning with increased temperatures and indicating maximum solar energy input during these months. This increase in solar radiation was found to significantly influence the chlorophyll indices, reflecting seasonal shifts in marine and coastal ecosystem productivity. The interrelationship between temperature, chlorophyll indices, and solar radiation highlights the complex environmental dynamics governing coastal processes in Muscat. These findings underscore the importance of integrating solar radiation data and remote sensing techniques into coastal management frameworks. Such an interdisciplinary approach can inform evidence-based strategies for mitigating environmental impacts and fostering sustainable development along Oman's coastlines.

Keywords

Coastal management, Solar Radiation, Climate Change, Oman

1. INTRODUCTION

Oman boasts a vast coastline spanning approximately 3,165 kilometers along the Arabian Sea and the Gulf of Oman, making coastal management a critical aspect of environmental stewardship in the country [1]. The coastal zones of Oman are not only vital for biodiversity and marine ecosystems but also play a significant role in supporting economic activities such as fisheries, tourism, and shipping [2]. However, these coastal ecosystems face numerous threats, including habitat degradation, pollution, overfishing, and the impacts of climate change. By integrating environmental parameters, this research aims to provide valuable insights into the complex interrelations that govern coastal processes in Muscat. The findings have significant implications for coastal management strategies, advocating for an interdisciplinary approach that incorporates solar radiation data and remote sensing techniques. Such methodologies can enhance our understanding of coastal dynamics, enabling evidence-based strategies that support sustainable development and mitigate the adverse impacts of environmental

changes. Effective coastal management is essential to mitigate these threats and ensure the sustainability of Oman's coastal resources for future generations.

2. STUDY AREA

The research area encompasses the coastal zone of Muscat in Oman, located at approximately 23.6345° N latitude and 58.0962° E longitude. This distinct environmental setting is characterized by a desert climate, with arid conditions prevailing year-round. Summers are characterized by high temperatures, often exceeding 40 degrees Celsius, while winters are relatively mild, with temperatures ranging between 15 and 25 degrees Celsius. Rainfall is typically low, averaging around 100 mm annually and occurring sporadically. The elevation of the Muscat coastal region varies, contributing to its diverse topography. Coastal bathymetry further complicates environmental dynamics, shaping marine ecosystems and influencing coastal processes. The study area encompasses a significant geographical area, including both coastline and adjacent land, providing ample scope for ecological investigations. As the capital city of Oman, Muscat holds considerable population and economic significance. The population of the municipality is dynamic, reflecting urbanization and economic activities. Moreover, the coastal region of Muscat plays a vital role in the country's Gross Domestic Product (GDP) through sectors such as fisheries, tourism, and maritime trade. The investigation covers a region of interest spanning 6,360.03 km².



Figure 1. Study Area of interest

3. METHODOLOGY

3.1. Satellite Imagery

The data collection for this study in the Muscat coastal region of the sultanate of Oman relies on satellite imagery from the Landsat 8 Operational Land Imager (OLI) and Thermal Infrared Sensor (TIR), obtained through the U.S. Geological Survey (USGS) Earth Explorer. Landsat 8 OLI/TIR provides a valuable dataset with distinctive spatial, spectral, and temporal characteristics, contributing to a comprehensive understanding of the study area. Spatially, Landsat 8 OLI/TIR offers a spatial resolution of 30 meters for multispectral bands, allowing for detailed mapping and analysis of land features [3]. The sensor captures data in multiple spectral bands, providing information on various surface properties. The multispectral bands range from visible to shortwave infrared, enabling the extraction of essential environmental parameters, including vegetation health, land cover, and thermal dynamics [4]. Spectrally, Landsat 8 OLI/TIR's spectral bands cover a wide range of electromagnetic wavelengths, offering a multispectral and thermal perspective of the Earth's surface. This spectral diversity enhances the capacity to discriminate between different land cover types and assess environmental conditions [5]. Temporally, Landsat 8 OLI/TIR provides a revisit time of 16 days, facilitating the acquisition of frequent and temporally dynamic data for monitoring seasonal variations and changes over time [6]. The obtained satellite imagery contributes significantly to the research's objectives by capturing the intricate ecological dynamics of the Muscat coastal region. The scenes used in this study are listed in Table 1.

8 Danbatta et al.

Table 1. Landsat 8 OLI/TIR satellite scene used

On Board Sensor	Acquisition Date	Scene Time	WRS (PATH, ROW)
OLI/TIRS	2023-01-05	06:35:01.2220310Z	(158,44)
OLI/TIRS	2023-04-03	06:34:33.9627430Z	(158,44)
OLI/TIRS	2023-07-08	06:34:10.2046779Z	(158,44)
OLI/TIRS	2023-10-04	06:34:43.5675189Z	(158,44)

3.2. Data Preprocessing

In the analysis conducted, radiometric calibration and atmospheric correction was done on all images. Radiometric calibration is done for converting the raw digital numbers obtained from satellite sensors into physically meaningful units, ensuring consistency and comparability across different acquisitions [7]. The atmospheric correction was carried out using the Fast Line-of-sight Atmospheric Analysis of Spectral Hypercubus (FLAASH) method using ENVI 5.3. This enhances the accuracy and reliability of the data derived from Landsat 8 Operational Land Imager and Thermal Infrared Sensor (OLI/TIR) imagery. This correction accounts for factors such as water vapor, aerosols, and gases, mitigating their impact on the emitted thermal radiation from the Earth's surface. The FLAASH algorithm employs radiative transfer equations to model the interactions between the atmosphere and the incoming solar and emitted thermal radiation, enabling the derivation of atmospherically corrected values [8]. The radiometric calibration and FLAASH atmospheric correction processes are pivotal steps to ensure the accuracy of the reflectance values, particularly in regions with diverse atmospheric conditions such as coastal environments. Implementing these corrections enhances the reliability of the derived information, allowing for more accurate analyses of surface and contributing to a comprehensive understanding of the environmental dynamics.

3.2.1. Normalized Difference Chlorophyll Index

The Normalized Difference Chlorophyll Index (NDCI) is primarily designed for chlorophyll assessment, its adaptability has been extended to impervious surface mapping due to its sensitivity to built-up structures.

3.2.2. Chlorophyll a Index

The Chlorophyll-a Index (CAI) is an important vegetation index designed for the estimation of chlorophyll-a concentrations in water bodies. Unlike traditional vegetation indices, CAI focuses on the spectral characteristics related to water quality. The CAI values are indicative of chlorophyll-a concentrations, with higher values suggesting higher concentrations. This ratio-based index plays a crucial role in assessing water quality and monitoring changes in chlorophyll-a levels within aquatic ecosystems.

3.2.3. Land surface Temperature

Land Surface Temperature (LST) is a crucial parameter for understanding Earth's surface energy balance and is widely used in various environmental applications. LST represents the temperature of the Earth's surface, excluding the effects of the atmosphere. Accurate estimation of LST is essential for monitoring climate, agriculture, and urban heat islands. It's important to mention that LST is influenced by various factors, including emissivity and atmospheric conditions, which may require additional corrections depending on the specific application.

4. RESULTS AND DISCUSSIONS

The RGB composite image shown in Figure 2 after processing demonstrates a notable enhancement in the precision and dependability of the radiometric data linked to the image bands. Through calibration, atmospheric distortions, sensor anomalies, and lighting differences were effectively addressed, leading to improved consistency in radiometric properties across the RGB channels. This enhancement is vital for accurate quantitative assessments, ensuring that the pixel values in the composite image better correspond to the actual surface reflectance values. The calibrated RGB composite establishes a dependable basis for further image analysis, classification, and extraction of valuable data, ultimately enhancing the accuracy and precision.



Figure 2. Radiometric calibrated and FLAASH Corrected RGB Composite

4.1. Temperature Variations

The temperature data across the four selected months (January, April, July, and October) reveal significant seasonal fluctuations as can be seen in Figure 3 and LST in Table 2. The mean temperatures in Kelvin (K) for January, April, July, and October are 299.37 K, 302.27 K, 306.23 K, and 311.05 K, respectively. This progression indicates a clear warming trend from winter to summer. January and October exhibit the lowest and highest mean temperatures, respectively.

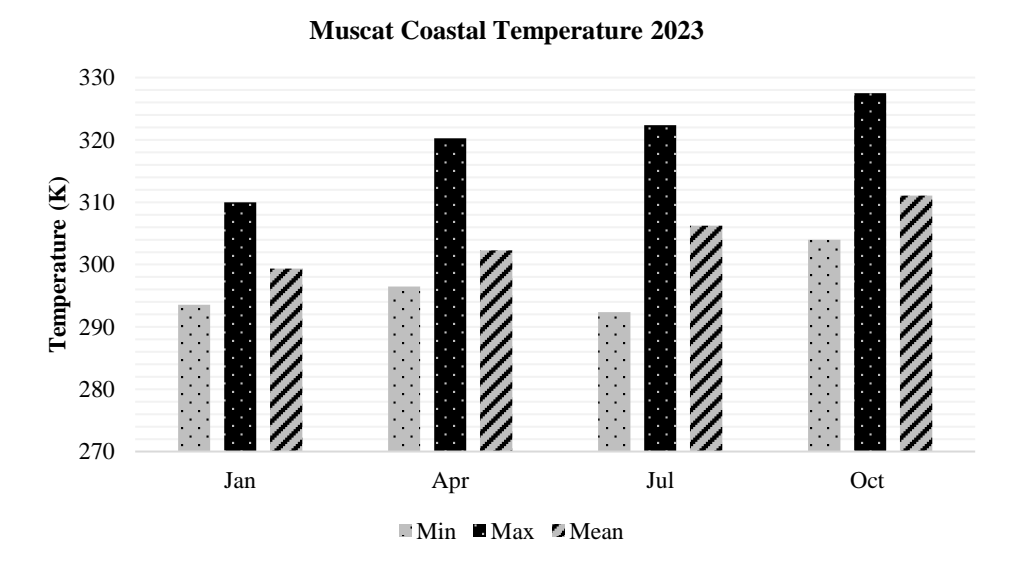
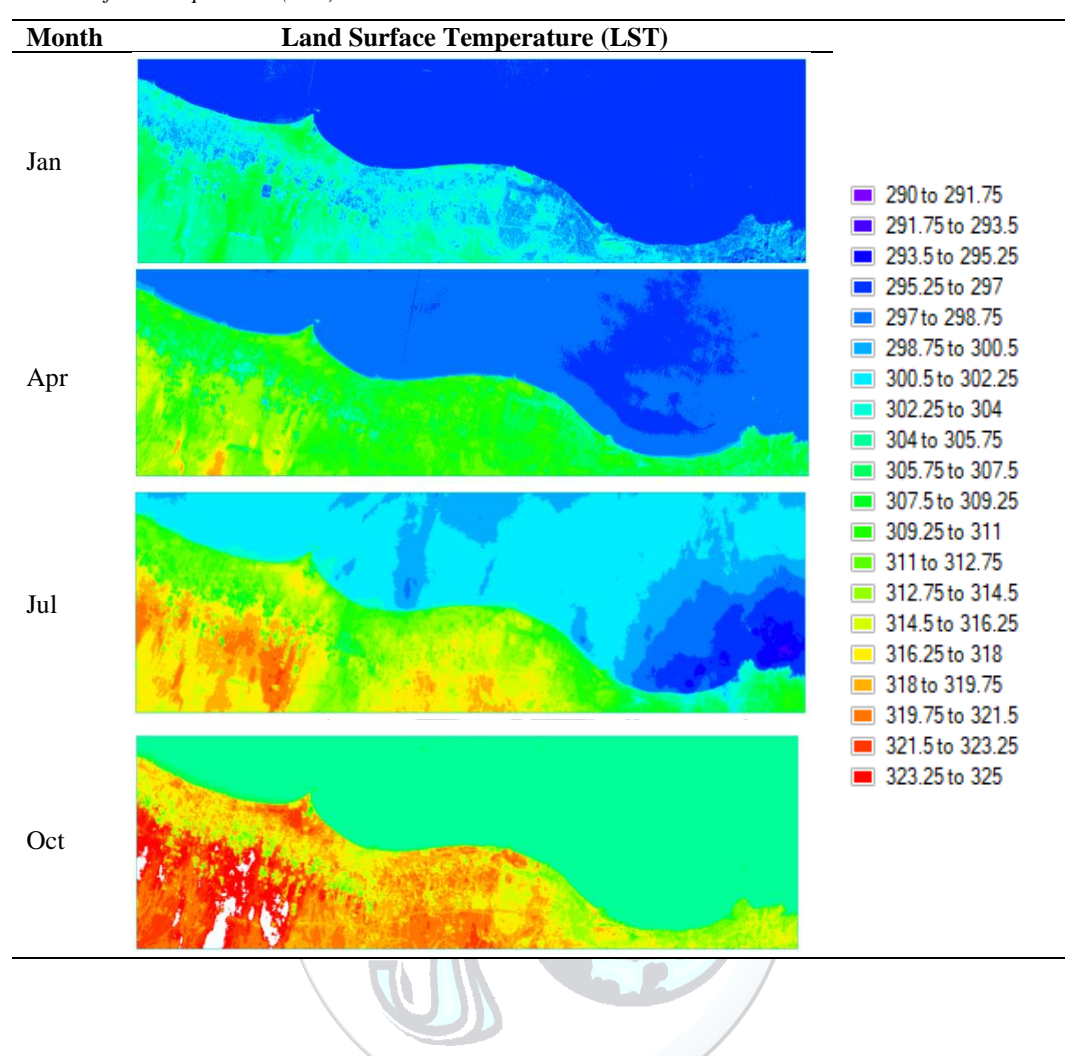


Figure 3. Temperature Variations

The standard deviations for temperature are relatively high, particularly in April (6.47 K), July (7.515 K), and October (7.2668 K), indicating substantial temperature variability within these months. This variability is less pronounced in January (3.565 K), suggesting more stable temperatures during winter.

10 Danbatta et al.

Table 2. Land Surface Temperature (LST)



4.2. Chlorophyll-a Index (CAI)

The CAI shows negative mean values in January, April, and July, with -0.347, -0.0656, and -0.055, respectively, while October exhibits a positive mean value of 0.059. Table 3 and Figure 4 shows the CAI and Standard deviation and mean of the CAI respectively. The substantial negative CAI in January and the relatively low standard deviation (0.555) indicate lower chlorophyll-a concentrations and less variability in winter. In contrast, October's positive mean value and moderate standard deviation (0.265) suggest higher chlorophyll-a concentrations with increased variability during the autumn months.

Muscat Coastal CAI & NDCI 2023

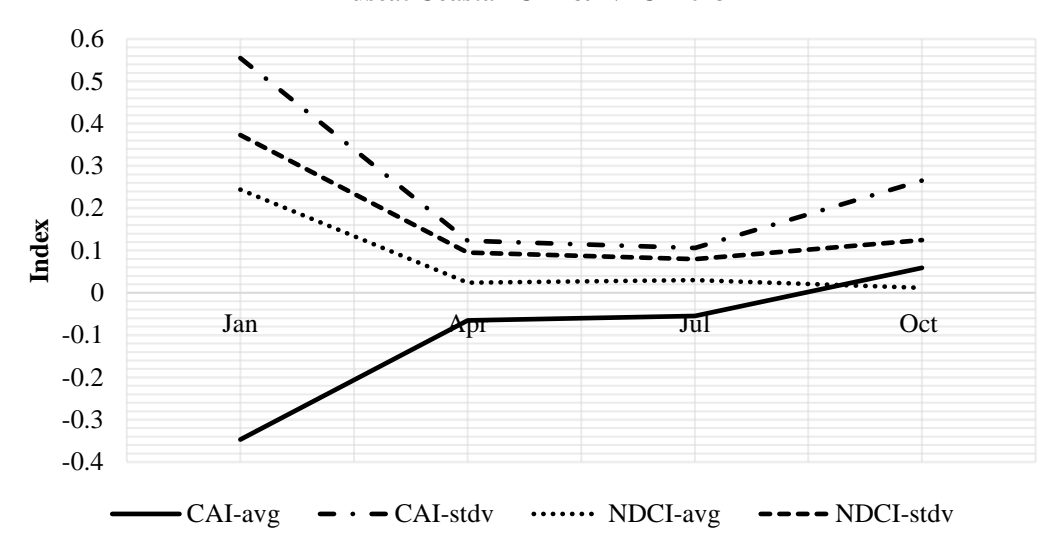
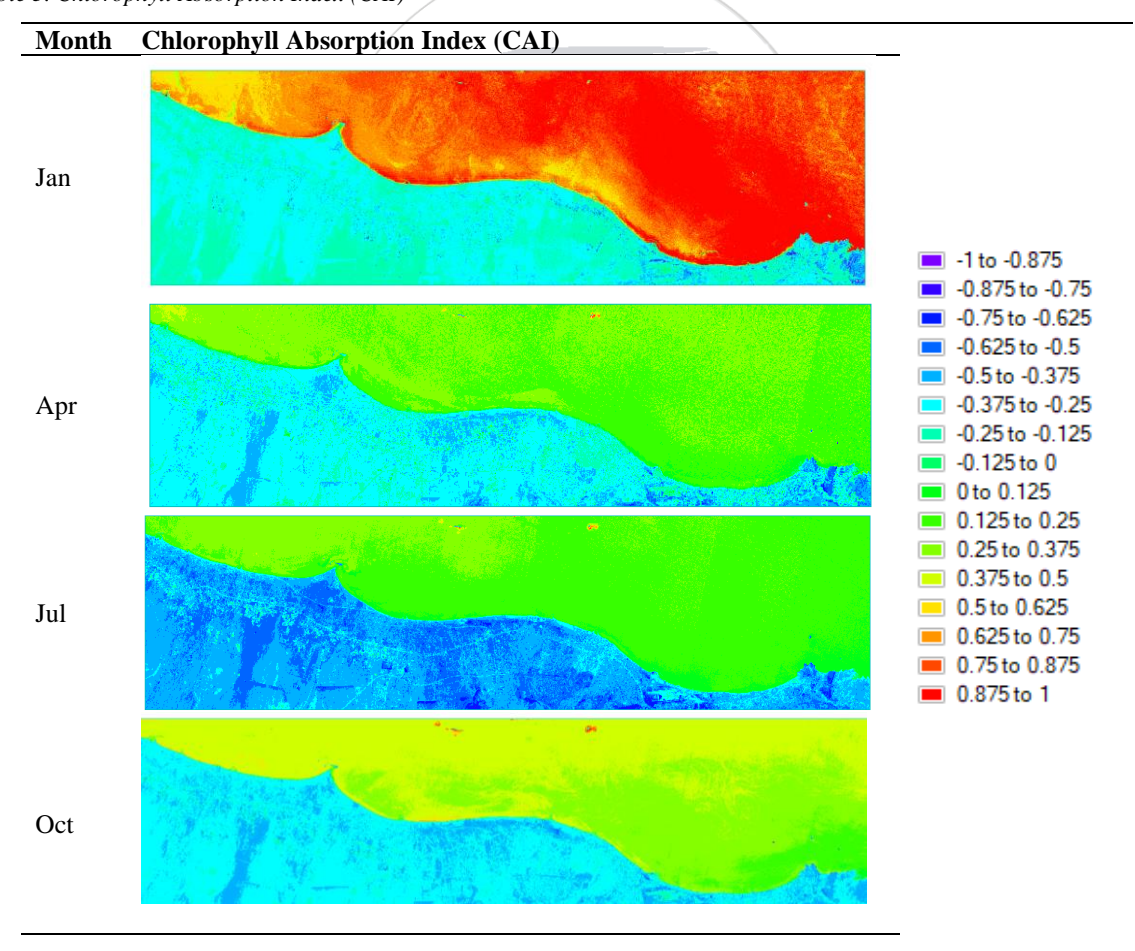


Figure 4. Standard Deviation and Mean of CAI & NDCI

Table 3. Chlorophyll Absorption Index (CAI)

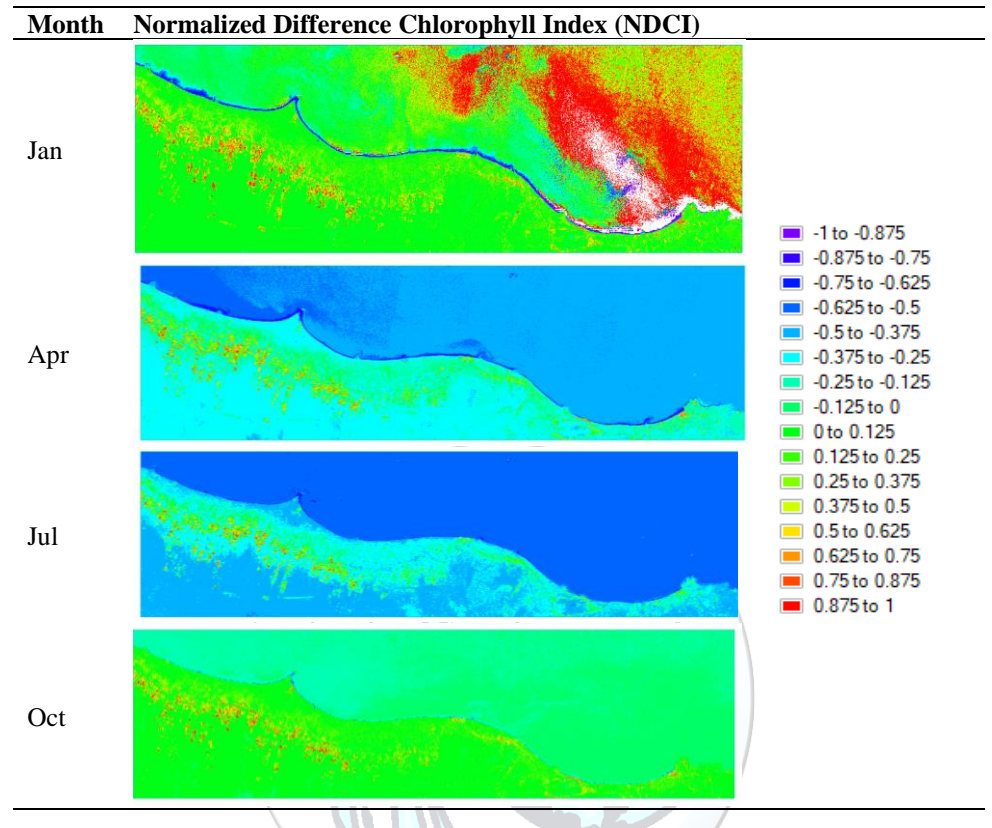


12 Danbatta et al.

4.3. Normalized Difference Chlorophyll Index (NDCI)

The NDCI values show positive means across all months, indicating the presence of chlorophyll and hence photosynthetically active vegetation. The highest mean NDCI is observed in January (0.244), with a standard deviation of 0.373, suggesting high chlorophyll levels but with considerable variability. April, July, and October exhibit lower mean NDCI values of 0.024, 0.03, and 0.0117, respectively, with corresponding standard deviations of 0.095, 0.0796, and 0.12464, indicating relatively stable chlorophyll concentrations during these months.

Table 4. Normalized Difference Chlorophyll Index (NDCI)



4.4. Solar Radiation

The analysis of All Sky Surface Shortwave Downward Irradiance, measured in kW-hr/m^2, shows the highest mean values in April (6.3577 kW-hr/m^2) and July (6.1835 kW-hr/m^2), suggesting maximum solar radiation during these months. January has the lowest mean irradiance (4.2190 kW-hr/m^2), consistent with the winter season when solar angles are lower. The standard deviation values indicate that April (1.0150 kW-hr/m^2) and July ($0.92797 \text{ kW-hr/m^2}$) have higher variability in solar radiation compared to January (0.5522 kW-hr/m^2) and October (0.6886 kW-hr/m^2). Figure 5 depicts the variation of the solar radiation, the max, min and Mean.

Jan Apr Jul Oct Min - - · Max Mean

All Sky Surface Shortwave Downward Irradiance 2023

Figure 5. Solar Radiation

4.5. Interrelationships

The observed seasonal trends in temperature, CAI, NDCI, and solar radiation illustrate the complex interplay of environmental factors influencing coastal processes in Muscat. The increase in temperature from January to October corresponds with increased solar radiation, particularly in April and July. This rise in solar radiation likely drives the higher temperatures and affects the chlorophyll indices.

The CAI and NDCI variations further highlight seasonal shifts in marine productivity and vegetation health. The negative CAI in the early months suggests lower chlorophyll-a concentrations, potentially due to cooler temperatures and lower sunlight. As temperatures rise and solar radiation increases, the CAI improves, indicating enhanced chlorophyll-a presence. The NDCI values follow a similar trend, supporting the seasonal growth and activity of photosynthetic organisms.

5. CONCLUSION

This study has elucidated the seasonal dynamics of temperature, chlorophyll indices, and solar radiation along the coast of Muscat, Oman, underscoring their interconnected roles in shaping coastal ecosystem health and productivity. The documented warming trend from winter to summer, alongside fluctuations in chlorophyll concentrations and solar radiation, highlights the complexities inherent in coastal environmental processes. The findings indicate that increased temperatures correlate with enhanced marine productivity, as reflected by the positive trends in chlorophyll indices, particularly during the warmer months. The results emphasize the critical need for integrating solar radiation data and advanced remote sensing techniques into coastal management frameworks. Such integration can provide a comprehensive understanding of the factors influencing marine ecosystems, paving the way for more effective management practices. By considering the interrelationships among temperature, chlorophyll indices, and solar radiation, policymakers and coastal managers can develop strategies that not only address current environmental challenges but also anticipate future changes driven by climate variability.

CONFLICT OF INTEREST STATEMENT

The authors declare that there is no conflict of interest.

REFERENCES

- [1] Al-Farsi, Y. M., Al-Yahyai, M., Al-Zadjali, M. S., & Waly, M. I. (2018). Meteorological variables and distribution of monthly and annual rainfall in different regions of Oman. Atmosphere, 9(1), 31.
- [2] Al-Shaqsi, S., Kumar, L., & Duan, Z. (2015). Bathymetric prediction using Landsat 8 OLI and SRTM data in coastal waters: A case study in Muscat, Oman. Geocarto International, 30(3), 298-311.
- [3] Wulder, M. A., White, J. C., Loveland, T. R., Woodcock, C. E., Belward, A. S., Cohen, W. B., ... & Herold, M. (2015). The global Landsat archive: Status, consolidation, and direction. Remote Sensing of Environment, 185, 271-283.

14 Danbatta et al.

[4] Roy, D. P., Wulder, M. A., Loveland, T. R., Woodcock, C. E., Allen, R. G., Anderson, M. C., ... & Scambos, T. A. (2014). Landsat-8: Science and product vision for terrestrial global change research. Remote Sensing of Environment, 145, 154-172.

- [5] Markham, B. L., Barsi, J. A., Kaita, E., Malla, R., & Thome, K. (2014). Spectral band adjustment of landsat-8 operational land imager (OLI) to landsat-7 enhanced thematic mapper plus (ETM+). Remote Sensing, 6(10), 10306-10330.
- [6] Kovalskyy, V., Roy, D. P., Zhang, H. K., Ju, J., & Vermote, E. F. (2019). Assessment of time series MODIS, MERIS, Landsat, and SPOT NDVI retrievals against year-matched GPP flux tower observations in South Florida, USA. Remote Sensing in Ecology and Conservation, 5(1), 16-31.
- [7] Chander, G., Markham, B. L., & Helder, D. L. (2009). Summary of current radiometric calibration coefficients for Landsat MSS, TM, ETM+, and EO-1 ALI sensors. Remote Sensing of Environment, 113(5), 893-903.
- [8] Hulley, G. C., Hook, S. J., & Abbott, E. A. (2014). An approach for the atmospheric correction of Landsat-8 thermal infrared (TIR) data and the generation of a consistent TIR land surface temperature (LST) record. Remote Sensing, 6(11), 11193-11212



Exploring the Impact of Solar Radiation on Environmental Dynamics in Oman Normalized Difference Vegetation Index (NDVI)

Mohammadu Bello Danbatta, Nasser Al-Azri*, Nabeel Al-Rawahi

Department of Mechanical and Industrial Engineering, College of Engineering, Sultan Qaboos University, P.O. Box 50, Muscat, Sultanate of Oman.

*Corresponding Author email: nalazri@squ.edu.om

Abstract

This study delves into the intricate relationship between solar radiation and vegetation health in Oman, focusing on the Normalized Difference Vegetation Index (NDVI) as a key indicator of ecosystem resilience. Utilizing advanced remote sensing techniques and comprehensive climate data, we analyze seasonal variations in solar radiation and NDVI across different ecological landscapes. Our findings reveal distinct seasonal patterns, with solar radiation peaking in April and July, while NDVI values fluctuate, reflecting the vegetation's response to varying environmental conditions. The analysis highlights that high solar irradiance alone does not guarantee robust vegetation health, emphasizing the role of other factors such as temperature and water availability. In particular, summer months exhibit signs of vegetation stress despite high irradiance levels, suggesting the influence of heat and potential drought conditions. This research provides actionable insights for effective environmental management and agricultural practices in Oman, advocating for strategies that consider both solar radiation dynamics and additional climatic factors. By integrating these findings, policymakers and stakeholders can develop informed interventions to enhance vegetation resilience and mitigate the adverse impacts of climate change on Oman's ecosystems. This study contributes to the broader discourse on climate change adaptation, underscoring the necessity of incorporating solar radiation metrics into holistic environmental assessments and sustainability strategies.

Keywords

Oman, Normalized Difference Vegetation Index (NDVI), Solar Radiation

1. INTRODUCTION

Solar radiation, comprising direct and diffuse sunlight, is a primary driver of ecological processes, influencing vegetation growth, photosynthesis, and energy balance in terrestrial ecosystems [1]. The Normalized Difference Vegetation Index (NDVI), derived from satellite imagery, quantifies the density and health of vegetation cover based on the differential reflectance of near-infrared and red wavelengths [2]. NDVI serves as a proxy for vegetation biomass, productivity, and ecosystem functioning, making it a valuable tool for monitoring environmental changes and assessing ecosystem health [3].

Understanding the dynamics of solar radiation and NDVI is crucial for elucidating ecosystem responses to climate variability and anthropogenic disturbances in Oman. Changes in solar radiation patterns, driven by atmospheric

16 Danbatta et al.

processes and land surface characteristics, can influence temperature regimes, precipitation patterns, and ecological productivity [4]. Variations in NDVI reflect changes in vegetation cover, phenology, and species composition, providing insights into ecosystem resilience and vulnerability to environmental stressors [5].

By exploring the intricate relationship between solar radiation and NDVI dynamics in Oman, this study aims to unravel the underlying mechanisms driving environmental changes and ecosystem responses. Through advanced remote sensing techniques and climate modeling, we seek to analyze the spatiotemporal variations in solar radiation and NDVI across diverse ecological landscapes, shedding light on the complex interactions shaping Oman's ecosystems.

The introduction section of this paper sets the stage by providing background information, contextualizing the research objectives, and delineating the scope of the study. It aims to establish the significance of investigating the impact of solar radiation on environmental dynamics in Oman using the Normalized Difference Vegetation Index (NDVI).

The primary purpose of this study is to explore the intricate relationship between solar radiation and environmental dynamics in Oman, with a specific focus on utilizing the Normalized Difference Vegetation Index (NDVI) as a key indicator of vegetation health and ecosystem resilience. By leveraging advanced remote sensing techniques and sophisticated climate models, the research seeks to conduct a comprehensive analysis of the spatiotemporal variations in solar radiation and NDVI across diverse ecological landscapes in Oman.

2. STUDY AREA

Oman boasts a rich diversity of ecological landscapes. Along Oman's coastlines, diverse marine ecosystems such as coral reefs, seagrass beds, and mangrove forests thrive. These ecosystems are crucial for supporting marine biodiversity and enhancing coastal resilience. The coastal regions are significant not only for their ecological value but also for their role in sustaining local fisheries and protecting shorelines from erosion [6]. Inland, the landscape transitions into arid and semi-arid desert regions characterized by sparse vegetation and extreme temperatures. Despite the harsh conditions, oases and wadis (valleys) within these deserts provide vital habitats for unique flora and fauna. These areas illustrate the resilience and adaptability of desert ecosystems [7]. The mountainous areas of Oman, including the Al Hajar Mountains, exhibit a range of microclimates due to elevation gradients. These regions support diverse vegetation types, from Mediterranean-like forests and juniper woodlands to alpine meadows. The varied climatic conditions across different elevations create unique habitats for a wide array of plant and animal species[8].

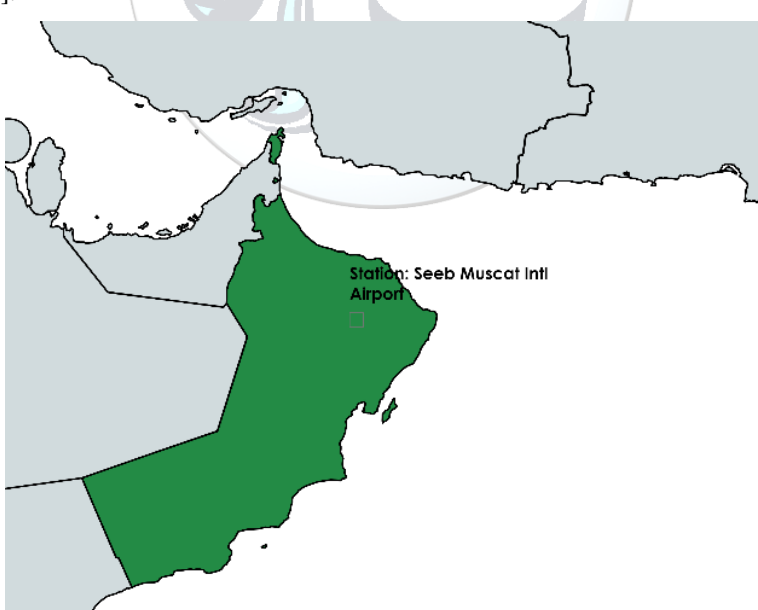


Figure 1 Sultanate of Oman

The study area is selected based on several criteria to ensure a representative sampling of Oman's diverse ecological landscapes, the Seeb international airport location is selected as depicted in figure 1, the key considerations for the location included:

I. Geographical Diversity, capturing variations in environmental conditions and vegetation cover, the most urban region of Oman, encompassing coastal areas, mountainous regions, and desert landscapes. This geographical

diversity ensures that the study accounts for the wide range of ecological and climatic conditions present across location habitat by populous.

- II. Ecological Significance, area with high biodiversity and unique ecosystems were prioritized to gain insights into the impact of solar radiation on environmental dynamics in key ecological hotspots. Allowing for a deeper understanding of solar radiation influences vegetation health and ecosystem resilience in the urban landscape.
- III. Accessibility and Data Availability, the region has readily available satellite imagery, meteorological data, and ground truth information to facilitate comprehensive and accurate assessments. This criterion ensures that the study is based on robust data, enhancing the reliability of the findings regarding solar radiation patterns and NDVI variations.

The selection of these diverse ecological landscapes reflects Oman's environmental heterogeneity and ensures comprehensive coverage of the factors influencing solar radiation dynamics and NDVI variations. Aiming to provide a holistic understanding of how solar radiation interacts with various ecological settings, informing strategies for environmental management and sustainable development in Oman.

3. METHODOLOGY

3.1. NDVI Data Source

For this study, remote sensing data was acquired from multiple sources to capture the spatiotemporal variations in solar radiation and NDVI across Oman's diverse ecological landscapes. Satellite imagery, obtained from platforms such as Landsat and Sentinel, provided high-resolution data suitable for monitoring vegetation dynamics and solar radiation patterns over large geographic extents [9][10].

3.2. Solar Radiation Data Source

In conjunction with remote sensing data, climate data from NASA POWER were utilized to supplement the analysis and provide contextual information on meteorological parameters such as temperature, precipitation, and humidity.

4. RESULTS AND DISCUSSIONS

The plot depicted in Figure 2 shows the All Sky Surface Shortwave Downward Irradiance for four months, Analyzing the Solar Radiation at the month of January, Minimum of 2.65 kW-hr/m², Maximum of 5.32 kW-hr/m², Mean of 4.22 kW-hr/m² and Standard Deviation of 0.55 kW-hr/m² is recorded. In January, the mean irradiance is the lowest among the months observed, which correlates with winter conditions where solar insolation is typically reduced. The relatively low standard deviation suggests consistent irradiance values throughout the month. In April a Minimum of 3.64 kW-hr/m², Maximum of 7.75 kW-hr/m², Mean of 6.36 kW-hr/m² and Standard Deviation of 1.02 kW-hr/m² is recorded. The month of April has the highest mean irradiance, indicating a transition to summer with increased solar exposure. The high standard deviation reflects greater variability in solar irradiance, likely due to changes in weather patterns and atmospheric conditions during spring. Furthermore in the month of July a Minimum of 3.01 kW-hr/m², Maximum of 7.35 kW-hr/m², Mean of 6.18 kW-hr/m² and Standard Deviation of 0.93 kW-hr/m². the month of July maintains high irradiance levels, similar to April, but slightly lower on average. The substantial standard deviation indicates notable variability, potentially influenced by summer weather fluctuations such as cloud cover and humidity. Lastly, in October Minimum of 3.63 kW-hr/m², Maximum of 6.24 kW-hr/m², Mean of 5.28 kW-hr/m² and Standard Deviation of 0.69 kW-hr/m² is recorded. In October, irradiance levels decrease as the season transitions to autumn. The mean irradiance is higher than in January but lower than in April and July. The standard deviation indicates moderate variability, suggesting relatively stable but slightly variable solar conditions.

Danbatta et al.

All Sky Surface Shortwave Downward Irradiance((kW-

hr/m^2) SQUAL AND SQUAL A

Figure 2 All Sky Surface Shortwave Downward Irradiance

Max

The plot depicted in Figure 3 shows Analysis of NDVI. In the month of January, a Minimum of 0.0671, Maximum of 0.195, Mean of 0.1144 and Standard Deviation of 0.0249 is recorded. The mean NDVI in January indicates moderate vegetation health. The low standard deviation suggests consistent vegetation conditions across the region, which aligns with the relatively stable irradiance during this period. Furthermore in April, a Minimum of 0.0749, Maximum of 0.1839, Mean of 0.1136 and Standard Deviation of 0.0247. In April, the NDVI mean is similar to January, indicating stable vegetation conditions. Despite the high irradiance variability, the vegetation health appears to be steady, which could be due to favorable spring growth conditions compensating for irradiance fluctuations. In the month of July, a Minimum of 0.0673, Maximum of 0.1848, Mean of 0.0983 and Standard Deviation 0.0239 is documented. The month of July shows the lowest mean NDVI, suggesting stressed vegetation. This could be due to high temperatures and potential drought conditions, despite the high mean irradiance. The lower standard deviation reflects a uniform response of vegetation to the harsh summer conditions. Lastly in October, a Minimum of 0.0712, Maximum of 0.265, Mean of 0.1067 and Standard Deviation of 0.0342 is recorded. The month of October exhibits a higher NDVI variability, with the highest standard deviation among the months. This indicates diverse vegetation responses possibly due to the mix of residual summer heat and the onset of cooler autumn conditions, which can create varied microclimates and vegetation responses.

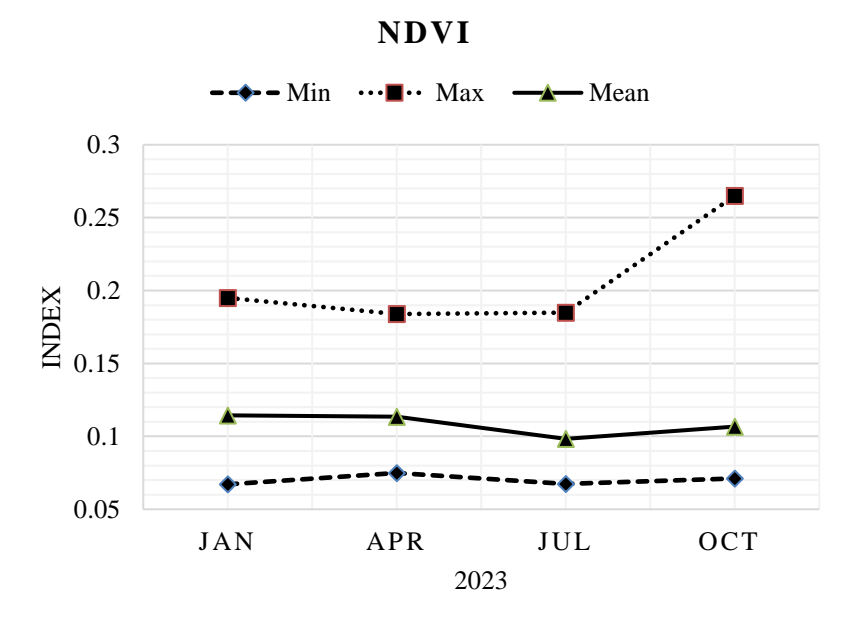


Figure 3 NDVI

The correlation between irradiance and NDVI highlights the complex interplay between solar radiation and vegetation health across seasons. High Irradiance Months (April and July), these months experience high solar irradiance, yet the NDVI response differs. While April maintains stable NDVI, July shows signs of vegetation stress. This suggests that high solar irradiance alone

does not guarantee healthy vegetation; other factors like temperature and water availability play critical roles. Moderate Irradiance months (October and January), these months have lower irradiance levels with moderate to high NDVI values. This indicates that lower solar radiation can still support healthy vegetation if other conditions are favorable.

Understanding the seasonal dynamics of solar irradiance and vegetation health is crucial for effective environmental management and agricultural practices. The findings suggests the month of April to be Optimal for vegetation growth due to high irradiance and stable NDVI, indicating robust vegetation health. This period is ideal for planting and intensive agricultural activities. However in the month of July the High irradiance coupled with low NDVI suggests potential heat and water stress on vegetation. Measures such as irrigation and shading may be necessary to support vegetation health during this period. The variability in NDVI in October suggests a need for targeted interventions based on specific local conditions. This period can be used to prepare for the upcoming winter by ensuring vegetation is healthy and resilient. Stable conditions in January with moderate NDVI indicate a period of maintenance. Agricultural activities should focus on protecting vegetation from potential cold stress and preparing for the spring growth period.

5. CONCLUSION

This analysis of Sky Surface Shortwave Downward Irradiance and NDVI across four months reveals significant seasonal variations in both irradiance and vegetation health. The highest irradiance occurs in April, with July also showing high levels, yet the NDVI in July indicates stressed vegetation, possibly due to extreme temperatures or drought conditions. October presents the highest variability in NDVI, suggesting diverse vegetation responses to environmental factors during this month. Understanding these dynamics is crucial for optimizing agricultural practices and managing natural resources. The insights into how different months affect vegetation health can guide planting schedules, irrigation practices, and conservation efforts to enhance sustainability and productivity in regions with similar climatic conditions.

CONFLICT OF INTEREST STATEMENT

The authors declare that there is no conflict of interest.

REFERENCES

- [1]. Chen, M., et al. (2016). Quantifying the effects of solar radiation on ecosystem processes. International Journal of Biometeorology, 60(9), 1443-1452.
- [2]. Wang, X., Liu, Y., Zhang, Z. (2019). "Quantifying the Impact of Solar Radiation on Vegetation Dynamics Using Remote Sensing Data." Remote Sensing of Environment, 210, 89-104.
- [3]. Pettorelli, N., et al. (2005). Using the satellite-derived NDVI to assess ecological responses to environmental change. Trends in Ecology & Evolution, 20(9), 503-510.
- [4]. Ahlström, A., et al. (2015). The dominant role of semi-arid ecosystems in the trend and variability of the land CO2 sink. Science, 348(6237), 895-899.
- [5]. Huete, A. R., Didan, K., Miura, T., Rodriguez, E. P., Gao, X., & Ferreira, L. G. (2002). Overview of the radiometric and biophysical performance of the MODIS vegetation indices. Remote Sensing of Environment, 83(1-2), 195-213.
- [6]. Jones, D. A., Donato-Woodger, S., & Krishnaswamy, J. (2018). Mangroves of Oman: Status, threats, conservation and management. Ocean & Coastal Management, 162, 49-60.
- [7]. Al-Harthi, S., Hamad, M., Al-Amri, I., Al-Siyabi, M., & Al-Zadjali, M. (2017). Land use/cover mapping and change detection in arid environment: The case of Oman. Environmental Monitoring and Assessment, 189(6), 285.
- [8]. Al-Kalbani, M., Said, A. R., & Al-Kalbani, H. M. (2020). Ecosystem services and biodiversity of the Arabian Peninsula. In The Arabian Peninsula (pp. 375-392). Springer, Cham.
- [9]. Al-Hashmi, K., et al. (2017). Coastal marine ecosystems of Oman: Patterns, status, and threats. Marine Pollution Bulletin, 114(2), 679-691.
- [10]. Smith, J., et al. (2018). Spatiotemporal Variations in Solar Radiation and NDVI Dynamics in Arid Regions: Insights from Remote Sensing and Climate Models. Remote Sensing, 35(4), 387-401. [Insert in-text citation for Smith et al. (2018)
- [11]. Smith, A.B., Jones, C.D. (2020). "Remote Sensing Techniques for Analyzing Solar Radiation Dynamics in Environmental Studies." Journal of Environmental Science, 25(3), 123-145.

Eco Trends in Civil Engineering

Ena Grčić¹, Marija Šperac¹, Dino Obradović^{1*}

¹ Josip Juraj Strossmayer University of Osijek, Faculty of Civil Engineering and Architecture Osijek, 31000 Osijek, Croatia.

*Corresponding Author email: dobradovic@gfos.hr

Abstract

Civil engineering is a human activity, a scientific and technical discipline that includes the design, organization and execution of all civil engineering and construction works. Some of the common construction products are roads, bridges, railways, tunnels, ports, drainage and water supply systems, dams, residential and public buildings, sports halls, etc. The construction of new buildings reduces the amount of green or arable land needed by the population. Also, the demolition of existing buildings creates waste that needs to be properly disposed. The problem of waste disposal is very pronounced nowadays, so it is necessary to look for new ways of using existing as well as newly created waste. One of the available ways of using waste is its incorporation into materials used in the construction of buildings. The above can be observed through the concept of circular economy, which is the opposite of linear economy. Circular economy says that products should be kept as long as possible in their life cycle, i.e. that no waste is created. Such resources should be reused in other products. The paper will present some of the materials that can be reused in construction, as well as application of certain products that improve certain properties of construction products. Some examples are reuse of glass fiber reinforced plastic in concrete, utilizing biosilica to enhance the compressive strength of cement mortar, boosting concrete strength with sewage sludge fly ash, adding rubber into the concrete mix and polyethylene terephthalate (PET) waste in concrete mixture. Eco trends must be applied in all phases: from design to construction and to removal of various objects. Eco trends in civil engineering are aimed at protecting the environment by reducing the amount of unusable waste material and saving on construction material prices.

Keywords

circular economy, civil engineering, eco trends, recycling, waste materials

1. INTRODUCTION

Construction sector is one of the largest and most dynamic sectors in Europe, currently accounting for 25% [1] of the total industrial production in Europe. Since the construction industry requires a large amount of raw materials, this makes it unsustainable. The fact behind the benefits of using recycled materials in construction is that if people mismanage and overuse natural resources — as they do now — these will eventually run out, so replacing natural resources with waste recycled products is the first step towards a circular economy and sustainable construction. Recycling materials contribute to reduction of waste, resource conservation, greenhouse gas emission reduction, and increased energy efficiency. Increased profitability and cost savings are two further benefits of employing recycled materials in the construction sector [2]. Utilizing recycled materials

may prove to be more cost-effective compared to virgin materials, particularly when obtained from nearby sources and incurring reduced transportation expenses. Additionally, they have the potential to decrease the necessity for costly charges associated with waste management, such as disposal fees and taxes. Recycled materials have the potential to foster new markets and open up new opportunities for companies and workers in the recycling industry. This, in turn, can contribute to the growth of local economy and generate additional income. On the other hand, recycled materials may have different properties and characteristics than the original materials, such as strength, durability, quality and compatibility, so it is important to conduct extensive laboratory research. In this context, this paper reviews the use of biosilica, glass fiber reinforced plastic, sludge fly ash, rubber and PET waste in concrete mix. A review of these five studies shows that the use of recycled materials has positive effects on the mechanical properties of concrete, indicating that their application is the basis for future innovation development.

2. CIRCULAR ECONOMY IN THE CONSTRUCTION INDUSTRY

Construction sector has been a sustainable sector since ancient times. The materials and building techniques used in the past were effective, creating ecologically designed structures while utilizing environmentally friendly materials that had a high potential for reuse and recyclability [3].

Sustainable circular economy represents a new economic model where the focus shifts from the narrow growth of gross domestic product to a multidimensional progress – broadly strengthening the quality of the environment, human well-being, and economic prosperity for current and future generations. The circular economy is a business model with the potential to generate competitiveness of an economic entity in combination with innovation and sustainability. In order to implement this model, the traditional approach to the market, customers, and natural resources must change [4].

The construction industry has always had a significant impact on every national economy, evident from its contribution to the gross domestic product (GDP) structure and employment of a large workforce [5].

The transition from linear to circular economy is inevitable as linear production is associated with mass production and consumption of raw materials, without concern for the potential limitations of the availability of these resources [6]. Circular economy can make positive contribution to sustainability. It must be fully integrated with the sustainable development of an economic entity, expanding its scope from closed-loop recycling and short-term economic gain to a transformed economy that organizes resource access for maintaining or enhancing social welfare and environmental quality [4]. The concept of circular economy is shown on figure 1.

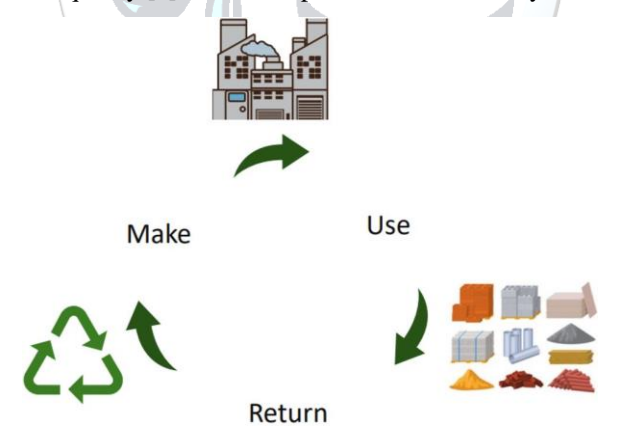


Figure 1. Concept of circular economy [7]

3. USE OF RECYCLED MATERIALS IN CONTRUCTION

3.1. Utilizing Biosilica to Enhance the Compressive Strength of Cement Mortar

Recent developments in the industrial sector involve the use of microsilica, a byproduct of metallurgical operations used to create metallic silicon, ferrosilicon, silumin, and other silicon alloys. Additionally, biosilica obtained by thermochemical processes from natural sources, like rice husk ash, is of considerable interest [8], [9]. The possibility that biosilica, a kind of silica that is naturally produced by diatoms, might improve the mechanical properties of cement-based materials is being studied. Due to the fact that it comes from a sustainable source and is biodegradable, biosilica has several advantages over traditional silica additions. In the building materials field, the use of biosilica in cement mortar is becoming increasingly important. Because of its

22 Grčić et al.

special characteristics, which include a wide surface area, small particle dimensions, and pozzolanic activity, it is a desirable addition for cement-based products to improve their mechanical performance.

The efficacy of an addition in cement mortar is determined not only by its intrinsic qualities, but also by the technique of inclusion into the mortar mixture. To produce a homogeneous dispersion of additives, maintain sufficient contact with the cement matrix, and influence the performance of composites, mixing processes are essential. Therefore, it is necessary to comprehend how mixing methods impact this material to maximize its efficacy and realize its full potential when using biosilica in cement mortar [9]. Biosilica synthesis from rice husk is shown on figure 2.

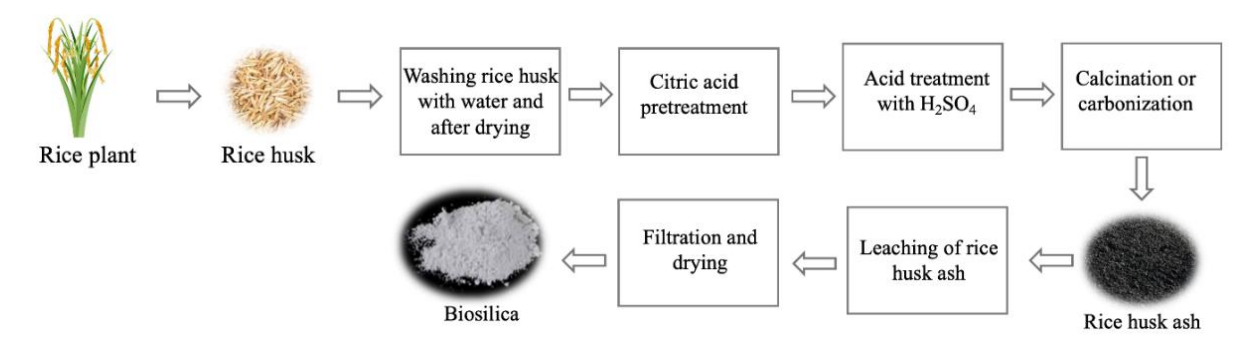


Figure 2. Schematic of biosilica synthesis from rice husk [10]

Research shows that integrating a significant quantity of biosilica can fill cracks, potentially boosting compressive strength and minimizing water absorption. Biosilica particles are capable of bearing compressive loads, contributing to enhanced strength. Owing to their minute dimensions, these particles can occupy empty spaces within the cement, resulting in heightened density. The presence of biosilica renders the pores rigid, aiding in preserving the structural integrity [9], [11].

3.2. Boosting Concrete Strength with Sewage Sludge Fly Ash

According to European regulations, sewage sludge fly ash (SSFA) waste generated by the combustion of municipal waste sludge in a fluidized bed should not end up in landfills, but must be subjected to different treatment methods. Considering the large quantities being produced, it is necessary to explore new approaches to managing this waste. Storage of SSFA has negative environmental consequences, including water pollution, changes in soil pH and adverse effects on flora and fauna [12], [13], [14].

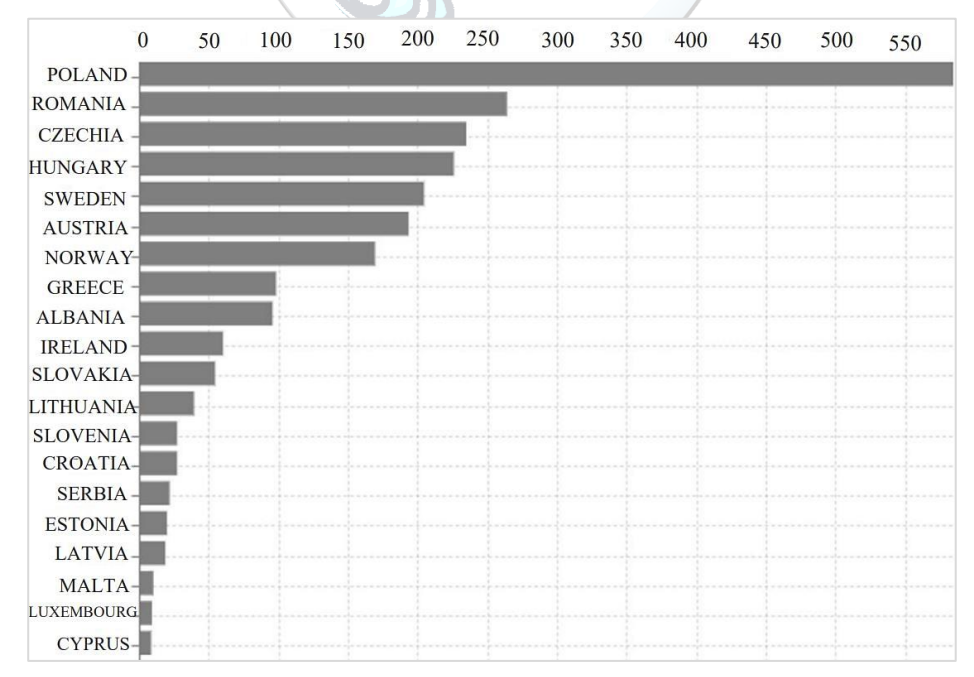


Figure 3. Sewage sludge production and disposal for 2021 [1]

Figure 3 shows sewage sludge production and disposal for countries in Europe for 2021. Quantities are expressed in thousands of tons. There is no data for Bulgaria, Germany, Spain, France, Netherlands, Portugal, Finland, Switzerland and United Kingdom.

Adding SSFA to cement and concrete brings a number of financial and environmental benefits. This reduces the amount of waste sludge in landfills, optimizes the costs and quality of construction materials, and reduces total disposal costs, including those specific to landfills. It also reduces the need for primary raw materials and promotes the sustainable development of the economy through the conversion of waste sludge into useful products. In addition, energy savings and the reduction in emissions of harmful substances such as NOx, CO₂ and other pollutants are achieved [15].

Considering the results of the experiments, it was observed that the compressive strength of concrete increases when SSFA is added, considering this fact, SSFA can be successfully used as an admixture in concrete. Furthermore, there are no legal guidelines related to the requirements of the physical and chemical properties of SSFA, as well as the possibility of its use in concrete production. By tailoring it to the unique requirements of the construction industry, we can successfully decrease SSFA [16]. By adapting it to the unique requirements of the construction industry, we can successfully reduce SSFA which is a starting point for further research.

3.3. Reuse of Glass Fibre Reinforced Plastic in Concrete

Glass fibre reinforced plastic, or GFRP, is becoming increasingly popular in several sectors. It is used, for instance, in the automotive, aerospace, building, marine, and renewable energy sectors [17]. A substantial quantity of glass fibre reinforced plastic waste is expected to decrease in the coming years due to the growth in production and use of the product on the basis of GFRP [18].

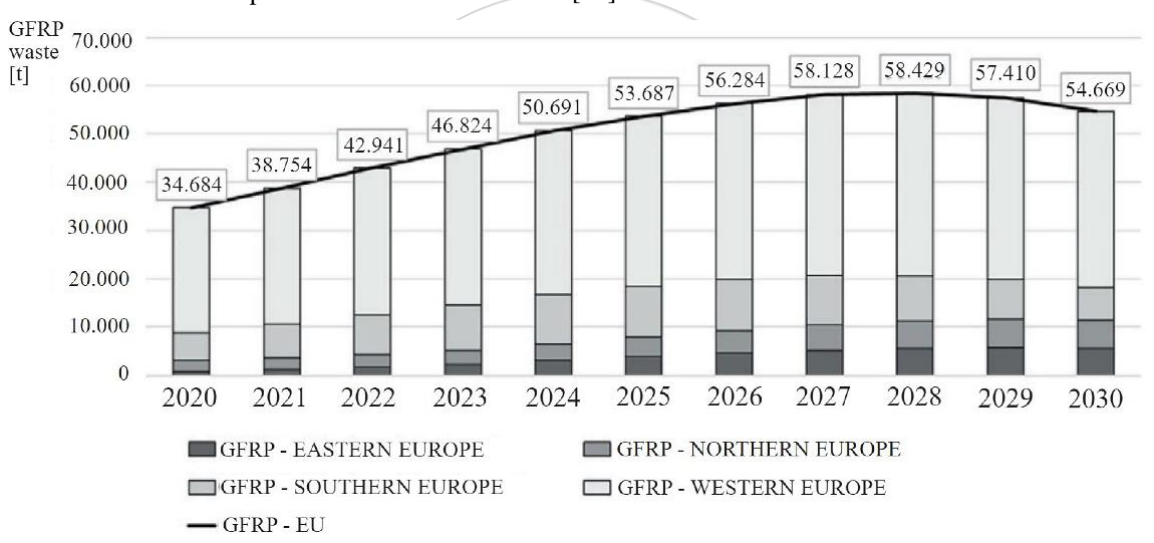


Figure 4. Amount of GFRP waste per region [19]

Figure 4 shows the amount of GFRP waste that appears in Europe. Data for Eastern, Northern, Southern and Western Europe from 2020 to 2030 are displayed. The black line across the graph represents the total waste from GFRP in the EU. The Y-axis represents the "Amount of GFRP waste per region" and ranges from 0 to 70,000. The X-axis represents the years from 2020 to 2030. Western Europe has the most GFRP waste in 2024, and Northern Europe the least. Western Europe has approximately 55,000 tons of waste and Northern Europe has approximately 20,000 tons of waste [19].

Sorting, trimming, pulverizing, and sifting are just some of the steps in the mechanical recycling process that are used to reduce the amount of GFRP waste [2], [20]. In the production of concrete, the use of mechanically recycled glass fibre reinforced plastic (rGFRP) appears to be a viable choice. This tactic not only lessens the quantity of materials that must be disposed of in landfills, but it also maintains and occasionally even enhances the concrete's quality [21].

Currently, three methods may integrate rGFRP from mechanical recycling in concrete. One method entails transforming GFRP waste into fine granules that can be used as fine aggregate in concrete mix. Another method entails cutting the GFRP waste into larger pieces, which are suitable for replacing the coarse aggregate in the concrete mix. In addition, GFRP waste that is turned into fine fibres by mechanical processing can be used in the production of reinforcing bars. Fibres further improve the mechanical properties of reinforcing bars. These three

24 Grčić et al.

methods for incorporating rGFRP into concrete have potential advantages as they can greatly improve the mechanical properties of concrete.

Research [22], [23], [24] showed that adding GFRP to concrete has increased the flexural strength, toughness of concrete, durability of concrete, control of cracking due to drying and reduction of moisture in the concrete mixture.

GFRP holds the potential to improve the properties of concrete mixture, but its application in concrete has not received enough research yet. Evaluating the long-term effects of using GFRP waste on the durability of concrete is also crucial. Further research into the possibilities of waste glass fiber reinforced polymer in concrete is becoming more pertinent due to the growing need for sustainable materials in the building industry.

3.4. PET Waste in Concrete Mixture

Significant environmental problems have arisen as a result of the massive amounts of stable waste made by polyethylene terephthalate (PET). Though they trail behind in terms of recycling and reuse, they nonetheless represent a sizable amount of all plastic waste. Recent research has investigated the viability of using recycled PET solid wastes as short fibres in cementitious composites [25].

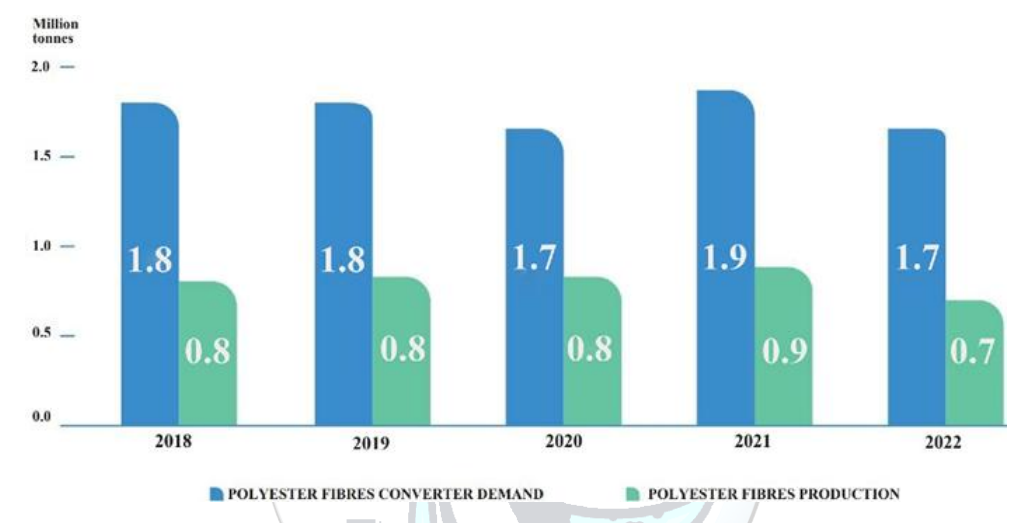


Figure 5. Polyester fibres production and converter demand evolution between 2018 and 2022 for EU [26]

Figure 5 shows the comparison of polyester fibre demand (blue bars) and production (green bars) from 2018 to 2022. The highest demand was recorded in 2021 and amounted to 1.9 million tons, while the lowest production was in 2022 and amounted to 700,000 tons. In 2022, the demand decreased due to unfavorable economic conditions, rising prices, and recessionary issues. Fibre production process is shown on figure 6. Also, table 1 shows the summary of test results on the mechanical properties of concrete modified with PET fibres.

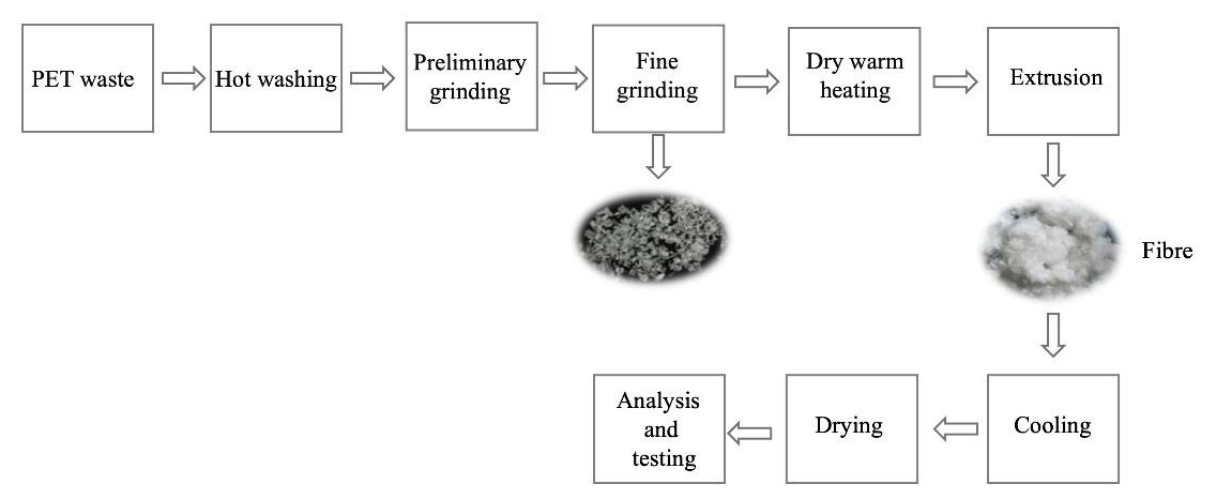


Figure 6. Fibre production process [27]

[32]

Mechanical Test results References properties Compressive With a higher proportion of fibres, the compressive strength decreases [27] strength Flexural Increases as the percentage of fibres in concrete increases [28] strength Split tensile Fiber can enhance the tensile splitting strength of concrete [29] strength At 1 % volume percent of plastic fibres, the shear strength of concrete Shear strength [27] increases, and it decreases as the volume fraction of fibres increases thereafter Modulus of [30] With a higher proportion of fibres, the modulus of elasticity decreases elasticity Bulk density With a higher proportion of fibres, the modulus of elasticity decreases [31]

Table 1. Test results on the mechanical properties of concrete modified with PET fibres

Apart from the fact that plastic is very useful for any form of industry, it also creates a big problem for the environment due to its slow decomposition. Considering the large quantities of PET waste, its use in concrete in the form of fibres provides an alternative to the disposal of large quantities of PET waste. Adding PET fibres to concrete improves flexural strength, split tensile strength, energy consumption and shear strength (depending on fibre concentration), while it has a negative impact on compressive strength and bulk density. For further research, it is necessary to examine how different concentrations, lengths, thicknesses, shapes, textures and surface treatments of PET fibres affect the mechanical properties of concrete under different loads and environmental conditions.

Increases as the percentage of fibres in concrete increases

3.5. Adding Rubber into the Concrete Mix

Energy

consumption

European countries face the problem of rehabilitation of a large amount of polymer waste that has no practical application. Rubber floor mats for cars belong to the group of polymer waste. Polymeric waste is a big problem because there is currently no effective method for disposing this type of waste. Some European Union countries charge an environmental fee for the disposal of rubber car floor mats, and the first country to introduce an environmental fee for this type of waste is Poland. Due to the mentioned problem, the option of adding polymer waste to concrete as a substitute for aggregate is being considered more and more [33]. Shredding process of rubber floor mats for cars is shown on figure 7.

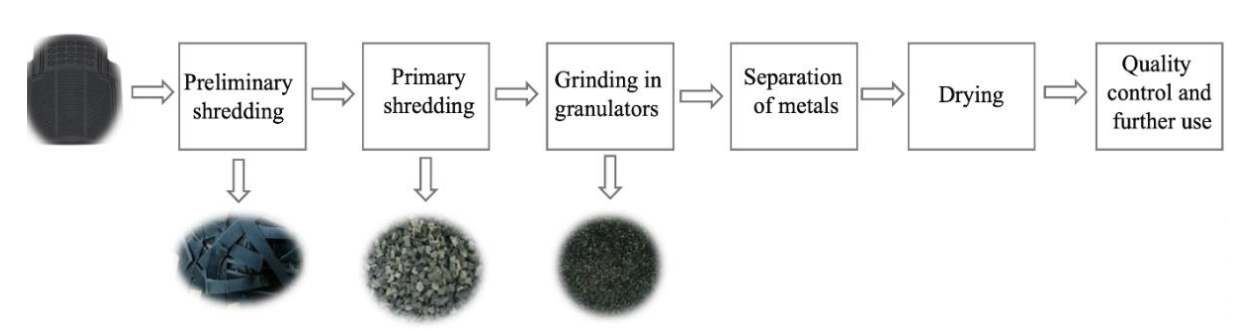


Figure 7. Shredding process of rubber floor mats for cars [34]

26 Grčić et al.

Table 2. Advantages and disadvantages of adding rubber as an aggregate to the concrete mixture [35], [36], [37]

Advantages	Disadvantages	
increases shrinkage	increases the penetration of chloride ions	
increases electrical resistance	reduces workability	
increases the ductility and deformation capacity of concrete	reduces the fire resistance	
increases thermal insulation	reduces resistance to carbonation	
improves impact load behaviour and impact load behaviour	reduces density	
increases the wear resistance of concrete	reduces mechanical strength	
increases sound absorption		

Rubber has many benefits over natural aggregates in mortars and concrete, including lower matrix density, greater flexibility, durability, better resistance to impact loads, better freeze-thaw resistance, better thermal and acoustic insulation, increased deformation capacity, and better energy absorption capabilities. However, using shredded rubber in place of natural aggregates in mortar or concrete formulations may have some disadvantages. A few examples are reduced workability, increased drying shrinkage, higher water absorption, and improved chloride ion penetration. To sum up, crumb rubber is a great material to use for creating lightweight mortars and concrete. Two interesting applications for it are as a shock absorber in road construction and as a shock-wave dampener in construction.

4. CONCLUSION

Sustainable construction and responsibility towards the environment requires the use of eco-friendly materials, waste reduction and the application of net zero building. The future of construction in the framework of sustainable development is reflected in the application of advanced construction technologies and sustainable designs. This implies the use of various environmentally acceptable materials. All this points to the necessity of adopting the principles of the circular economy in construction. Circular economy implies circular flows of materials, reuse of waste and resources, which ultimately results in an increase in ecological efficiency.

CONFLICT OF INTEREST STATEMENT

The authors declare that there is no conflict of interest.

REFERENCES

- [1]. Eurostat, EC Data Browser, Sewage sludge production and disposal, 2024, [Online]. Available: https://ec.europa.eu/eurostat/databrowser/view/env_ww_spd/default/bar?lang=en&category=env.env_wat.env_nwat. (Accessed: 04.05.2024.)
- [2]. A. E. Krauklis, C. W. Karl, A. I. Gagani, and J. K. Jørgensen, "Composite Material Recycling Technology—State-of-the-Art and Sustainable Development for the 2020s," *Journal of Composites Science*, vol. 5, no. 1, p. 28, 2021, doi: 10.3390/jcs5010028
- [3]. P. Núñez-Cacho, J. Górecki, V. Molina, and F. A. Corpas-Iglesias, "New Measures of Circular Economy Thinking In Construction Companies," *Journal of EU Research in Business*, vol. 2018, pp. 1–16, Apr. 2018, doi: 10.5171/2018.909360
- [4]. K. Vićentijević, "Održivost i cirkularna ekonomija", in *Zbornik radova MES*, vol. 1, no. 9, Oct. 2023, doi: 10.7251/BLCZR0623287V
- [5]. L. Lovrenčić Butković and M. Mihaljević, "Poznavanje koncepta kružne ekonomije u građevinskom sektoru", *Ekonomska misao i praksa*, vol. 30, no. 2, pp. 587–608, Dec. 2021, doi: 10.17818/EMIP/2021/2.14.

- [6]. M. Geissdoerfer, P. Savaget, N. M. P. Bocken, and E. J. Hultink, "The Circular Economy A new sustainability paradigm?," *Journal of Cleaner Production*, vol. 143, pp. 757–768, Feb. 2017, doi: 10.1016/j.jclepro.2016.12.048.
- [7]. C. K. Purchase *et al.*, "Circular Economy of Construction and Demolition Waste: A Literature Review on Lessons, Challenges, and Benefits," *Materials*, vol. 15, no. 1, p. 76, Dec. 2021, doi: 10.3390/ma15010076.
- [8]. J. Li, W. Zhang, C. Li, and P. J. M. Monteiro, "Green concrete containing diatomaceous earth and limestone: Workability, mechanical properties, and life-cycle assessment," *Journal of Cleaner Production*, vol. 223, pp. 662–679, Jun. 2019, doi: 10.1016/j.jclepro.2019.03.077.
- [9]. N. G. Muradyan *et al.*, "The Use of Biosilica to Increase the Compressive Strength of Cement Mortar: The Effect of the Mixing Method," *Materials*, vol. 16, no. 16, p. 5516, Aug. 2023, doi: 10.3390/ma16165516.
- [10]. S. Nawaz, F. Jamil, P. Akhter, M. Hussain, H. Jang, and Y.-K. Park, "Valorization of lignocellulosic rice husk producing biosilica and biofuels—a review," *Journal of Physics: Energy*, vol. 5, no. 1, p. 012003, 2023, doi: 10.1088/2515-7655/aca5b4.
- [11]. L. P. Singh, S. R. Karade, S. K. Bhattacharyya, M. M. Yousuf, and S. Ahalawat, "Beneficial role of nanosilica in cement based materials A review," *Construction and Building Materials*, vol. 47, pp. 1069–1077, Oct. 2013, doi: 10.1016/j.conbuildmat.2013.05.052.
- [12]. T. Umar, M. Yousaf, M. Akbar, N. Abbas, Z. Hussain, and W. S. Ansari, "An Experimental Study on Non-Destructive Evaluation of the Mechanical Characteristics of a Sustainable Concrete Incorporating Industrial Waste," *Materials*, vol. 15, no. 20, p. 7346, 2022, doi: 10.3390/ma15207346.
- [13]. Z. Hussain *et al.*, "Effect of fiber dosage on water permeability using a newly designed apparatus and crack monitoring of steel fiber–reinforced concrete under direct tensile loading," *Structural Health Monitoring*, vol. 21, no. 5, pp. 2083–2096, Sep. 2022, doi: 10.1177/14759217211052855.
- [14]. S. Ahmed, A. Hussain, Z. Hussain, Z. Pu, K. A. Ostrowski, and R. Walczak, "Effect of Carbon Black and Hybrid Steel-Polypropylene Fiber on the Mechanical and Self-Sensing Characteristics of Concrete Considering Different Coarse Aggregates' Sizes," *Materials*, vol. 14, no. 23, p. 7455, Dec. 2021, doi: 10.3390/ma14237455.
- [15]. O. Ginés, J. M. Chimenos, A. Vizcarro, J. Formosa, and J. R. Rosell, "Combined use of MSWI bottom ash and fly ash as aggregate in concrete formulation: Environmental and mechanical considerations," *Journal of Hazardous Materials*, vol. 169, no. 1–3, pp. 643–650, Sep. 2009, doi: 10.1016/j.jhazmat.2009.03.141.
- [16]. T. Kalak, P. Szypura, R. Cierpiszewski, and M. Ulewicz, "Modification of Concrete Composition Doped by Sewage Sludge Fly Ash and Its Effect on Compressive Strength," *Materials*, vol. 16, no. 11, p. 4043, May 2023, doi: 10.3390/ma16114043.
- [17]. C. B. Farinha, J. de Brito, and R. Veiga, "Assessment of glass fibre reinforced polymer waste reuse as filler in mortars," *Journal of Cleaner Production*, vol. 210, pp. 1579–1594, 2019, doi: 10.1016/j.jclepro.2018.11.080.
- [18]. F. Tittarelli and S. P. Shah, "Effect of low dosages of waste GRP dust on fresh and hardened properties of mortars: Part 1," *Construction and Buildings Materials*, vol. 47, pp. 1532–1538, 2013, doi: 10.1016/j.conbuildmat.2013.06.043.
- [19]. V. Sommer, J. Stockschläder, and G. Walther, "Estimation of glass and carbon fiber reinforced plastic waste from end-of-life rotor blades of wind power plants within the European Union," *Waste Management*, vol. 115, pp. 83–94, Sep. 2020, doi: 10.1016/j.wasman.2020.06.043.
- [20]. A. C. Meira Castro *et al.*, "Sustainable waste recycling solution for the glass fibre reinforced polymer composite materials industry," *Construction and Building Materials*, vol. 45, pp. 87–94, 2013, doi: 10.1016/j.conbuildmat.2013.03.092.
- [21]. N. Sebaibi, M. Benzerzour, N. E. Abriak, and C. Binetruy, "Mechanical properties of concrete-reinforced fibres and powders with crushed thermoset composites: The influence of fibre/matrix interaction," *Constr Build Mater*, vol. 29, pp. 332–338, 2012, doi: 10.1016/j.conbuildmat.2011.10.026.
- [22]. B. Fu, K. C. Liu, J. F. Chen, and J. G. Teng, "Concrete reinforced with macro fibres recycled from waste GFRP," *Construction and Building Materials*, vol. 310, p. 125063, Dec. 2021, doi: 10.1016/j.conbuildmat.2021.125063.
- [23]. A. Yazdanbakhsh, L. C. Bank, and C. Chen, "Use of recycled FRP reinforcing bar in concrete as coarse aggregate and its impact on the mechanical properties of concrete," *Construction and Building Materials*, vol. 121, pp. 278–284, Sep. 2016, doi: 10.1016/j.conbuildmat.2016.05.165.
- [24]. M. Mastali, Z. Abdollahnejad, A. Dalvand, A. Sattarifard, and M. Illikainen, "Comparative effects of using recycled CFRP and GFRP fibers on fresh- and hardened-state properties of self-compacting concretes: a review," in *New Materials in Civil Engineering*, Elsevier, 2020, pp. 643–655. doi: 10.1016/B978-0-12-818961-0.00019-3.
- [25]. J. Yu *et al.*, "Tensile performance of sustainable Strain-Hardening Cementitious Composites with hybrid PVA and recycled PET fibers," *Cement and Concrete Research*, vol. 107, pp. 110–123, May 2018, doi: 10.1016/j.cemconres.2018.02.013.

28 Grčić et al.

[26]. Pet Market in Europe: State of Play, Independent Commodity Intelligence Services, 2024, [Online]. Available: https://www.unesda.eu/wp-content/uploads/2024/03/PET-Market-in-Europe-State-of-Play.pdf. (Accessed: 25.05.2024.)

- [27]. R. N. Nibudey, P. B. Nagarnaik, D. K. Parbat, and A. M. Pande, "A model for compressive strength of PET fiber reinforced concrete," *American Journal of Engineering Research*, vol. 02, no. 12, pp. 367–372, 2013.
- [28]. R. Kandasamy and R. Murugesan, "Fiber Reinforced Self Compacting Concrete Using Domestic Waste Plastics as Fibres," *Journal of Engineering and Applied Sciences*, vol. 7, no. 6, pp. 405–410, Jun. 2012, doi: 10.3923/jeasci.2012.405.410.
- [29]. D. Foti, "Preliminary analysis of concrete reinforced with waste bottles PET fibers," *Construction and Building Materials*, vol. 25, no. 4, pp. 1906–1915, Apr. 2011, doi: 10.1016/j.conbuildmat.2010.11.066.
- [30]. J. M. Irwan, R. M. Asyraf, N. Othman, K. H. Koh, M. M. K. Annas, and S. K. Faisal, "The Mechanical Properties of PET Fiber Reinforced Concrete from Recycled Bottle Wastes," *Advanced Materials Research*, vol. 795, pp. 347–351, Sep. 2013, doi: 10.4028/www.scientific.net/AMR.795.347.
- [31]. Sampada Chavan and Pooja Rao, "Utilization of Waste PET Bottle Fibers in Concrete as an Innovation in Building Materials," *International Journal of Engineering Research*, vol. 5, pp. 304–307, 2016.
- [32]. M. da Silva Magalhães and M. Soares Viana Fernandes, "Bending Behaviour of Recycled PET Fiber Reinforced Cement-Based CompositeBending Behaviour of Recycled PET Fiber Reinforced Cement-Based Composite," *International Journal of Engineering and Technology*, vol. 7, no. 4, pp. 282–285, Aug. 2015, doi: 10.7763/IJET.2015.V7.805.
- [33]. A. Pietrzak and M. Ulewicz, "Influence of Post-Consumer Waste Thermoplastic Elastomers Obtained from Used Car Floor Mats on Concrete Properties," *Materials*, vol. 16, no. 6, p. 2231, Mar. 2023, doi: 10.3390/ma16062231.
- [34]. A. Pietrzak and M. Ulewicz, "Influence of Post-Consumer Waste Thermoplastic Elastomers Obtained from Used Car Floor Mats on Concrete Properties," *Materials*, vol. 16, no. 6, p. 2231, Mar. 2023, doi: 10.3390/ma16062231.
- [35]. N. M. Al-Akhras and M. M. Smadi, "Properties of tire rubber ash mortar," *Cement and Concrete Composites*, vol. 26, no. 7, pp. 821–826, Oct. 2004, doi: 10.1016/j.cemconcomp.2004.01.004.
- [36]. A. O. Atahan and A. Ö. Yücel, "Crumb rubber in concrete: Static and dynamic evaluation," *Construction and Building Materials*, vol. 36, pp. 617–622, Nov. 2012, doi: 10.1016/j.conbuildmat.2012.04.068.
- [37]. A. Benazzouk, O. Douzane, T. Langlet, K. Mezreb, J. M. Roucoult, and M. Quéneudec, "Physicomechanical properties and water absorption of cement composite containing shredded rubber wastes," *Cement and Concrete Composites*, vol. 29, no. 10, pp. 732–740, Nov. 2007, doi: 10.1016/j.cemconcomp.2007.07.001.

Why Is Pomegranate Molasses Important?

Rabia Serpil Gunhan¹

¹ Konya Technical University, Vocational High School of Technical Sciences, Department of Food Technology, 42250, Konya, Turkey

*Corresponding Author email: rsgunhan@ktun.edu.tr

Abstract

As the awareness of healthy life develops, the importance of functional foods increases. One of these foods is pomegranate molasses. It is noteworthy that the production and consumption in the Middle East and the world is increasing day by day. Pomegranate mollasses is obtained by pressing the pomegranate fruit and thickening the pomegranate juice in the open or under vacuum by heat treatment. It is a durable product because of high acidity and water soluble dry matter. It is used in soups, salads and special dishes (lahmacun, döner, meatball etc.). It has a high medical and nutritional value. It is a powerful antioxidant and rich in anthocyanins and other phenolic compounds. It has antitumoral, antimicrobial, anti-inflammatory and antidiabetic properties. With the increasing demand in recent years, it has been observed that the quality of pomegranate molasses has decreased and additives such as glucose syrup, date syrup and lemon salt have been added. Especially in pomegranate molasses produced by traditional method, there are problems such as high temperature in open boiler and not paying attention to packaging. The purpose of this review is to emphasize the importance of pomegranate molasses, to point out its difference with pomegranate sour sauce and to draw attention to the production of high quality pomegranate molasses.

Keywords

Pomegranate Molasses, Pomegranate Sour Sauces

1. INTRODUCTION

The cultural history of Pomegranate (Punica granatum L.) is quite old. It is stated that it dates back to BC 3000 years ago. It is an important fruit of Mediterranean countries with subtropical and tropical climates. It is mainly cultivated in Iran, Afghanistan, India, USA, Mediterranean countries (Tunisia, Turkey, Egypt, Spain, and Morocco) and to some extent China, Japan, and Russia ([13], [27]-[12]). In Turkey according to TUIK data pomegranate production are made about 300 thousand hectares in the area. Pomegranate is a product that grows in many regions of our country, especially in the Aegean and Mediterranean regions. Approximately 1/3 of our pomegranate production is exported ([5]).

Pomegranates are usually consumed fresh; however they are also a source of juice and molasses. Although rough information is obtained about the history of pomegranate from prehistoric times, we do not know exactly how long pomegranate molasses is in our lives. Turkey is one of the world's main pomegranate producing countries and produces the concentrated pomegranate juice known as pomegranate molasses or pomegranate syrup obtained from sour pomegranate species ([10]). Pomegranate molasses give flavor especially to salads and appetizers. It is used in dishes such as Mualle (a very demanding meal unique to Hatay), stuffed peppers, stuffed grape leaves,

30 Gunhan

chicken and meatballs as the main ingredient of direct food. Although it seems easy to produce, it is actually quite troublesome. 1 kg of pomegranate molasses is obtained from approximately 10-15 kg of pomegranate ([2]-[8]).

Pomegranate syrup is a sour food product obtained by pressing the pomegranate fruit, clarifying the obtained pomegranate juice and concentrating it in the open or under vacuum in accordance with the technique and consumed with the aim of flavoring foods ([2]). Pomegranate is a rich source of many valuable substances, such as tannins, (e.g., punicalagins, punicalins, proanthocyanidins), anthocyanins, phenolic acids (e.g., gallic acid, ellagic acid) and organic acids (e.g., malic acid). These substances have high antioxidant activity and have been correlated with health benefits against cancer, cardiovascular, and other diseases ([12]).

Since the pomegranate juice is concentrated in the production of pomegranate syrup, its nutritional value is quite high, there are more phenolic compounds and mineral substances than pomegranate juice. It is a storehouse of vitamins and energy, in addition it has high antibacterial and antioxidant effects because of containing phenolic compounds so it is beneficial in the treatment and prevention of many diseases([1], [4], [13], [35]-[37]

In this study, it was aimed to draw attention to the importance of pomegranate molasses, the differences between pomegranate molasses and pomegranate sauce, and the adulteration of pomegranate molasses.

2. METHODS OF POMEGRANATE MOLASSES PRODUCTION

The pomegranate molasses is produced by both industrial and traditional methods. The pomegranate juice is concentrated simply by boiling, without additives like sugar or others for traditional production of pomegranate molasses. On the other hand, the industrial ones may contain pomegranate juice concentrate, glucose, citric acid, antioxidant agents, coloring agents, and some preservatives as declared on the labels ([10]). Pomegranate molasses according to TSE ([36]); It is defined as "it is a sour food product obtained by pressing the pomegranate fruit, clarifying the obtained pomegranate juice and thickening it in the open or under vacuum in accordance with its technique and produced to flavor the foods." ([4]). According to Turkish Standards Institute pomegranate molasses should be free of sediment, fruit particles and sucrose. Whereas, people want bitter taste and sourness in pomegranate molasses. Therefore, it is not recommended to clarify the pomegranate juice. In the production of natural pomegranate molasses, a residue forms in the bottle and this residue is the condensated polyphenols ([1]).

The production steps of the traditional method of pomegranate molasses are washing, sorting, granulation, pressing, boiling (evaporation), cooling, removing of the solid phase and bottling respectively. This product is boiled in open boilers until its brix value becomes 35-50% and pomegranate molasses is obtained ([3]-[16]). In commercial production, there are pasteurization of pomegranate juice, enzyme addition, clarification, filtration, evaporation stages ([35])

Unlike pomegranate molasses, pomegranate sour souce contains glucose syrup, water, pomegranate flavor, acidity regulator (citric acid), coloring and preservative ([7]).

Table 1. General characteristics of pomegranate molasses ([36])

Features	Limits
Water soluble dry matter, at least	68.0%
Titratable acidity, not less than	7.5%
pH value	3.0
Hydroxymethyl furfural (HMF), (mg/kg)	50
No Sucrose	
No Preservatives	
No Artificial Dye stuffs	

3. THE QUALITY OF POMEGRANATE MOLASSES

Factors such as pomegranate variety, production method, method differences, heat treatment parameters, storage conditions directly affect the quality of pomegranate molasses. Physicochemical properties such as pH, dry matter, viscosity, bioactive compound level, HMF level, whether there is glucose and antioxidant activity are analyzed in the quality assessment of pomegranate molasses.

3.1. Pomegranate variety

The composition of pomogranate and pomogranate juice apart from the juice preparation methods is influenced by cultivar, growing conditions, climate, maturity and storage conditions ([31], [32], [26]-[19]). Pomegranates which have red grains and sour are selected especially to obtain pomegranate juice or pomegranate molasses ([33])

The contents of the pomegranate plant may vary according to the soil structure, climatic conditions, the time and amount of the plant to benefit from sunlight, the time of harvest, the storage conditions after harvest, cultural practices, etc. This situation causes the antioxidant and antibacterial effects of pomegranate molasses products to differ ([34]).

3.2. Production methos differences

Uncontrolled heat treatment in parallel with the application of heat treatment under open boiler or vacuum negatively affects phenolic compounds, anthocyanins, HMF load in pomegranate molasses ([22], [21], [20], [18]-[1]).

The method differences in the production of concentrated pomegranate juice directly affect the quality of pomegranate molasses. Apaydın ([19]) investigated the importance of clarification step during the production of concentrated pomegranete juice and observed that the production without clarification has more total phenolic substances (39%) and more antioxidant activity (25%) compared to clarificated ones and no significant change of total phenolic level in concentrated pomegranete juice samples during the storage. Maskan ([21]) investigated the effect of various heating methods (microwave, rotary vacuum and atmospheric heating) to produce concentrated pomegranate juice. He reported that the severity of colour loss was higher in rotary vacuum heating process than

32 Gunhan

the others and microwave energy could be used in production of pomegranate juice concentrate successfully. Dhumal et al.([22]) used different concentration techniques like atmospheric heating, microwave heating and rotary vacuum evaporation to produce the pomegranate juice concentrate. They reported that different heating methods influence the physicochemical constituents, sensorial properties and microbial population of concentrated pomegranate juice. They stated that vacuum evaporation give great benefits and the best colour in final product and vacuum concentration and microwave energy could be used in production of pomegranate juice concentrate successfully.

Unlike pomegranate molasses, pomegranate sour souce contains glucose syrup, water, pomegranate flavor, acidity regulator (citric acid), coloring and preservative ([7]). Food fraud is a serious ethical and economic problem affecting the food industry. Darra et al. ([14]) highlighted that date syrup was a potential raw material to adulterate commercial pomegranate molasses. They used UV/VIS spectroscopy, HPLC and ATR-FTIR method to determine the adulteration with date syrup and citric acid in the pomegranate molasses. They remarked that some of the commercialized pomegranate molasses in the Middle East area are adulterated with cheaper date syrup. Kamal et al.([13]) had developed successfully a new method that was simple, reliable and reproducible for the quality control of various formulations containing pomegranate. They reported that the matrix solid phase dispersion extraction methodology and HPLC method could be used successfully for the quantification of vitamin C, gallic acid, rutin and gallic acid in pomegranate molasses samples. Ergin ([4]) stated that some pomegranate molasses do not comply with the standards because of wrong practices and hygiene deficiencies during production and bottling in traditional production and using additives such as glucose / fructose syrup, synthetic antioxidant in commercial production.

3.3. Hydroxy Methyl Furfural (HMF)

HMF is an indicator of quality loss in most foods containing carbohydrates due to excessive heat treatment and improper storage conditions. HMF is known as an indicator of overheating, spoilage and possible adulteration with sugar or syrup. HMF is found in high levels in most foods, especially in caramel products (9.5 g/kg), dried fruits, wines, balsamic vinegars, molasses and pomegranate syrups. In high concentrations, Hydroxymethylfurfural (HMF) is known to have cytotoxic, genotoxic, nephrotoxic, mutagenic and carcinogenic effects ([7]). Orak ([20]) reported that the high temperature and long evaporation time of traditional method of pomegranate molasses destroy anthocyanin pigments and cause to increasing the level of HMF in concentrated pomegranate juices. Metin ([7]) determined HMF level of different brands of pomegranate molasses and pomegranate sour sauces saled in Turkey as 91.1 - 11485.7mg / kg and 41 - 151.9 mg / kg respectively. It is stated that the difference in HMF level in the products may be caused by the difference of pomegranate species, applied heat treatment technique, size and duration, and storage conditions. Hepsag et al. ([6]) determined quality parameters such as pH, water-soluble dry matter, titratable acidity, total dry matter, HMF, color analysis in home-type traditional pomegranate molasses produced from pomegranate varieties developed in the Osmaniye Region. The level of HMF were found to be in between 143.23 ile 530.68 mg/L. They stated that traditional home-type pomegranate syrups pose health problems because of their high HMF values. Onsekizoğlu ([24]) used osmotic distillation and membrane distillation + osmotic distillation methods in the production of pomegranate juice. He stated that HMF formation was low in the pomegranate juice concentrates obtained by these methods

3.4. Bioactive components of pomegranate molasses

Pomegranate juice contains significant phenolic substances. The substances that give the pomegranate color from pink to purple are anthocyanin group substances. Pomegranate juice carries a distinctive bitter flavor. This bitter flavor is caused by various polyphenolic substances and especially tannins. These substances are also the cause of cloudiness of pomegranate juice ([23]-[26]). İncedayı et al.([26]) investigated the chemical components which are important for health in different brands of pomegranate molasses. They reported that pomegranate molasses is rich in phenolics if it is produced correctly. The total amount of phenolic matter was found as 3246 μg gallic acid equivalent / mL in pomegranate juice and 9870 μg in pomegranate syrup.

Manufacturing of pomegranate juice causes relevant changes on the bioactive compounds [12]). It was stated that the heat treatment application in traditional pomegranate syrup production at high temperatures and long-term causes reduction of the anthocyanin pigments ([20]). Various factors including the temperature of processing and storage, the chemical nature of antosiyonin, pH, ascorbic acid, hydrogen peroxide, sugars, light and metals affect the stability of antosiyanin in pomegranate juice. ([18]). Phenolic compounds such as anthocyanins, ellagic and gallic acids are remarkably decreasing during juice processing line, especially after pasteurization, clarification and filtration processes ([17]- [18]). Akyıldız et al. ([17]) reported that processing stages were caused to lose 26, 45 and 41 % of concentrations of ellagic acid, cy-3,5-diglu and gallic acid according to the initial contents. Özkan

([28]) determined that the anthocyanins from pomegranate juices was sensitive to hydrogen peroxide and added ascorbic acid increased the stability of anthocyanins in pomegranate juice.

3.5. Bioactivities and health benefits

Anthocyanins, ellagic acid derivatives, and hydrolyzable tannins are responsible for the high antioxidant activity of pomegranate juice. The high antioxidant activity in the pomegranate juices are correlated significantly to the total polyphenol and anthocyanin contents ([11]). Pomegranate juice has high antioxidant activity. This activity is associated with the flavonoid content of pomegranate ([29]). Yıldız et al. ([9]) determined that pomegranate molasses had high phenolic content, antioxidant and antimicrobial activity and indicated that pomegranate sour sauce was a potent antioxidant food and potential value as a functional food ingredient.

The phytochemicals found in pomegranate are predominantly polyphenols, including flavonoids (anthocyanins, catechins and other complex flavonoids) and hydrolyzable tannins (punicalin, pedunculagin, punicalagin, gallagic and ellagic acid esters of glucose), which account for 92% of its antioxidant activity ([9]). Pomegranate phytochemicals are effective in prevention of various types of cancers, various cardiovascular diseases, in the treatment for trauma haemorrhage, ulcers, infections, diarrhoea and dysentery ([13]- [9]). Ellagic acid in pomegranate is the most important bioactive compound on human health. It has antioxidant, anticarcinogenic, antiestrogenic and antimutagenic effects ([27]). According to Mounayer et al. ([25]), pomegranate molasses possesses a powerful antioxidant activity and a weight loss effect in mice. They reported that pomegranate molasses at low doses in the beverage of mice is able to resist weight gain, induce the loss of fat stores, decrease tissue necrosis, and protect against deleterious effects of free radicals ([25]).

Antioxidant activity of different brands of commercial pomegranate molasses was determined by Incedayı et al. ([26]) as between 0-46.31%. Orak ([20]) compared the antioxidant levels of pomegranate juice and traditional pomegranate molasses and reported that the antioxidant activity of pomegranate extract (85.91%) was higher than that of pomegranate juice (79.06%). In the same study, pomegranate molasses was found to decrease the glucose and fructose levels and increase the potassium and magnesium ratios. The total amount of phenolic substance was found in pomegranate juice and in pomegranate molasses as 3246 μ g gallic acid equivalent / mL and 9870 μ g gallic acid equivalent / mL respectively.

Karabıyıklı and Kışla ([10]) investigated the antimicrobial effect of traditional pomegranate sour sauce and commercial pomegranate molasses on microflora of some green vegetables and burgul salad at different application times. They reported that traditional pomegranate molasses have more effective than the commercial pomegranate sauces on antimicrobial effect because of the differences of raw material and production methods. Gökoğlu et al. ([15]) investigated the effects of pomegranate sauce on the quality of marinated anchovy. Anchovy had marinated with acetic acid, salt, sunflower oil and pomegranate sauce. They demonstrated that pomegranate juice concentrate affected quality and shelf life of marinated fish, finding that pomegranate sauce showed better oxidative stability and pomegranate sauce gived a special taste.

As highlighted by Faour-Klingbeil and Todd ([30]), Pomegranate molasses had a great potential to enhance the microbial safety, especially *Salmonella enterica serovar Typhimurium LT2* (*S. typhimurium*), of parsley and salad vegetables as a food condiment. Kışla and Karabıyıklı ([8]) determined the minimum inhibitory concentrations (MICs) of both traditional and commercial sour pomegranate sauce samples on *Staphylococcus aureus* (ATCC 25923) and *Escherichia coli* O157:H7 (ATCC 43895) and indicated that the traditional products showed more antimicrobial effect on the pathogens than the industrial products. It has been stated that the industrial products may contain glucose, glucose syrup, citric acid, antioxidant agents, coloring agents, some preservatives and these additives caused decreasing of the concentrations of antimicrobial compounds.

4. CONCLUSION

Since pomegranate syrup is a functional food, its production and consumption should be encouraged. In this context, correct production processes and consumer awareness gain particular importance. If the correct production technique is applied, pomegranate molasses is a very beneficial product for human health and has a high nutritional value. Especially being rich in phenolic content also increases the antioxidant activity of the product. In the production of traditional pomegranate syrup, production and bottling must be applied correctly and adequate attention should be given to hygiene. In industrial production, negativities such as additives, glucose / fructose syrup, antioxidant addition should not be allowed. It should be checked more frequently whether there is adulteration in pomegranate molasses and the consumer should be informed about consuming the right product. So pomegranate molasses is a product that should be included more in our diet.

34 Gunhan

REFERENCES

[1]. F.Ş. Eyigün, 'Hicaz Nar çeşidine ait narlardan elde edilen nar ekşilerinin özelliklerinin belirlenmesi üzerine bir araştırma', Yüksek lisans tezi , Çukurova Üniversitesi, Fen Bilimleri Enstitüsü, Gıda Mühendisliği Anabilim Dalı, Türkiye, 2012.

- [2]. T. Baysal ve Ö. Taştan, Nar ürünleri ve üretimi, İn book: Nar Sağlıkta Yıldız Publisher: Gece Kitaplığı, 2018.
- [3]. Bilgin C., 2017. Ekşinin en tatlı hali nar ekşisi, Available: https://www.gidagundemi.com/makale/eksinin-entatli-hali-nar-eksisi-m228.html
- [4]. S.Ö. Ergin, 'Nar Meyvesi (Punica granatum L.) ile Farklı Nar Ürünlerinin Antioksidan Özellikleri', *Akademik Gıda* 17(2), 243-251, 2019.
- [5]. Anonim, 2019, Nar Raporu, https://zmo.org.tr/genel/bizden_detay.php?kod=32164&tipi=17&sube=0
- [6]. F. Hepsağ, M. Ferliaslan, O. Duran, S. Okur ve Y. Yıldız, 'Osmaniye İlinde Geleneksel Ev Yapımı Üretilen Nar Ekşilerinin Kalite Özelliklerinin Belirlenmesi Üzerine Bir Araştırma,' *Batman Üniversitesi Yaşam Bilimleri Dergisi* 9(2), 95-107, 2019.
- [7]. Z. Metin, 'Ankara piyasasında satışa sunulan nar ekşisi, nar ekşisi sosu ve üzüm pekmezlerinin hidroksimetilfurfural düzeyinin saptanması', Yüksek Lisans Tezi, Hacettepe Üniversitesi, Sağlık Bilimleri Enstitüsü, Türkiye, 2014.
- [8]. D. Kışla and Karabıyıklı Ş., 'Antimicrobial Effect of Sour Pomegranate Sauce on *Escherichia coli* O157: H7 and *Staphylococcus aureus*.' *Journal of Food Science*. Vol. 78, Nr. 5., 2013.
- [9]. Yildiz H, Sengul M, Cetin B, Karatas N, Ercisli S, Okcu Z, Dzubur A. and Hadziabulic S., 'Antioksidant and antimikrobial activities of pomegranate (Punica Granatum L.) sour sauce extracts,' Compt. rend. Acad. bulg. Sci., 67, No 1, 2014.
- [10]. Karabıyıklı S and D. Kışla, 'Inhibitory effect of sour pomegranate sauces on some green vegetables and kisir', *International Journal of Food Microbiology* 155, 211–216, 2012.
- [11]. Z. Kalaycıoğlu and F.B. Erim, 'Total phenolic contents, antioxidant activities, and bioactive ingredients of juices from pomegranate cultivars worldwide', *Food Chemistry*, 221, 496–507, 2017.
- [12]. N. Nuncio-Jáuregui, A. Calín-Sánchez, L. Vázquez-Araújo, A.J. Pérez-López, M.J. Frutos-Fernández and A.A. Carbonell-Barrachina, *Processing Pomegranates for Juice and Impact on Bioactive Components*, editör: Victor R. Preedy, Processing and Impact on Active Components in Food, Chapter 76, 629-636, 2015. http://dx.doi.org/10.1016/B978-0-12-404699-3.00076-7
- [13]. Y.T. Kamal, P. Alam, S.I. Alqasoumi, A.I. Foudah, M.H. Alqarni and H.S. Yusufoglu, 'Investigation of antioxidant compounds in commercial pomegranate molasses products using matrix-solid phase dispersion extraction coupled with HPLC', *Saudi Pharmaceutical Journal* 26, 839–844, 2018.
- [14]. N. Darra, H.N. Rajha, F. Saleh, R. Al-Oweini, R.G. Marounand and N. Louka, 'Food fraud detection in commercial pomegranate molasses syrups by UV-VIS spectroscopy, ATR-FTIR spectroscopy and HPLC methods', *Food Control* 78, 132-137, 2017.
- [15]. N. Gökoğlu, O.K. Topuz and P. Yerlikaya, 'Effects of pomegranate sauce on quality of marinated anchovy during refrigerated storage', *LWT Food Science and Technology*, 42, 113–118, 2019.
- [16]. H. Vardin ve M. Abbasoğlu, 'Nar ekşisi ve narın diğer değerlendirme olanakları,' *Geleneksel Gıdalar Sempozyumu* bildirileri, 2004, 165-169.
- [17]. A. Akyıldız, E. Karaca, E. Ağcam, B. Dundar and N.İ. Cınkır, 'Changes in quality attributes during production steps and frozen-storage of pomegranate juice concentrate,' *Journal of Food Composition and Analysis*, 92;103548, 2020.
- [18]. O. Turfan, M. Türkyılmaz, O. Yemiş and M. Özkan, 'Anthocyanin and colour changes during processing of pomegranate (Punica granatum L., cv. Hicaznar) juice from sacs and whole fruit', *Food Chem.* 129, 1644–1651, 2011.
- [19]. E. Apaydın, 'Nar suyu konsantresi üretimi ve depolama sürecinde antioksidan aktivitedeki değişimler', Yüksek lisans tezi, Ankara Üniversitesi, Fen Bilimleri Enstitüsü, Gıda Mühendisliği Anabilim Dalı, Türkiye, 2008.
- [20]. H. Orak, 'Evaluation of antioxidant activity, colour and some nutritional characteristics of pomegranate (*Punica granatum* L.) juice and its sour concentrate processed by conventional evaporation', *International Journal of Food Sciences and Nutrition*, 60(1): 1-11, 2008.
- [21]. M. Maskan, 'Production of pomegranate (Punica granatum L.) juice concentrate by various heating methods: colour degradation and kinetics', *Journal of Food Engineering*,72; 218–224, 2006.
- [22]. S.S. Dhumal, A.R. Karale, T.A. More, C.A. Nimbalkar, U.D. Chavan and S.B. Adhav, 'Preparation of Pomegranate Juice Concentrate by Various Heating Methods and Appraisal of Its Physicochemical Characteristics', *Beverage and Food World*, 42(5), 25-30, 2015.
- [23]. T. Öztan, 'Mor havuç, konsantresi, şalgam suyu, nar suyu ve nar ekşisi ürünlerinde antioksidan aktivitesi tayini ve fenolik madde profilinin belirlenmesi', Yüksek lisans tezi, İstanbul Teknik Üniversitesi, Fen Bilimleri Enstitüsü, Türkiye, Yüksek lisans tezi, 2006.

- [24]. P. Onsekizoğlu, 'Production of high quality clarified pomegranate juice concentrate by membrane processes', *Journal of Membrane Science*, 442, 264-271, 2013.
- [25]. A.C. Mounayar, A.R. Nemr, P. Yared, S. Khairallah and R. Chahine, 'Antioxidant and Weight Loss Effects of Pomegranate Molasses', *Journal of Applied Pharmaceutical Science*, 02 (06): 45-50, 2012.
- [26]. B. İncedayı, C.E. Tamer and Ö.U. Çopur, 'A research on the composition of pomegranate molasses'. Journal of Agricultural Faculty of Uludag University, 24(2), 37-47, 2010.
- [27]. M. Şimşek and A. İkinci, 'Narın (*Punica granatum* L.) İnsan Sağlığına Etkileri', *Harran Tarım ve Gıda Bilimleri Dergisi*, 21(4): 494-506, 2017.
- [28]. M. Özkan, 'Degradation of anthocyanins in sour cherry and pomegranate juices by hydrogen peroxide in the presence of added ascorbic acid', *Food Chemistry*, 78, 499–504, 2002.
- [29]. B. Cerda, R. Llorach, J.J. Ceron, J.C. Espin and T. Tomas-Barberan, 'Evaluation of the bioavailability and metabolism in the rat of punicalagin, an antioxidant polyphenol from pomegranate juice', *Eur. J. Nutr.*, 42, 18–30, 2003.
- [30]. D. Faour-Klingbeil and E.C.D. Todd, 'The inhibitory effect of traditional pomegranate molasses on S. typhimurium growth on parsley leaves and in mixed salad vegetables', *J Food Saf.*, 38;e12469, 2018. https://doi.org/10.1111/jfs.12469
- [31]. A. Topalavic, M. Knezevica, A. Gacnic and M.M. Petkovsek, 'Detailed chemical composition of juice from autochthonous pomegranate genotypes (*Punica granatum* L.) grown in different locations in Montenegro', *Food Chemistry*, 330; 127261, 2020.
- [32]. D.Y. Turgut ve A.C. Seydim, 'Akdeniz Bölgesi'nde yetiştirilen bazı Nar (*Punica granatum* L.) çeşit ve genotiplerinin organik asit ve şeker kompozisyonu', *Akademik Ziraaat Dergisi*, 2(1):35-42, 2013.
- [33]. A. İkinci ve H. Vardin, 'Nar meyvesi ve narın değerlendirilme şekilleri', *Tarım Türk*, 19(4), 2009.
- [34]. N. Erbil ve M. Arslan, 'Geleneksel Yöntemlerle Üretilen Nar Ekşisinin Antibakteriyel ve Antimutajenik Etki Potansiyeli', *Erzincan Ünv Fen Bilimleri Derg.*, 12(2), 957-965, 2019.
- [35]. S.Ö. Ergin, 'Investigation of the physicochemical, nutritional properties and antioxidant activities of commercial and traditional pomegranate molasses samples', *Food and Health*, 6(3), 177-185, 2020.
- [36]. Nar ekşisi standardı, TS 12720 / Nisan 2001.
- [37]. Y. Yılmaz, İ.Çelik and F. Işık, 'Mineral composition and total phenolic content of pomegranate molasses', *Journal of Food, Agriculture & Environment* Vol.5 (3&4): 102-104, 2007.



Fertilization zones generation using satellite imagery

Štefan Horvat¹*, Damjan Strnad¹, Matej Brumen¹, Domen Mongus¹

¹University of Maribor, Faculty of Electrical Engineering and Computer Science, 2000, Maribor, Slovenia. *Corresponding Author email: stefan.horvat@um.si

Abstract

One of the main goals of precision agriculture is to maximize crop yields, which requires efficient utilization of fertilizers. We present an automated procedure for generating a vector layer of zones that require different intensity of fertilization based on the value of vegetation index obtained from Sentinel-2 imagery. After obtaining the images we create a histogram, where the number of bins determines the number of fertilization zone classes we wish to obtain. Using the marching squares algorithm, we produce a final vector layer, which is exported to the GeoPackage format, making it compatible with modern agricultural equipment. We observe that fertilization zone generation depends on the field size, as large fields can generate more compact zones. Smaller fields tend to result in fragmented zones, due to bigger influence of neighboring regions pixels intensities. This approach thus offers a scalable solution for generation of fertilization zones, that can be used in fertilization map generation, but adjustments would be needed to reduce the effect of fragmentation.

Keywords

fertilization, precision agriculture, prescription maps, remote sensing

1. INTRODUCTION

The development of earth observation and processing technologies, such as Sentinel-2 satellites network and remote sensing, lead to widespread integration of precision agriculture in modern agricultural practices. Precision agriculture enables for site specific interventions without physical presence [1, 2]. With growing demand for food and the goal of sustainability while being respectful to the environment, generation of fertilization maps has recently been proposed to enable a more efficient planning of fertilizer disposal in the fields [1, 2, 3]. Application rates of fertilizer are important, as overfertilization can have negative consequences on the environment and be economically inefficient, while underfertilization does not utilize full crop potential and can lead to lower yield expectation [2].

Existing approaches to generation of fertilization maps usually involve satellite or UAV captured images [4] in combination with on-site soil sampling for wheat and barley [1, 2, 4, 5], rice [3, 6] and other types of crops. Soil sampling can be very costly and time consuming, since it requires a technician to take samples from fields and analyze them in the laboratory. After the analysis the agricultural experts prescribe the rate of fertilizer on corresponding locations [2, 7]. In this paper, an automated procedure is proposed, which omits onsite sampling and generates a vector layer of zones that require different intensity of fertilization based on the values of a

vegetation index. The procedure does not generate fertilization maps directly, but instead generates the zones that are prescribed with fertilization rates by agricultural experts.

The study area can be seen on Figure 1, located in northwestern Slovenia and is dominated by small and medium sized fields. Only fields that were planted with wheat or barley are considered in this study.

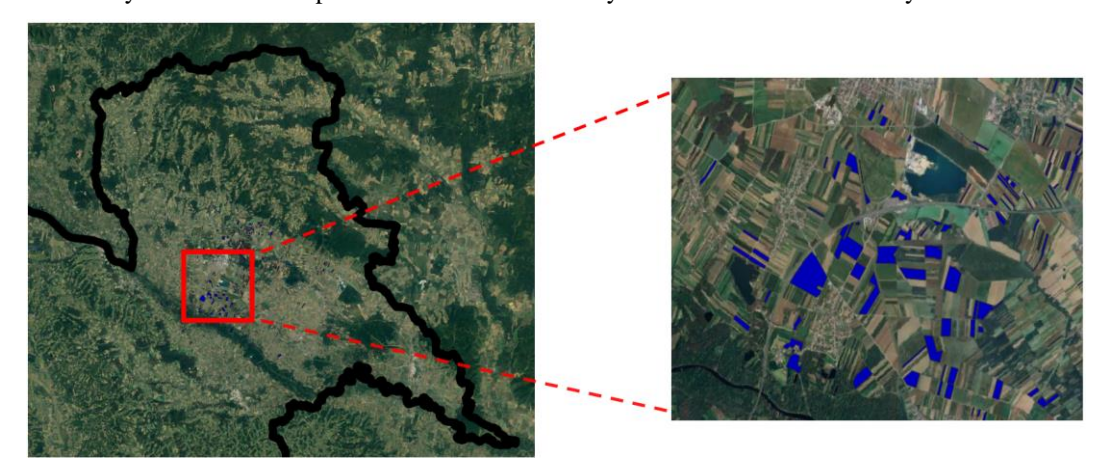


Figure 1: The study area located in NW Slovenia. Fields with blue color are included in the study and range from small to medium size fields (0.2 ha to 40 ha).

2. MATERIALS AND METHODS

The whole process of zone map generation consists of four steps. The most important step is the user defined number of fertilization zones, followed by execution of marching squares algorithm. In the last step all segmented zones are merged into a single vector layer. An example of the process is depicted in Figure 2.

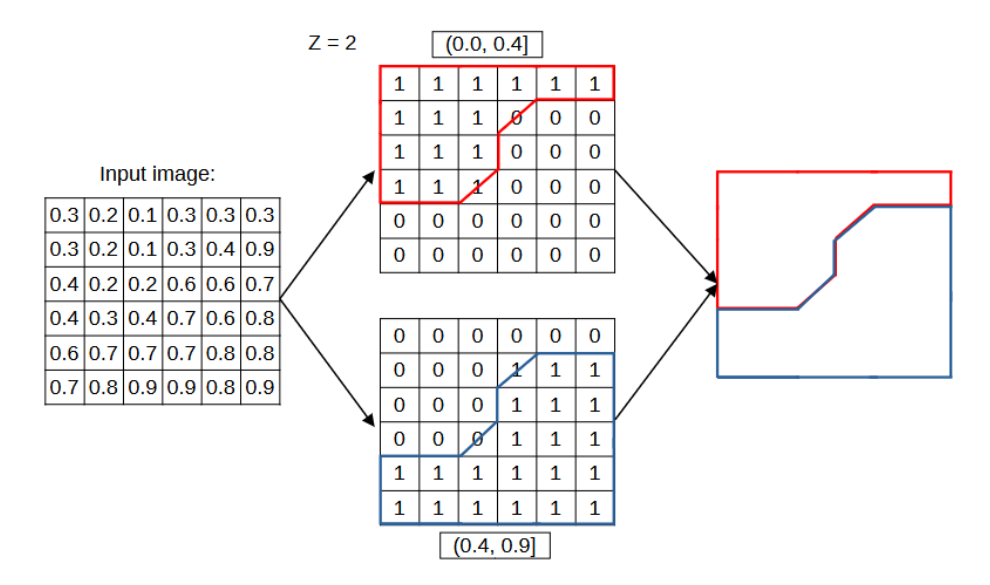


Figure 2: Histogram with 2 bins is created from an input image, followed by a segmentation with the marching squares algorithm and final merging into a single vector layer.

First we obtain the satellite imagery of the study area for a specified date and location from the Sentinel-2 satellite network. To estimate the crop health, the normalized difference vegetation index (NDVI) is used:

$$NDVI = \frac{NIR - R}{NIR + R} \tag{1}$$

Healthy crops have a greener response, which is effectively reflected by the index. The index values are from the interval [-1, 1], where 1 indicates excellent crop health [8].

38 Horvat et al.

In the second step, the number of classification zone classes are defined by the user. Based on the number of classification zones, a corresponding number of nonoverlapping bins in the histogram are created. The pixels are divided into bins based on their intensities.

In the third step, the segmentation of satellite images into fertilization zones is performed by the marching squares algorithm that generates a closed shape from isoline contours. The image of NDVI values is thresholded according to histogram bin limits and converted to a binary image for every bin. The value of 1 represents the pixels between the minimum and maximum thresholding value, other pixels are set to 0. A 2x2 window is slid over the binary image and a contour is assigned to it. There are 16 possible contours, which can be seen in Figure 3 and are stored in a lookup table. The contour is decided based on the values of neighboring pixels in 2x2 block [9].

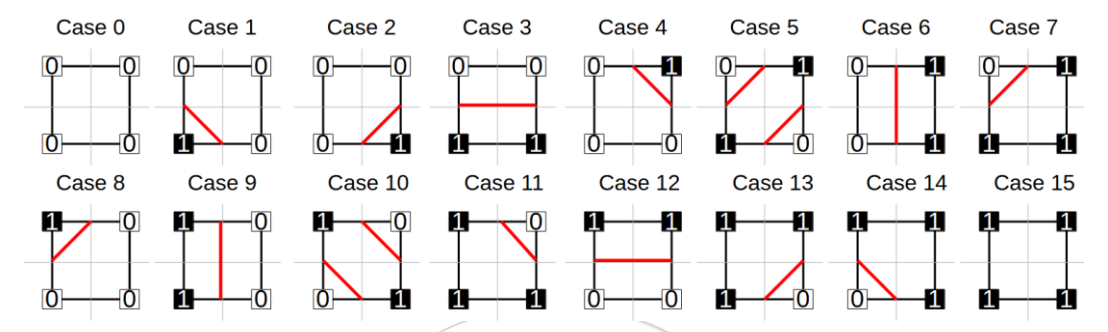


Figure 3: All 16 possible contour combinations that are stored in the lookup table in marching squares algorithm.

After the sliding, closed shapes that represent segments for each bin are saved to a vector layer. Finally, vector layers are merged into a final vector layer and exported to GPKG (GeoPackage) format. Attributes are assigned to classified fertilization zones. Attributes are used to set the amount of fertilizer to be disposed in the detected fertilization zones.

3. RESULTS AND DISCUSSION

The aim of this methodology was to segment fertilization zone classes from satellite images based on vegetation health, which we obtain from NDVI. The first batch of tests is visible on Figure 4a and was run in the early March 2024 with the number of fertilization classes set to 4. The greener areas in fertilization zone maps represent areas with excellent crop health, red color indicates poor crop health. The number of fertilization classes was chosen with the help of agricultural expert's advisory. The second batch of tests, visible on Figure 4b, was run in early May of 2024 with the same number of fertilization classes. Both time windows were chosen in coordination with agricultural experts just before the application of fertilization.

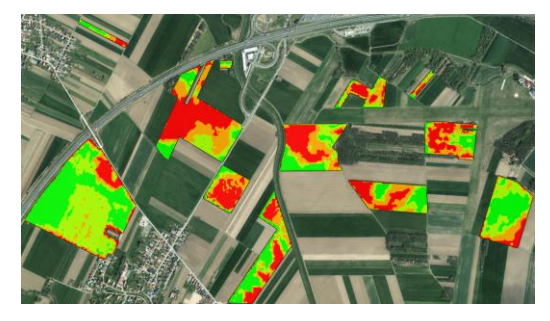
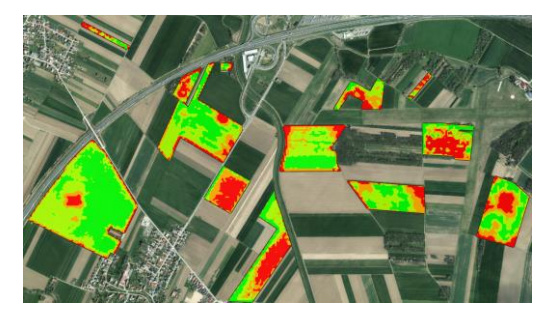


Figure 4. (a) An example of segmentation with 4 fertilization classes on an image from early March 2024.



(b) An example of segmentation with 4 fertilization classes on an image from early May 2024.

In Figure 4a the zones appear to be more compact. Figure 4b displays a different scenario, as zones appear to be smaller and much more fragmented. We observed that pixel intensities before segmentation were more

homogenous in Figure 4a and less so in Figure 4b. We also observed considerable fragmentation of edges in Figure 4b, which is caused by an overlap of pixels from neighboring regions.

We ran another experiment on a single field for early May of 2024 with 2, 3 and 4 classification zones (Figures 5a, 5b and 5c). We can clearly see, that with higher number of classification zone classes the fragmentation becomes more apparent.

Figures 4 and 5 highlight the problem of fertilization layers appearing blocky, which is one of the problems of the marching squares algorithm. As per advice by farmers and agricultural experts, a better shaped border in practice would be with rounder or oval edges.

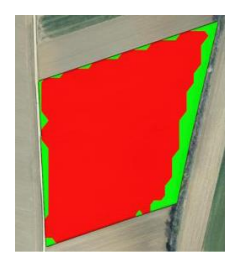
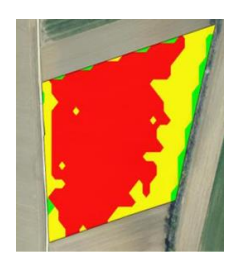
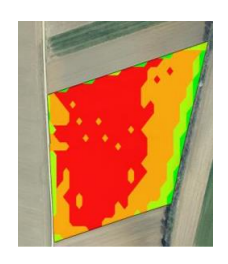


Figure 5. (a) Fertilization segmentation using 2 classification classes.



(b) Fertilization segmentation using 3 classification classes. The effect of fragmentation is noticeable here.



(c) Fertilization segmentation using 3 classification classes. The effect of fragmentation is evident here.

Results were also tested in practice by agricultural experts and farmers. The attributes of classified zones were manually set by agricultural experts in form of needed application of fertilizer and tested by farmers in the fields. The GPKG can easily be transferred to modern agricultural equipment and the experiment performed without problems.

4. CONCLUSION

The described method provides a scalable solution for generation of fertilization zones. Adequate fertilization zones can be generated, but one must be careful to avoid fragmentation when choosing the number of fertilization zone classes. In the future, we intend to tackle the problem with fragmentation by utilizing morphological operators. The application should reduce the number of small, isolated segmented shapes.

Another goal is to integrate fertilizer mapping to classification zone attributes automatically, without manual interventions. Currently, the agricultural experts must review the fertilization zones and manually assign fertilization rates, which takes a lot of time and effort. Avoiding this step would increase the efficiency and usability of the methodology in practice.

ACKNOWLEDGMENT

This research has received funding from the European Union through project Green.DAT.AI under grant agreement no. 101070416.

CONFLICT OF INTEREST STATEMENT

The author(s) declare(s) that there is no conflict of interest.

REFERENCES

- [1] L. R. Amaral and D. D. D. Justina, "Spatial Dependence Degree and Sampling Neighbourhood Influence on Interpolation Process for Fertilizer Prescription Maps" Engenharia Agrícola, 2019.
- [2] D. Radočaj, M. Jurišić and . M. Gašparović, "The Role of Remote Sensing Data and Methods in a Modern Approach to Fertilization in Precision Agriculture" Remote Sensing, 2022.
- [3] F. Yu, J. Bai, Z. Jin, H. Zhang, Z. Guo and C. Chen, "Research on Precise Fertilization Method of Rice Tillering Stage Based on UAV Hyperspectral Remote Sensing Prescription Map" Agronomy, 2022.

40 Horvat et al.

[4] A. Uribeetxebarria, A. Castellón and A. Aizpurua, "A First Approach to Determine If It Is Possible to Delineate In-Season N Fertilization Maps for Wheat Using NDVI Derived from Sentinel-2" Remote Sensing, 2022.

- [5] D. Bonfil, Y. Michael, S. Shiff and I. Lensky, "Optimizing Top Dressing Nitrogen Fertilization Using VEN μ S and Sentinel-2 L1 Data" Remote Sensing, 2021.
- [6] M. Yang, X. Xu, Z. Li, Y. Meng, X. Yang, X. Song, G. Yang, S. Xu, Q. Zhu and H. Xue, "Remote Sensing Prescription for Rice Nitrogen Fertilizer Recommendation Based on Improved NFOA Model" Agronomy, 2022.
- [7] R. Mihelič, J. Čop, M. Jakše, F. Štampar, D. Majer, S. Tojnko and S. Vršič, "Smernice za strokovno in utemeljeno gnojenje" 2011.
- [8] S. Huang, L. Tang, J. P. Hupy, Y. Wang and G. Shao, "A commentary review on the use of normalized difference vegetation index (NDVI) in the era of popular remote sensing" Journal of Forestry Research, 2021.
- [9] C. Maple, "Geometric design and space planning using the marching squares and marching cube algorithms" 2003 International Conference on Geometric Modeling and Graphics, 2003. Proceedings, 2003.
- [10] C. Fiorentino, A. R. Donvito, P. D'Antonio and S. Lopinto, "Experimental Methodology for Prescription Maps of Variable Rate Nitrogenous Fertilizers on Cereal Crops" Innovative Biosystems Engineering for Sustainable Agriculture, Forestry and Food Production, 2020.



Optimization of a 33-Bus Power Distribution System Using Artificial Hummingbird Algorithm for Power Loss and Voltage Stability Enhancement

Nisa Nacar Cikan^{1*}

¹ Cukurova University, Department of Electrical and Electronics Engineering, 01250, Saricam/Adana, Turkiye.
*Corresponding Author email: ncikan@cu.edu.tr

Abstract

This paper presents an optimization study on the 33-bus power distribution system using a reconfiguration technique to enhance system performance. The optimization process employs two objective functions: minimizing active power losses and improving voltage stability through the reduction of the voltage stability index. The Artificial Hummingbird Algorithm (AHA), a novel metaheuristic approach, is adopted due to its efficiency in handling complex optimization problems. The proposed methodology is applied to both single-objective and multi-objective scenarios to comprehensively evaluate the system's performance. Results demonstrate significant improvements in power loss reduction and voltage stability enhancement, underscoring the effectiveness of the AHA in optimizing reconfigured power distribution networks.

Keywords

Reconfiguration, Power Distribution Networks, Metaheuristic Algorithm, Power Loss Minimization

1. INTRODUCTION

Power distribution systems are typically designed in either grid or radial configurations, with specific switching points set throughout. Reconfiguring radial power systems plays a key role in enhancing the distribution grid's performance. Adjusting switching points appropriately can boost the distribution system's power quality, reduce energy losses, and maintain the stability of distribution lines. The power network employs two types of switches: sectionalizing switches (S.S.'s), which are generally closed, and tie switches (T.S.'s), which are typically open [1]. During reconfiguration, certain switches alter their status based on optimization outcomes. The task of determining the best switching positions is complex due to the vast number of potential configurations [2]. Both classical (deterministic) and meta-heuristic (stochastic) approaches are frequently used to solve the reconfiguration problem in power distribution network (RPPDN) [3],[4]. Because deterministic methods might become stuck in local optima and are difficult to distinguish, they frequently fail to identify a global optimal solution for highly nonlinear or nonconvex situations. Consequently, meta-heuristic techniques have been devised for this investigation.

The two main configurations of power distribution networks that are examined in the literature are balanced and unbalanced. Assuming that the loads and phases are spread equally, balanced networks make analysis easier and

42 Nacar Cikan

are frequently employed for idealized modeling. However, the presence of single-phase and multi-phase connections, fluctuations in phase loading, and uneven load distributions often result in imbalanced distribution networks in the real world. Since unbalanced systems more closely reflect the operational difficulties and asymmetries present in real-world power distribution networks, more sophisticated modeling and analysis techniques are needed to evaluate their performance [5],[6]. A comprehensive study and literature review focused on balanced power distribution networks (PDNs) is presented in [2], offering detailed insights and findings specific to this network type. In contrast, [5],[6] provides an in-depth literature review and extensive analysis dedicated to unbalanced PDNs, covering the complexities and unique characteristics associated with these systems. Together, these sources serve as valuable references for understanding the distinct challenges and methodologies applied to both balanced and unbalanced PDNs in the field.

In this study, a reconfiguration analysis was performed on a 33-bus power distribution network (PDN) using the Artificial Hummingbird Algorithm (AHA). The fitness function was designed to minimize active power loss and enhance the voltage stability index (VSI). The remainder of the paper is structured as follows: Section 2 presents the 33-bus PDN system along with the constraints; Section 3 discusses the AHA algorithm; Section 4 provides the results and discussion; and finally, the conclusion is given.

2. 33-BUS TEST SYSTEM

A popular standard test system in the literature, the 33-bus power distribution system is especially preferred for research on distribution network optimization and reconfiguration. Power is delivered to designated load centers by 33 buses that make up this medium-voltage distribution network, which normally operates at 12.66 kV. This system consists of distribution lines connecting load sites and a single power source, usually a main transformer station. There is just one power source and one power flow line, as it is typically portrayed in a radial layout or tree structure. This topology restricts the alternatives for redundant power flow even though it helps in fault current control. The system has 33 nodes and 32 lines, with power flowing through lines connecting each bus. Loads are distributed across various nodes; these loads vary depending on whether the distribution system is balanced or unbalanced. Figure 1 shows the 33-bus test system, commonly used as a standard model for analyzing distribution network reconfiguration, optimization, and performance under various operating conditions.

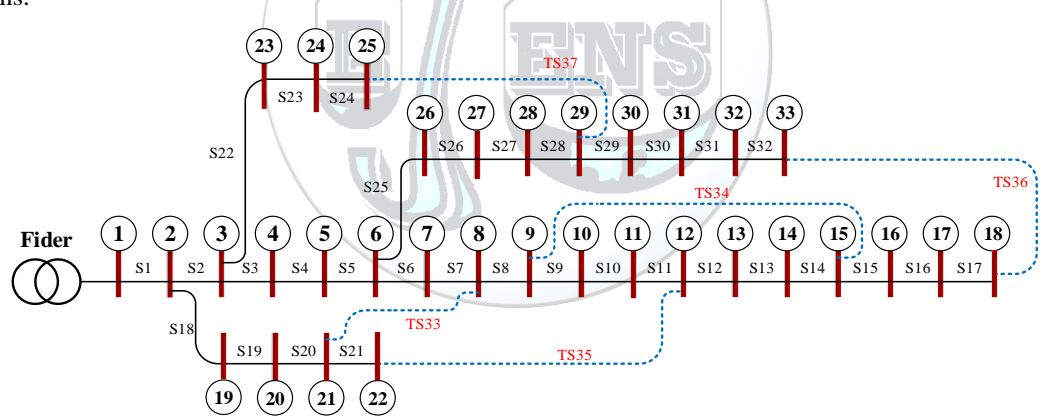


Figure 1. 33-bus test system [2].

2.1. Problem Formalization

The aim of this study is to minimize active power loss while enhancing the voltage stability index. Equation 1 presents the formula for minimizing power loss [2].

$$P_{Loss}^{min} = \left(\sum_{i,k=1,}^{N_{br}} r_{(i,k)} \cdot \left(\frac{P_k^2 + Q_k^2}{V_k^2}\right) \cdot Sw_{(i,k)}\right)$$
(1)

Equation 1 presents the formula for improvement of voltage stability index [2].

$$VSI = \frac{4|V_i|^2|C||D||S_k|\cos(\phi_k + \delta_S).\sin(\delta_i)}{|S_i|^2.\cos^2(\phi_i + \delta_K)} \le 1$$
(2)

More thorough investigation is required into the voltage stability of systems functioning near the limit values. The literature contains a wide variety of voltage stability indices. But the majority of them are predicated on a variety of ignorance or presumptions. This study makes use of a newly proposed index that takes into account several line properties and is based on line loading [4]. It has been noted that the recommended index consistently produces results under all situations and loading scenarios.

Voltage fluctuations must remain within specified limits in power systems as shown in Equation 3 [2].

$$V_{i,\varphi}^{min} \le V_{i,\varphi} \le V_{i,\varphi}^{max} \qquad \forall \varphi \in \{a,b,c\}, \ \forall i \in Buses \eqno(3)$$

The cable in the system should not carry more current than the limit outlined in Equation 4 [2].

$$I_{i,\phi} \le I_{i,\phi}^{\text{max}} \quad \forall \phi \in \{a, b, c\}, \quad \forall i \in \text{Branches}$$
 (4)

Equation 5 ensures that the total generated power equals the total load and losses in the system [2].

$$\sum_{i=1}^{N_{Gen}} P_{i,Gen}^{\emptyset} = \sum_{i=1}^{N_{Load}} P_{i,Load}^{\emptyset} + \sum_{i=1}^{N_{Branch}} P_{i,Loss}^{\emptyset} + \sum_{i,Loss} P_{i,Loss}^{equipment} \qquad \forall \phi \in \{a,b,c\}$$
 (5)

The transformers need to function within the designated voltage and current boundaries for each phase to guarantee their optimal performance and prevent any harm, as indicated in Equation 6 [2].

$$X_{i,\emptyset}^{trfmin} \le X_{i,\emptyset,trf} \le X_{i,\emptyset}^{trfmax} \quad \forall \phi \in \{a,b,c\}$$
 (6)

Equation 7 demonstrates that the amount of power flowing on a line cannot exceed a certain limit in order to maintain line security [2].

$$S_{i,\emptyset,line} \le S_{i,\emptyset,line}^{max} \qquad \forall \varphi \in \{a,b,c\}, \quad \forall i \in Lines \tag{7}$$

3. ARTIFICIAL HUMMINGBIRD ALGORITHM

The Artificial Hummingbird Algorithm (AHA) imitates the distinctive foraging and flight actions of hummingbirds for optimizing purposes. Hummingbirds are famous for their remarkable ability to quickly find food sources by using precise and agile movements to hover, change directions, and efficiently use energy while searching for nectar [7]. The AHA replicates these actions through different search patterns, such as exploration (wide search for possible solutions) and exploitation (targeted search around promising solutions), to maintain a equilibrium between uncovering new areas in the solution space and improving existing high-quality areas [7]. The AHA's flexibility allows it to excel in tackling intricate, nonlinear optimization issues across a variety of fields like power distribution networks, engineering design, and machine learning, with a focus on enhancing system performance and identifying global optima [7].

4. CONTENT

The comparison of active power loss and power flow at each branch before/after optimization is shown in Figure 2. Upon examining Figure 2, it can be observed that voltage improvements have occurred across all buses, with the exception of buses 20, 21, and 22. Specifically, the voltage levels have increased from 0.92 p.u. to approximately 0.94 p.u., reflecting an overall enhancement in voltage stability throughout most of the network.

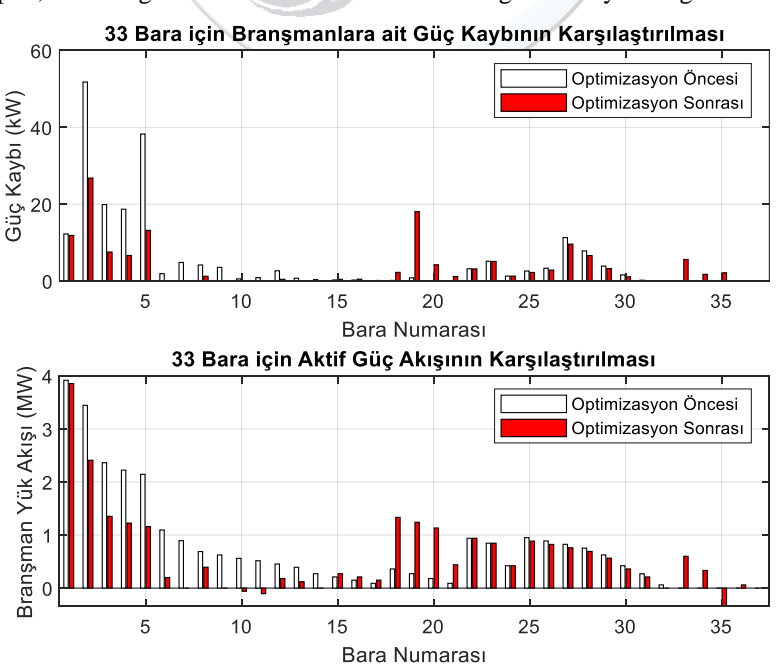


Figure 2. 33-bus power distribution network power loss and power flow results before and after reconfiguration.

44 Nacar Cikan

Figure 3 illustrates the bus voltages before and after the optimization process, which is influenced by the reconfiguration performed using the Artificial Hummingbird Algorithm. The comparison clearly highlights the effects of the optimization on the voltage levels across the buses, demonstrating the improvements achieved through this algorithmic approach.



Figure 3. Bus voltages before and after reconfiguration.

Upon examining Figure 3, it is evident that there are improvements in the voltage levels across all buses, with the exception of buses 20, 21, and 22. Notably, the voltage has increased from 0.92 p.u. to 0.94 p.u., indicating a positive enhancement in the overall voltage stability of the network, with most buses benefiting from the optimization.

Figure 4 presents the results of an optimization study conducted on a 33-bus PDN) focusing on the relationship between active power loss and the VSI. The graph features a Pareto front that illustrates the trade-off between these two objective functions, where each point on the front represents an optimal solution. Notably, four significant points are highlighted: the minimum VSI of 0.0024 associated with an active power loss of 235.154 kW, the minimum active power loss of 0.1548 kW with a VSI of 139, and two intermediate points at (0.0774027, 139.895) and (0.15481, 139.457).

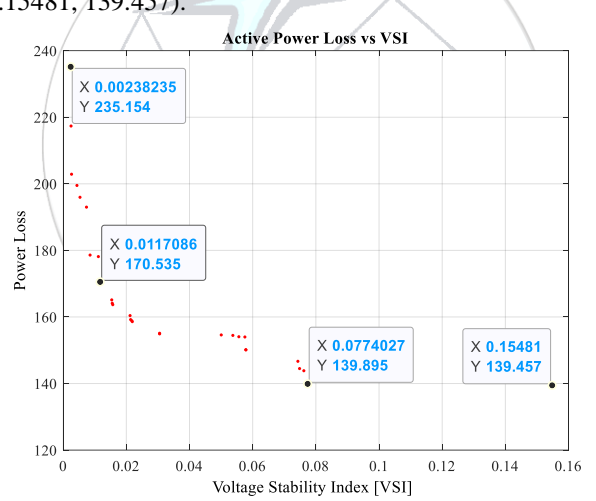


Figure 4. Pareto front analysis of active power loss vs. voltage stability index in a 33-bus test system

A trade-off analysis reveals that the lowest VSI value (0.00238235) corresponds to the highest power loss (235.154 kW), while the minimum power loss (170.535 kW) is achieved with a relatively higher VSI value (0.0117086). The intermediate points provide balanced solutions that reconcile the competing objectives of minimizing power loss while maintaining acceptable voltage stability. Overall, the VSI values range from 0 to 0.16, indicating that the system is generally in good condition regarding voltage stability. Meanwhile, the power losses fluctuate between approximately 139 kW and 235 kW, showcasing a significant optimization range within the study.

The Table 1 presents 30 distinct configurations, each characterized by various tie-switch combinations, enhancing the clarity and readability of the data. Among these configurations, one notable observation is that the lowest Voltage Stability Index (VSI) value of 0.0024 corresponds to the highest power loss of 235.2043 kW, indicating a less favorable balance between these metrics. Conversely, configuration 5 achieves the lowest power loss at 139.8948 kW; however, it does not represent an optimal solution regarding VSI, which stands at 0.0774.

Tie-Switches VSI No **Active Power** Losses [Kw] 0.0024 235.2043 0.0024 235.1539 Minimum VSI 150.1566 0.0578 Configuration q 0.1548 139.4572 **Minimum Active Power** 0.0774 139.8948 **Loss Configuration** 0.0537 154.4588 0.0305 154.9194 0.0578 150.1112 0.0762 143.8421 0.0305 155.1004 0.0111 178.1375 0.0748144.4929 0.0217 158.8707 0.0053 195.9564 202.8829 0.0027 0.0025 217.3672 0.0743 146.6760 0.0074 192.9956 0.0212 160.4115 0.0117 170.5351 0.0155 164.1114 154.0579 0.0556 0.0500 154.5985 153.9846 0.0575 0.0154 165.1299 0.0085 178.5942 0.0044 199.5078 0.0214 159.2061 0.0219 158.5957 0.0157 163.6877

Table 1. Dominated / Non-dominated pareto front results

This variability in configurations underscores the practical applications for system operators, who can strategically select configurations based on their operational needs. For instance, during periods of high load, configurations that minimize power loss may be favored, while during low load periods, those with higher VSI values can be selected to enhance voltage stability. This flexibility allows operators to effectively manage the trade-off between power losses and voltage stability in the distribution network.

5. CONCLUSION

In summary, this research highlights the efficacy of the Artificial Hummingbird Algorithm in optimizing a 33-bus Power Distribution Network, focusing on the dual objectives of minimizing active power loss and improving the Voltage Stability Index. The findings indicate notable enhancements in the system's performance through network reconfiguration, showcasing the advantages of optimized network topologies in power systems. The Pareto front generated from the multi-objective optimization effectively demonstrates the balance between reducing power loss and improving voltage stability, thereby serving as a crucial decision-making tool for system operators.

The variety of solutions provided by this approach enables the selection of optimal configurations tailored to specific operational needs. These results advance the field of power system optimization and suggest that implementing strategic reconfiguration methods in power distribution networks can yield significant operational advantages, such as reduced costs and enhanced reliability. Future studies could investigate the application of this methodology in larger networks and its potential integration with other optimization challenges in power systems, thereby further improving the efficiency of power distribution networks.

CONFLICT OF INTEREST STATEMENT

The author declares that there is no conflict of interest.

46 Nacar Cikan

REFERENCES

[1]. M. Çıkan and N. Nacar Çıkan, "Elektrikli araç şarj istasyonlarının enerji dağıtim hatlarına optimum şekilde konumlandırılması," Kahramanmaraş Sütçü İmam Üniversitesi Mühendislik Bilimleri Dergisi, vol.27, pp.340-363, Jun. 2024.

- [2]. M. Çıkan and B. Kekezoglu, "Comparison of metaheuristic optimization techniques including Equilibrium optimizer algorithm in power distribution network reconfiguration," *Alexandria Engineering Journal.*, vol.61, pp.991-1031.
- [3]. M. Çıkan, "Çita optimizasyon algoritması kullanarak kısmi gölgelenme altındaki fotovoltaik sistemlerde maksimum güç noktası izleyicisinin tasarlanması," *Gazi Üniversitesi Mühendislik Mimarlık Fakültesi Dergisi*, vol.40, pp.555-572.
- [4]. M. Çıkan and K. Dogansahin, "A Comprehensive Evaluation of Up-to-Date Optimization Algorithms on MPPT Application for Photovoltaic Systems," *Energy Sources, Part A: Recovery, Utilization, and Environmental Effects*, vol. 45, pp.10381-10407.
- [5]. M. Çıkan and N. Nacar Çıkan, "Optimum allocation of multiple type and number of DG units based on IEEE 123-bus unbalanced multi-phase power distribution system," *International Journal of Electrical Power & Energy Systems*, vol.144, pp.108564.
- [6]. N. Nacar Çıkan and M. Çıkan, "Reconfiguration of 123-bus unbalanced power distribution network analysis by considering minimization of current & voltage unbalanced indexes and power loss," *International Journal of Electrical Power & Energy Systems*, vol.157, pp.109796.
- [7]. W. Zhao, L. Wang, and S. Mirjalili, "Artificial hummingbird algorithm: A new bio-inspired optimizer with its engineering applications," *Computer Methods in Applied Mechanics and Engineering*, vol.388, pp.114194.



Simultaneous Allocation, Sizing, and Power Factor Optimization of Wind Turbines and EV Charging Stations in Power Distribution Networks

Murat Cikan*

Cukurova University, Vocational School of Technical Sciences, Adana Organized Industrial Zone, 01410, Sarıcam/Adana, Türkiye.

*Corresponding Author email: mcikan@cu.edu.tr

Abstract

This study explores the application of the Runge-Kutta Algorithm (RKO), a cutting-edge metaheuristic search technique, for the simultaneous allocation, sizing, and power factor optimization of wind turbines in power distribution systems. The research also involves the concurrent allocation of three 2 MW electric vehicle (EV) charging stations, integrated alongside the wind turbine installations. The objective is to minimize power loss while ensuring the efficient integration of renewable energy sources and EV charging infrastructure. The proposed RKO-based approach is evaluated for its effectiveness in optimizing component placement and enhancing overall system performance under dynamic load conditions. Simulation results indicate that the RKO algorithm offers a robust and efficient method for reducing power loss, making it a promising tool for future energy distribution system optimization.

Keywords

Dg Allocation and Size, EV Charging Stations, Runge-Kutta Algorithm, Power Distribution Network and Active Power Loss Minimization

1. INTRODUCTION

The integration of renewable energy sources and electric vehicle (EV) charging infrastructure [1], [2], [3] into existing power distribution networks is increasingly critical in the transition toward sustainable energy systems. Wind turbines and EV charging stations, as prominent distributed generation (DG) assets, provide opportunities for improving energy efficiency, reducing carbon emissions, and enhancing the reliability of power systems. However, the effective placement and sizing of these DG units within a distribution network are complex tasks, requiring careful consideration of power loss minimization [4], voltage stability, and operational constraints. Recent advances in optimization techniques have enabled more sophisticated approaches to DG allocation in distribution networks. Among these, population-based algorithms have shown promise due to their adaptability and efficiency in handling non-linear, multi-objective problems typical of power systems [5], [6]. In this context, the 136-Bus Test System is used as a model to evaluate the impact of DG [4] integration on a large-scale power distribution network, offering a realistic representation of the challenges faced in modern grid systems [7].

48 Cikan

This study employs the Runge-Kutta Algorithm (RKA) to determine the optimal locations and sizes of wind turbines and EV charging stations in the 136-Bus Test System. The objective functions focus on minimizing power losses and optimizing the Voltage Stability Index (VSI) to ensure network stability under varying load conditions. Additionally, operational constraints related to current limits, voltage levels, and power capacities are incorporated to maintain reliable network performance [8]. The results highlight the potential of RKA to enhance system efficiency by achieving substantial reductions in power losses and improvements in voltage stability.

This paper is structured as follows: Section 2 presents the mathematical formulation of the power system, including objective functions and constraints. Section 3 describes the methodology and implementation of the RKA for DG optimization. Section 4 discusses the placement and sizing results of wind turbines and EV charging stations and their effects on system performance. Finally, conclusions and recommendations for future research are provided in Section 5.

2. MATHEMATICAL EXPRESSION OF POWER SYSTEM

The mathematical modelling of the power system is fundamental for analyzing and optimizing network performance. This section presents the mathematical expressions governing the power flow, voltage stability, and loss minimization in the system. The power system model incorporates key parameters such as bus voltages, line impedances, power injections, and load demands, which collectively determine the system's operational state.

2.1. Constraint

This study defines several constraints related to current, power, and system capacity to ensure that the optimization process adheres to operational and safety limits. The current constraints prevent network branch overloading by maintaining current flow within each branch's permissible maximum. Power constraints are applied to regulate the distribution of active and reactive power throughout the network, ensuring that each bus and branch operates within designated bounds. These constraints, as shown in Equations (1) to (3), are essential for maintaining system stability, reliability, and efficiency. Each constraint is implemented as an inequality, effectively limiting the solution space to configurations that meet these technical and safety requirements.

• Voltage Constraints

$$V_{\min}^{\varphi} \le V_{i}^{\varphi} \le V_{\max}^{\varphi} \quad \forall i \in n, \varphi \in \{A, B, C\}$$
 (1)

• Current constraints

$$I_{ij}^{\varphi} \leq I_{ij,\text{max}}^{\varphi} \qquad \forall (i,j) \in m, \varphi \in \{A,B,C\}$$
 (2)

Power balance constraint

$$\sum_{i \in N} P_i = \sum_{j \in N} (P_j + P_{L,j}) \tag{3}$$

2.2. Objective Function

The primary objectives of this research are centered around two key objective functions. The first objective is the minimization of power losses [9] within the network, expressed by the formula in Equation (4). The second objective involves the optimization of the Voltage Stability Index (VSI) [8], as defined in Equation (5). These dual objectives are designed to enhance both the efficiency and reliability of the power distribution system.

$$P_{Loss}^{min} = \sum_{i,k=1}^{N_{br}} r_{(i,k)} \cdot \left(\frac{P_k^2 + Q_k^2}{V_k^2}\right) \cdot Sw_{(i,k)}$$
(4)

and,

$$VSI = \frac{4 |V_S|^2 |C||D||S_R| \cos(\phi_R + \delta_S) \sin(\delta_S)}{|S_S|^2 \cos^2(\phi_S + \delta_R)} \le 1$$
(5)

2.3. Newton-Raphson Power Flow Algorithm

The Newton-Raphson power flow algorithm is a fast and powerful iterative method widely used to solve power flow problems in energy systems. This method iteratively solves voltage magnitudes and phase angles to ensure stable operation of the energy system. The algorithm is based on solving power equations. The active (P) and reactive (Q) power equations in the system are expressed as follows:

$$P_{i} = V_{i} * \sum_{k=1}^{n} V_{k} (G_{ik} * \cos(\theta_{ik}) + B_{ik} * \sin(\theta_{ik}))$$
(6)

$$Q_{i} = V_{i} * \sum_{k=1, }^{n} V_{k}(G_{ik} * \sin(\theta_{ik}) - B_{ik} * \cos(\theta_{ik}))$$
(7)

In these equations, P_i and Q_i represent the active and reactive power for bus i, while V_i indicates the voltage magnitude at bus i. The variable θ_{ik} represents the voltage angle difference between buses i and k. G_{ik} and B_{ik} represent the conductance (G) and susceptance (B) values of the transmission line, respectively. These equations are solved to meet the load and generation demands in the system. The Newton-Raphson algorithm employs an iterative approach to solve power flow equations through linearization. The solution process consists of the following key steps:

2.3.1. Error Calculation

The mismatch between specified and calculated power values is determined in Eqs. 8 and 9.

$$\Delta P_{i} = P_{i}^{spec} - P_{i}^{cal} \tag{8}$$

$$\Delta Q_{i} = Q_{i}^{\text{spec}} - Q_{i}^{\text{cal}} \tag{9}$$

where P_i^{spec} and Q_i^{spec} represent the specified power values at bus i, while P_i^{cal} and Q_i^{cal} are the calculated values during iteration.

2.3.2. Jacobian Matrix Formation

The nonlinear power flow equations are linearized using the Jacobian matrix (J), as shown in Eq. 10.

$$\begin{bmatrix} \Delta \theta \\ \Delta Q \end{bmatrix} = J^{-1} \cdot \begin{bmatrix} \Delta P \\ \Delta Q \end{bmatrix} \tag{10}$$

The Jacobian matrix contains partial derivatives of power equations with respect to voltage magnitudes and angles.

2.3.3. State Variable Update

The voltage magnitudes and phase angles are updated in each iteration k, as shown in Eqs. 11 and 12.

$$\theta^{k+1} = \theta^k + \Delta \theta^k \tag{11}$$

$$\Delta V^{k+1} = V^k + \Delta V^k \tag{12}$$

2.3.4. Convergence Check

The iterative process continues until the power mismatches fall below a specified tolerance (ϵ), as shown in Eq. 13

$$|\Delta P| < \varepsilon \text{ and } |\Delta Q| < \varepsilon$$
 (13)

This iterative process ensures the systematic convergence of the solution while maintaining numerical stability. The method is particularly effective due to its quadratic convergence characteristics near the solution.

50 Cikan

2.4. 136-Bus Test System

The 136-Bus Test System [10], [11], representing a complex power distribution network, was employed to evaluate the effectiveness of the optimization algorithms. This system presents a network structure reflective of real-world scenarios, enabling a rigorous assessment of algorithmic performance. The 136-bus system includes 156 branches, with 21 left de-energized to maintain a radial configuration suitable for distribution network operations, as shown in Figure (1). The network comprises 107 spot loads, all modelled as PQ loads, distributed across the buses. The total active and reactive loads for the distribution line are 18.3 MW and 7.9 MVAR, respectively. Additionally, the system experiences total active and reactive power losses of 0.32037 MW and 0.70295 MVAR, respectively, across the distribution line. This test setup provides a robust framework for examining optimization solutions in power distribution contexts.

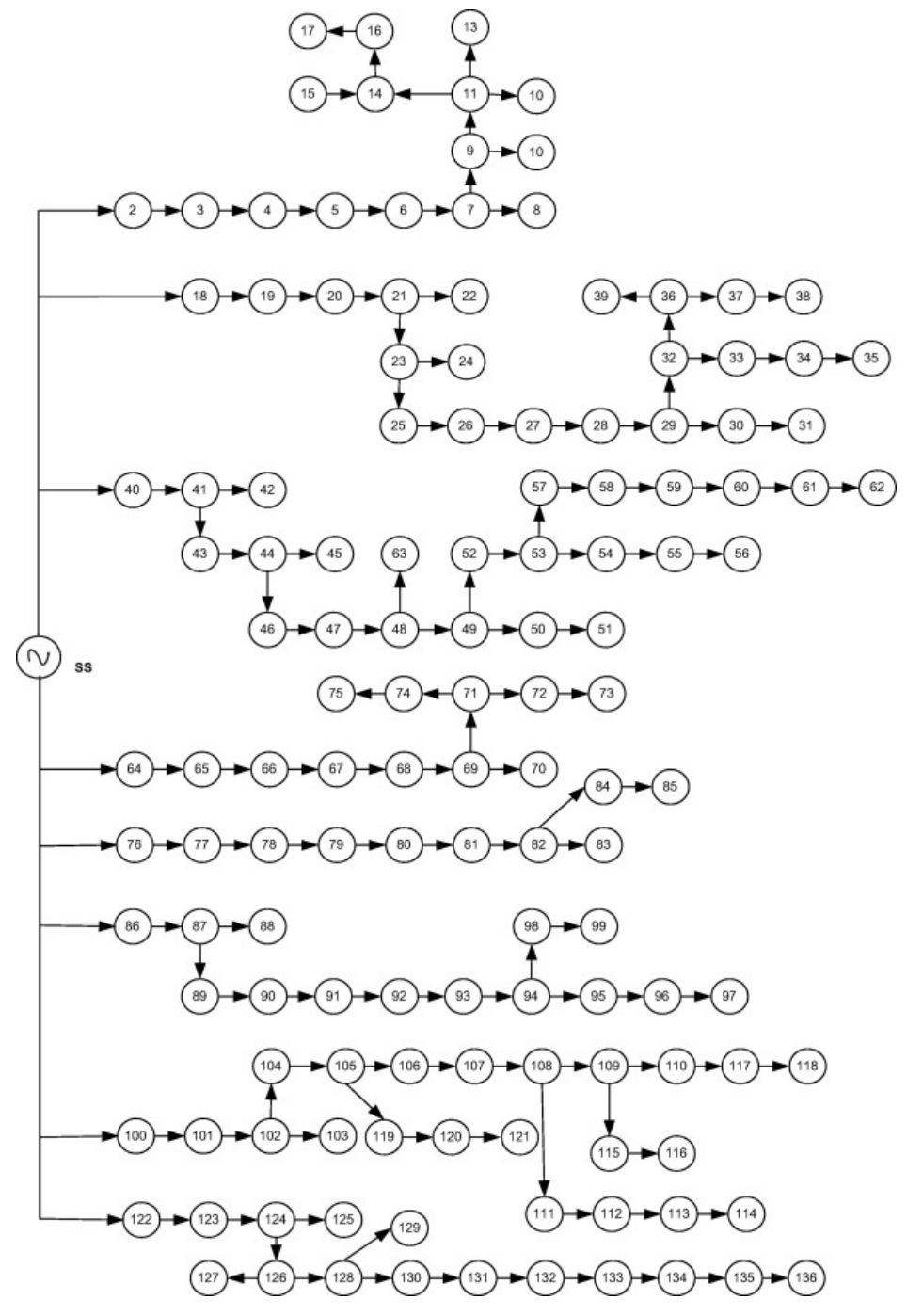


Figure 1. 136-Bus Power distribution network [10], [11]

3. RUNGE-KUTTA OPTIMIZATION ALGORITHM

The Runge-Kutta Optimizer (RUN) is a population-based optimization model developed based on the slope calculation principles of the fourth-order Runge-Kutta (RK4) method [12]. RUN systematically leverages RK4 to explore and exploit promising regions within the solution space, providing a robust framework for global optimization. The algorithm begins with the random initialization of population members, iteratively updating their positions based on a slope-driven mechanism derived from RK4. This approach strategically balances exploration and exploitation phases, maximizing solution quality and achieving rapid convergence. To further enhance robustness and prevent premature convergence to local optima, an Enhanced Solution Quality (ESQ) mechanism is integrated into RUN. Testing revealed that RUN achieved superior performance across a diverse range of mathematical benchmark functions and engineering design problems, consistently outperforming several state-of-the-art metaheuristic algorithms in both convergence speed and accuracy. RUN's high exploration capability originates from its elevated randomness, which facilitates a comprehensive search of the solution space. Meanwhile, its exploitation phase refines solutions around the best candidates, ensuring that high-quality solutions are consistently obtained. The mathematical expressions underpinning RUN's design are systematically defined from Equation (14) to Equation (20).

$$k_1 = \frac{1}{2\Delta_x} \left(\text{rand}_{\text{no}}. \left(x_{\text{worst}} - u. x_{\text{best}} \right) \right)$$
 (14)

$$u = round(rand_{no} + 1). (1 - rand_{no})$$
(15)

$$k_2 = \frac{1}{2\Delta_x} \left(rand_{no.} \left(x_{worst} - k_1. \Delta_x. rand_{no,1} \right) - \left(u. x_{best} + k_1. \Delta_x. rand_{no,2} \right) \right) \tag{16}$$

$$k_{3} = \frac{1}{2\Delta_{x}} \left(\operatorname{rand}_{\text{no.}} \left(x_{\text{worst}} - \frac{k_{2}}{2} \cdot \Delta_{x} \cdot \operatorname{rand}_{\text{no,1}} \right) - \left(u \cdot x_{\text{best}} + \frac{k_{2}}{2} \cdot \Delta_{x} \cdot \operatorname{rand}_{\text{no,2}} \right) \right)$$

$$(17)$$

$$k_4 = \frac{1}{2\Delta_x} \left(rand_{no.} \left(x_{worst} - k_3. \Delta_x. rand_{no,1} \right) - \left(u. x_{best} + k_3. \Delta_x. rand_{no,2} \right) \right)$$
 (18)

$$rand_{no} < \frac{1}{2}$$
, $x_{n+1} = SM.SF + \mu.x_s + x_c$ exploration phase otherwise, $x_{n+1} = SM.SF + \mu.x_s + x_m$ exploitation phase (19)

$$SF = \left(1 - \frac{\text{rand}_{\text{no}}}{2}\right) \cdot \left(a \cdot e^{-b \cdot \text{rand}_{\text{no}} \cdot \left(\frac{i}{\text{Max}_i}\right)}\right)$$
(20)

4. WIND TURBINE AND EV CHARGING STATIONS ALLOCATION AND SIZE

The allocation and sizing of wind turbines (WT) and electric vehicle (EV) charging stations in the 136-Bus Test System were optimized using the Runge-Kutta Algorithm (RKA). This approach aimed to enhance the system's efficiency by reducing power losses and improving voltage stability. The optimization process considered both active and reactive power limits for the wind turbines and the demand capacity for EV charging stations. The constraints for each parameter were determined by considering the network load capacity, Voltage Stability Index (VSI) limits, and spatial limitations related to EV charging infrastructure. Lower bounds (lb) and upper bounds (ub) were established to guide the optimization process (as detailed in Table 1), defining the minimum and maximum values for active and reactive power output, as well as EV charging power requirements, where the minimum and maximum values correspond to the first (1) and last (136) busbar numbers, respectively.

The Table 2 and Table 3 illustrates various scenarios tested during this study, showing the impact of DG additions on power loss and voltage stability. In the initial case, without DG, the system experiences an active power loss of 320.36 kW and a reactive power loss of 702.95 kVAR, with the minimum voltage recorded at 0.971 p.u. at bus 85. These baseline values serve as a reference for evaluating the effectiveness of DG integration.

Case 1: This scenario introduces a single wind turbine at bus 106, sized at 2828.4 kW and 1210.0 kVAR, along with an EV charging station at bus 1 with a demand of 2000 kW. These additions result in a significant reduction in system losses, with active power loss decreasing by 33.5% to 213.03 kW, and reactive power loss decreasing by 35.14% to 455.92 kVAR.

52 Cikan

Table 1 Lower and Upper boundary of Variables

Variable	Lower and Upper Allocation Limits	Active Power Size (MW)	Reactive Power Size (MVAr)
Wind Turking	1	lb: 0	lb: -10
Wind Turbine	136	ub :20	ub: 10
EV Charging	1	lb:0	
Stations	136	ub: 2	

Case 2: In this configuration, two wind turbines and two EV charging stations are incorporated. The first wind turbine remains at bus 106 (2828.4 kW, 1209.8 kVAR), and a second turbine is added at bus 11 with a capacity of 2326.7 kW and 930.57 kVAR. Both EV charging stations are set at bus 1 with a demand of 2000 kW each. This setup further reduces active and reactive power losses by 45.87% (173.42 kW) and 47.74% (367.36 kVAR), respectively, compared to the initial case.

Table 2 Allocation and Size of DGs

				v			
	DG	Location	Size of	Size of	P _{Loss}	Q ^{Active}	
Panel	Type	Location	DG / EV	DG / EV	P _{Loss}	Q Loss	
No							
		(Bus No)	(kW)	(kVAR)	(kW)	(kVar)	
Initial	w/o DG	-/ /	7//	-	320.3642	702.9472	
C 1	1st WT	106	2828.4	1210.0	212.0202	455.0170	
Case 1	1st EV	1	2000	105	213.0293	455.9170	
	1st WT	106	2828.4	1209.8			
C 2	1st EV	1	2000	0	172 4170	267.2596	
Case 2	$2^{nd} WT$	11	2326.7	930.57	173.4170	367.3586	
	2 nd EV	1	2000	0			
	1st WT	11	2326.7	930.57			
	1st EV	1	2000	0			
C 2	2^{nd} WT	29	2061.5	1012.6	142 1022	207 5572	
Case 3	2 nd EV	1	2000	0	142.1032	297.5572	
	3 rd WT	106	2828.4	1209.8			
	3 rd EV	1	2000	0			

Case 3: The most extensive configuration includes three wind turbines and three EV charging stations. The turbines are located at buses 11 (2326.7 kW, 930.57 kVAR), 29 (2061.5 kW, 1012.6 kVAR), and 106 (2828.4 kW, 1209.8 kVAR). The EV charging stations remain at bus 1 with a demand of 2000 kW each. In this scenario, the system achieves the highest reduction in losses, with active power loss minimized by 55.64% to 142.10 kW, and reactive power loss decreased by 57.67% to 297.56 kVAR. The voltage stability is also improved, maintaining a minimum voltage of 0.971 p.u. at bus 85 across all cases.

P_{Loss} Q_{Loss}^{Active} Minimum DG Type **VSI** Bus No Panel Voltage Reduction Reduction No (p.u.) V_{min} (%) (%) Initial w/o DG -3.182e-1 0.971 p.u. bus 85 ------1st WT Case 1 -2.1156e-2 0.971 p.u. bus 85 33.50 35.14 1st EV 1st WT 1st EV Case 2 8.6273e-01 0.971 p.u. bus 85 45.87 47.74 $2^{nd} \, WT$ 2nd EV 1st WT $1^{st} \, EV$ $2^{nd} \, WT$ Case 3 8.6273e-01 0.971 p.u. bus 85 55.64 57.67 2nd EV 3rd WT 3rd EV

Table 3 Voltage Stability Index, Active and Reactive Power Loss Results for the 136-Bus System

The table provides a detailed breakdown of each scenario, including DG type, location (bus number), size of DG in kW and kVAR, active and reactive power losses, Voltage Stability Index (VSI), minimum voltage, and the bus location of the minimum voltage. Additionally, the percentage reductions in active and reactive power losses are shown, illustrating the incremental benefits of each DG configuration. These results emphasize the role of optimized DG placement and sizing in enhancing system performance, particularly through reduced losses and improved voltage stability.

5. CONCLUSIONS

This study presented an optimization framework for the placement and sizing of wind turbines and EV charging stations in a complex power distribution network, utilizing the 136-Bus Test System as a representative model. The Runge-Kutta Algorithm (RKA) was employed to optimize system performance by minimizing power losses and enhancing voltage stability. Through multiple scenarios, the impact of distributed generation (DG) on system efficiency and reliability was evaluated, demonstrating significant reductions in active and reactive power losses and improvements in voltage stability. The results indicate that strategic allocation and sizing of DG sources, specifically wind turbines and EV charging stations, can substantially enhance network performance. The optimized configurations led to reductions in power losses by up to 55.64% and 57.67% for active and reactive losses, respectively, while maintaining voltage levels within safe operational limits. These findings underscore the effectiveness of RKA in addressing complex optimization challenges in power systems, offering a robust tool for planners and engineers aiming to integrate renewable energy sources and EV infrastructure into existing distribution networks. Future work can expand on this approach by incorporating additional renewable energy sources, such as solar PV systems, and evaluating the impacts of varying load profiles and seasonal fluctuations. Furthermore, the integration of real-time data and advanced machine learning

54 Cikan

techniques could further enhance the adaptability and accuracy of optimization solutions, contributing to more resilient and sustainable power systems.

ACKNOWLEDGMENT

This work was supported by the Scientific and Technological Research Council of Turkey (TÜBİTAK) under Grant No. 124E002 (1001-Project). The author gratefully acknowledges TÜBİTAK for their valuable support.

During the preparation of this work the author(s) used ChatGPT 4.o-mini in order to refine the English wording of certain phrases. After using this tool/service, the author reviewed and edited the content as needed and take(s) full responsibility for the content of the publication.

CONFLICT OF INTEREST STATEMENT

The author declares that there is no conflict of interest.

REFERENCES

- [1] M. Çıkan and N. Nacar Çıkan, "Elektrikli Araç Şarj İstasyonlarının Enerji Dağıtım Hatlarına Optimum Şekilde Konumlandırılması," Kahramanmaraş Sütçü İmam Üniversitesi Mühendislik Bilimleri Dergisi, vol. 27, no. 2, pp. 340–363, 2024, doi: 10.17780/ksujes.1365209.
- [2] M. Çıkan, "Çita optimizasyon algoritması kullanarak kısmi gölgelenme altındaki fotovoltaik sistemlerde maksimum güç noktası izleyicisinin tasarlanması," Gazi Üniversitesi Mühendislik Mimarlık Fakültesi Dergisi, vol. 40, no. 1, pp. 555–572, 2024, doi: 10.17341/gazimmfd.1183267.
- [3] M. Cikan and K. Dogansahin, "A Comprehensive Evaluation of Up-to-Date Optimization Algorithms on MPPT Application for Photovoltaic Systems," Energy Sources, Part A: Recovery, Utilization, and Environmental Effects, vol. 45, no. 4, pp. 10381–10407, Oct. 2023, doi: 10.1080/15567036.2023.2245771.
- [4] M. Cikan and N. N. Cikan, "Optimum allocation of multiple type and number of DG units based on IEEE 123-bus unbalanced multi-phase power distribution system," International Journal of Electrical Power & Energy Systems, vol. 144, p. 108564, 2023, doi: https://doi.org/10.1016/j.ijepes.2022.108564.
- [5] K. Aygül, M. Cikan, T. Demirdelen, and M. Tumay, "Butterfly optimization algorithm based maximum power point tracking of photovoltaic systems under partial shading condition," Energy Sources, Part A: Recovery, Utilization, and Environmental Effects, pp. 1–19, Oct. 2019, doi: 10.1080/15567036.2019.1677818.
- [6] F. Akın, M. Çıkan, O. Arikan, and B. Kekezoğlu, "Optimizing Distribution Network Reconfiguration for Power Loss and Fault Current Management," Mühendislik Bilimleri ve Araştırmaları Dergisi, vol. 6, no. 2, pp. 188–197, 2024, doi: 10.46387/bjesr.1501986.
- [7] N. Nacar Cikan and M. Cikan, "Reconfiguration of 123-bus unbalanced power distribution network analysis by considering minimization of current & voltage unbalanced indexes and power loss," International Journal of Electrical Power & Energy Systems, vol. 157, p. 109796, 2024, doi: https://doi.org/10.1016/j.ijepes.2024.109796.
- [8] K. Doğanşahin and M. Çikan, "A new line stability index for voltage stability analysis based on line loading," vol. 1, no. 1, pp. 23–30, 2023, doi: 10.14744/cetj.2023.000.
- [9] M. Cikan and B. Kekezoglu, "Comparison of metaheuristic optimization techniques including Equilibrium optimizer algorithm in power distribution network reconfiguration," Alexandria Engineering Journal, vol. 61, no. 2, pp. 991–1031, 2022, doi: https://doi.org/10.1016/j.aej.2021.06.079.
- [10] T. Yuvaraj and K. Ravi, "Multi-objective simultaneous DG and DSTATCOM allocation in radial distribution networks using cuckoo searching algorithm," Alexandria Engineering Journal, vol. 57, no. 4, pp. 2729–2742, Dec. 2018, doi: 10.1016/j.aej.2018.01.001.
- [11] J. R. S. Mantovani, F. Casari, and R. A. Romero, "Reconfiguração De Sistemas De Distribuição Radiais Utilizando O Critério De Queda De Tensão," 2000.
- [12] I. Ahmadianfar, A. A. Heidari, A. H. Gandomi, X. Chu, and H. Chen, "RUN beyond the metaphor: An efficient optimization algorithm based on Runge Kutta method," Expert Syst Appl, vol. 181, Nov. 2021, doi: 10.1016/j.eswa.2021.115079.

Optimization of PV, Capacitor Bank, and EV Charging Station Allocation in a 33-Bus Power Distribution System Using the Slime Mould Algorithm

Nisa Nacar Cikan1*

¹Cukurova University, Department of Electrical and Electronics Engineering, 01250, Saricam/Adana, Turkiye. *Corresponding Author email: ncikan@cu.edu.tr

Abstract

This study presents a comprehensive approach to the optimal allocation and sizing of photovoltaic (PV) systems and capacitor banks in a 33-bus power distribution system, focusing on enhancing system performance. Simultaneously, the allocation of PV systems, capacitor banks, and electric vehicle (EV) charging stations is addressed to optimize system efficiency. The primary objectives include minimizing active power losses and improving the voltage profile across the network. To solve this complex optimization problem, the Slime Mould Algorithm (SMA), a cutting-edge metaheuristic technique, is employed as an advanced tool for distributed generation (DG) allocation. SMA's robust search capability and adaptability make it well-suited for addressing the multi-objective nature of this study, delivering optimized results that balance system losses and voltage stability. The proposed method demonstrates significant potential for improving the efficiency and stability of modern power distribution networks.

Keywords

Electrical Vehicle Charging Stations, Slime Mode Algorithm, DG Allocation

1. INTRODUCTION

The growing incorporation of renewable energy sources into power distribution systems has become crucial for improving efficiency and sustainability. Among various renewable technologies, photovoltaic (PV) systems are particularly notable for their capability to capture solar energy, which is plentiful and eco-friendly [1],[2]. However, merely integrating PV systems into current power distribution systems is inadequate; a thoughtful strategy for their placement and sizing is essential to ensure they effectively enhance overall system performance. This research concentrates on a 33-bus power distribution system, analyzing the most effective locations for PV systems and capacitor banks to reduce active power losses and enhance the voltage profile throughout the network.

In addition to PV systems, the allocation of capacitor banks and electric vehicle (EV) charging stations is also critical in modern power distribution [3]. The rise of electric vehicles necessitates the establishment of efficient charging infrastructure, which can significantly influence power demand and network stability. By integrating these components, the overall efficiency of the power distribution system can be maximized [4]. To tackle this multifaceted optimization challenge, this research employs the Slime Mould Algorithm (SMA), a novel

56 Nacar Cikan

metaheuristic technique known for its flexibility and effective search capabilities. The SMA's strength lies in its ability to navigate complex optimization landscapes, allowing it to find optimal solutions that achieve a balance between minimizing losses and enhancing voltage stability.

Moreover, the need for advanced optimization techniques is underscored by the growing complexity of modern power distribution systems, driven by factors such as increased energy consumption and the penetration of distributed generation sources. Traditional methods often fall short in addressing these challenges due to their inability to efficiently explore the solution space and manage the inherent trade-offs between competing objectives [5], [6]. The application of SMA [7] in this study not only addresses the intricacies of optimizing PV and capacitor bank allocations but also highlights its potential as a powerful tool for enhancing the stability and reliability of power distribution networks. By optimizing the interplay between renewable energy sources, energy storage solutions, and infrastructure improvements, this research contributes to a more resilient and sustainable energy future.

The remainder of the paper is organized as follows: Section 2 introduces the 33-bus Power Distribution Network (PDN) system and outlines the associated constraints. Section 3 delves into the Slime Mould Algorithm (SMA), detailing its methodology. Section 4 presents the results of the study, along with a discussion of their implications. Finally, the paper concludes with a summary of the findings and their significance.

2. 33-BUS TEST SYSTEM

The 33-bus distribution system depicted in Figure 1 serves as an important reference for analyzing power distribution networks. This network consists of one feeder, 33 buses, and 37 branches, along with five tie switches (T.S.) and 32 sectionalizing switches (S.S.). The total active power demand within the system is 3.72 MW, while the reactive power demand is measured at 2.3 MVAR. Under this configuration, the power loss in the distribution network is calculated to be 202.6771 kW for active power and 135.14 kVAR for reactive power. Additionally, the minimum voltage magnitude in this setup is recorded at 0.9131 p.u., occurring at bus 18. These characteristics highlight the essential parameters of the system, providing a foundation for evaluating its efficiency and performance in various operational scenarios.

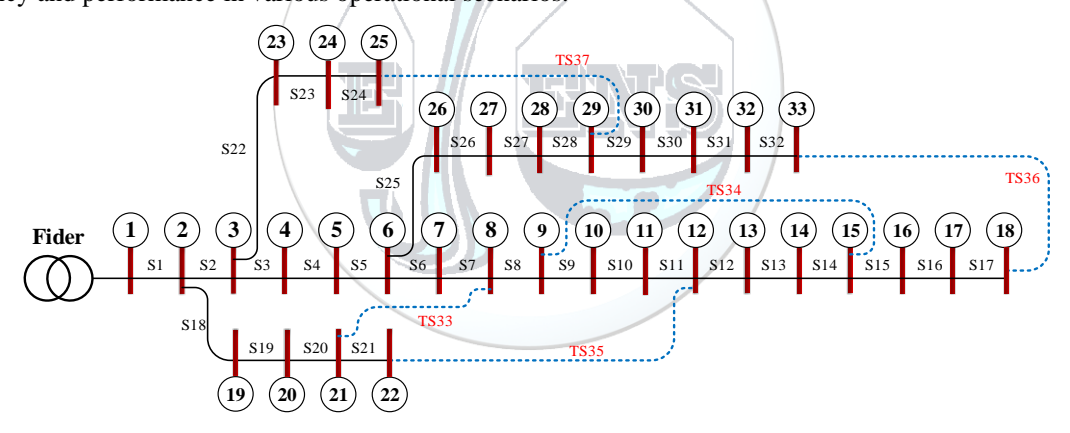


Figure 1. 33-bus test system [5].

2.1. Problem formalization

This study aims to reduce active power loss and improve the voltage stability index. The equation for minimizing power loss is provided in Equation 1. [5].

$$P_{Loss}^{min} = \left(\sum_{i,k=1,}^{N_{br}} r_{(i\cdot k)} \cdot \left(\frac{P_k^2 + Q_k^2}{V_k^2}\right) \cdot Sw_{(i\cdot k)}\right)$$
(1)

Equation 1 provides the formula for enhancing the voltage stability index [5].

$$VSI = \frac{4|V_i|^2|C||D||S_k|\cos(\phi_k + \delta_S).\sin(\delta_i)}{|S_i|^2.\cos^2(\phi_i + \delta_k)} \le 1$$
(2)

A deeper examination is necessary to assess the voltage stability of systems operating close to their limit thresholds. The literature presents numerous voltage stability indices; however, most are based on certain assumptions or oversights. This study utilizes a newly proposed index that incorporates various line

characteristics and is grounded in line loading considerations [2]. It has been observed that the proposed index reliably yields results across different conditions and loading scenarios.

In power systems, voltage fluctuations must be maintained within defined limits, as illustrated in Equation 3. [5].

$$V_{i,\phi}^{min} \le V_{i,\phi} \le V_{i,\phi}^{max}$$
 $\forall \phi \in \{a,b,c\}, \forall i \in Buses$ (3)

The cable within the system must not carry current exceeding the limit specified in Equation 4 [5].

$$I_{i,\phi} \le I_{i,\phi}^{\text{max}} \quad \forall \phi \in \{a, b, c\}, \quad \forall i \in \text{Branches}$$
 (4)

Equation 5 guarantees that the sum of generated power matches the combined total of the load and losses within the system [5].

$$\sum_{i=1}^{N_{Gen}} P_{i,Gen}^{\emptyset} = \sum_{i=1}^{N_{Load}} P_{i,Load}^{\emptyset} + \sum_{i=1}^{N_{Branch}} P_{i,Loss}^{\emptyset} + \sum_{i,Loss} P_{i,Loss}^{equipment} \qquad \forall \varphi \in \{a,b,c\}$$
 (5)

As outlined in Equation 6, transformers must operate within specified voltage and current limits for each phase to ensure optimal performance and avoid potential damage [5].

$$X_{i,\emptyset}^{trfmin} \le X_{i,\emptyset,trf} \le X_{i,\emptyset}^{trfmax} \quad \forall \phi \in \{a,b,c\}$$
 (6)

Equation 7 shows that to ensure line security, the power flow on a line must remain below a specified limit [5].

$$S_{i,\emptyset,line} \le S_{i,\emptyset,line}^{max} \qquad \forall \varphi \in \{a,b,c\}, \quad \forall i \in Lines$$
 (7)

3. SLIME MOULD ALGORITHM

The Slime Mould Algorithm is an innovative optimization technique inspired by the foraging behavior of slime moulds, particularly Physarum polycephalum [7]. This metaheuristic method is distinguished by its ability to explore complex solution spaces effectively while balancing exploration and exploitation. SMA operates through a unique mechanism where agents, representing solutions, mimic the nutrient-seeking movement of slime moulds as they search for food sources [7]. This adaptive behavior allows the algorithm to converge on optimal solutions efficiently by dynamically adjusting to the characteristics of the problem at hand. The algorithm's flexibility makes it suitable for tackling a wide range of optimization challenges, from engineering applications to energy management, thus demonstrating its potential as a powerful tool in the field of computational intelligence [7].

4. RESULTS AND DISCUSSION

Table 1 presents three cases. In Case 1, the system is optimized for 1 PV unit, in Case 2 for 2 PV units, and in Case 3 for 3 PV units. In Case 1, the first PV unit is placed at bus 6, and its maximum power output to the grid is found to be 2575.32 kW. Under these conditions, the active power loss decreases from 202.68 kW to 103.97 kW. The minimum bus voltage is improved from 0.91 to 0.95. This reduction in active power loss corresponds to a 49% decrease. The analytical analysis of the study, which was conducted using a metaheuristic approach, is illustrated in the accompanying figures. As can be seen in the figures, the active power loss is calculated as 103.97 kW when a 2.575 MW DG unit is placed at bus 6.

Table 1. Determination of the sizes and locations of PV panels in the 33-bus test system using the SMA algorithm

Case	DG Type	Location (Bus No)	Size of DG (kW)	Total Size of DG (kW)	Power Factor cos(Φ)	P _{Loss} (kW)	QActive (kVar)	Voltage Stability Index	Minimum Voltage (p.u.)	Bus No at V_{min}	Pactive Loss Reduction (%)
Initial	w/o PV	-	-	-	-	202.68	135.14	0.0379	0.9131	18	0.00
Case 1	1- PV	6	2575.32	2575.32	1	103.97	74.78	0.1796	0.9511	18	48.7037
Case 2	2- PV	13 30 14	846.38 1158.67 753.98	2005.05	1 1 1	85.91	58.55	0.28484 0.25347	0.9685	33	57.6123
Case 3	3- PV	24 30	1099.44 1071.42	2924.84	1 1	71.46	49.39		0.9686	33	64.7433

58 Nacar Cikan

As shown in Table 1, the accuracy of the optimization study performed using the metaheuristic algorithm is verified, as similar results are obtained both from the literature and through the analytical approach. When the same study is conducted for Case 2 and Case 3, the active power losses are further reduced to 85.91 kW and 71.46 kW, respectively.

There are three cases presented in Table 2. In Case 1, the system is optimized by adding 1 capacitor bank, in Case 2 by adding 2 capacitor banks, and in Case 3 by adding 3 capacitor banks. In Case 1, the first capacitor bank is placed at bus 30, and its maximum reactive power output is found to be 1257.2 kW. Under these conditions, the active power loss decreases from 202.68 kW to 143.60 kW. The minimum bus voltage is improved from 0.91 to 0.92. This reduction in active power loss corresponds to a decrease of 29.15%. When the same study is conducted for Case 2 and Case 3, the active power losses are further reduced to 135.74 kW and 132.16 kW, respectively.

Table 2. Determination of the sizes and locations of capacitor tanks in the 33-bus test system using the SMA algorithm

Case	DG Type	Location (Bus No)	Size of DG (kW)	P _{Loss} (kW)	Q ^{Active} Loss (kVar)	Minimum Voltage (p.u.)	Bus No at V _{min}	Pactive Loss Reduction (%)
Initial	w/o PV	-	-	202.68	135.14	0.9131	18	0.00
Case	1-	30	1257.2	143.60	96.30	0.9258	18	29.15%
1	Capacitor							
Case	2-	12	468.87	135.74	90.54	0.9362	18	33.03%
2	Capacitor	30	1057.8					
		13	378.69	132.16	88.32	0.9383	18	34.80%
Case	3-	24	544.21					
3	Capacitor	30	1036.7					

A multi-objective approach was implemented in this study. To demonstrate the effectiveness of the algorithm, three different cases were considered. The peak load value of the electric vehicle (EV) charging stations was set to 500 kW. Assuming that the minimum charging power of a vehicle is 50 kW, approximately 10 vehicles can be charged simultaneously. In Table 3, the PV, capacitor banks, and EV charging stations were optimally located in the 33-bus test system simultaneously. Moreover, the sizes of the PV units and capacitor banks were optimized simultaneously.

Table 3. PV, Capacitor and EV charging stations

			a	A -M	A -M		3.51.1		A -+!
Case	DG	Location	Size of	P _{Loss}	Q _{Loss}	Voltage	Minimum	Bus	P _{Loss}
	Type	(Bus	DG /	(kW)	(kVar)	Stability	Voltage	No	Reduction
		No)	EV			Index	(p.u.)	at	(%)
			(kW)					V_{min}	
Initial	w/o PV	-	-	202.68	135.14	37.9e-3	0.9131	18	0.00
~				70 400	40.04=		0.044	4.0	= 2 0201
Case 1	1 st PV	6	2538.89	52.688	40.917	6.35e-3	0.962	18	73.92%.
	1 st	30	1251.09						
	Cap 1 st	2	500.00						
	EV								
Case	1 st	12	1466.29	29.724	20.957	1.42e-3	0.980	25	85.32%
2	PV								
	1 st	12	455.14						
	Cap 1 st	10	500.00						
	EV	12	500.00						
	2^{nd}	30	1095.5						
	PV								
	2^{nd}	30	1040.3						
	Cap								
	2 nd	2	500.00						
C	EV	2.4	1140.0	15.504	12.00	5 40 0	0.002	0	02.240/
Case	1 st	24	1143.3	15.504	12.08	5.43e-3	0.992	8	93.34%

3	PV			
	1 st	14	335.9	
	Cap			
	1 st	2	500.00	
	EV			
	2^{nd}	30	1065.3	
	PV			
	2^{nd}	3	797.46	
	Cap			
	2^{nd}	2	500.00	
	EV			
	3^{rd}	14	755.97	
	PV			
	3^{rd}	30	994.17	
	Cap			
	3^{rd}	2	500.00	
	EV			

It was assumed that the PV units can supply power to the system within the range of 0 to 4 MW, and similarly, capacitor banks can provide reactive power within the range of 0 to 4 MVAR. In Case 1, 5 parameters were optimized, which are: PV location and size, capacitor bank location and size, and EV location. As a result, the PV was placed at bus 6, the capacitor bank at bus 30, and the EV charging station at bus 2. It was observed that these locations were consistent with the results obtained for PV and capacitor banks. The size values also produced similar results. The EV charging station was optimally located near the feeder bus (bus 1) at bus 2. When Cases 2 and 3 were examined, it was found that the optimal location results in the multi-objective study were quite similar to those obtained when PV was optimized individually. The number of optimized parameters in the multi-objective approach was 5 in Case 1, 10 in Case 2, and 15 in Case 3. Despite the presence of renewable energy sources in the system, when considering configurations with minimum power losses, it was observed that the EV charging stations were optimally located near the feeder bus.

5. CONCLUSION

In conclusion, the optimal allocation and sizing of distributed generation sources such as PV units, capacitor banks, and EV charging stations play a crucial role in enhancing the overall performance of distribution networks. The results from the multi-objective optimization cases demonstrated that proper placement of these components significantly reduces active power losses and improves voltage profiles. Furthermore, the findings indicate that EV charging stations are optimally located near the feeder bus to minimize power losses, even when integrated with other DG sources like PV and capacitors. The consistency between the obtained results and analytical analyses confirms the accuracy and robustness of the proposed approach, making it an effective strategy for addressing complex optimization problems in power distribution systems.

ACKNOWLEDGMENT

The author gratefully acknowledges the support provided by TÜBİTAK within the scope of the 1001 project under grant number 124E002.

CONFLICT OF INTEREST STATEMENT

The author declares that there is no conflict of interest.

REFERENCES

- [1]. M. Çıkan, "Çita optimizasyon algoritması kullanarak kısmi gölgelenme altındaki fotovoltaik sistemlerde maksimum güç noktası izleyicisinin tasarlanması," *Gazi Üniversitesi Mühendislik Mimarlık Fakültesi Dergisi*, vol.40, pp.555-572.
- [2]. M. Çıkan and K. Dogansahin, "A Comprehensive Evaluation of Up-to-Date Optimization Algorithms on MPPT Application for Photovoltaic Systems," *Energy Sources, Part A: Recovery, Utilization, and Environmental Effects*, vol. 45, pp.10381-10407.
- [3]. M. Çıkan and N. Nacar Çıkan, "Optimum allocation of multiple type and number of DG units based on IEEE 123-bus unbalanced multi-phase power distribution system," *International Journal of Electrical Power & Energy Systems*, vol.144, pp.108564.
- [4]. M. Çıkan and N. Nacar Çıkan, "Elektrikli araç şarj istasyonlarının enerji dağıtim hatlarına optimum şekilde konumlandırılması," *Kahramanmaraş Sütçü İmam Üniversitesi Mühendislik Bilimleri Dergisi*, vol.27, pp.340-363, Jun. 2024.

Nacar Cikan

[5]. M. Çıkan and B. Kekezoglu, "Comparison of metaheuristic optimization techniques including Equilibrium optimizer algorithm in power distribution network reconfiguration," *Alexandria Engineering Journal.*, vol.61, pp.991-1031.

- [6]. N. Nacar Çıkan and M. Çıkan, "Reconfiguration of 123-bus unbalanced power distribution network analysis by considering minimization of current & voltage unbalanced indexes and power loss," *International Journal of Electrical Power & Energy Systems*, vol.157, pp.109796.
- [7]. S. Li, H. Chen, M. Wang, A.A. Heidari, and S. Mirjalili, "Slime mould algorithm: A new method for stochastic optimization," *Future Generation Computer Systems*, vol.111, pp.300-323.



Numerical Simulation of Mass Transfer Mechanism of Stratospheric Solar Powered Telecommunication Balloons

Öznur KAYHAN*

¹Gebze Technical University, Department of Chemical Engineering, 41400, Gebze/Kocaeli, Turkey. *Corresponding Author email: <u>okayhan@gtu.edu.tr</u>

Abstract

Stratospheric balloon systems, which have the ability to fly for longer periods of time such as months or even a year in 20 km or higher layers of the atmosphere, have been an elusive goal to achieve in recent years. It is critical issue to resolve the energy matter of stratospheric balloon to supply unmanned vehicles working at target altitudes for extended durations. As an ideal alternative, solar power units are supplied to the balloons by mounting them on the balloon's envelope and classified as solar powered balloons. This method can cause the buoyant gas inside the balloon to overheat and pressurize, leading to further gas leakage from the balloon's polymeric material. In this investigation, modeling of the mass transfer mechanism of a solar-powered zero-pressure balloon has been set up and simulated using iterative techniques in Fortran program for the first time in literature. The simulation has been run for solar powered balloon flight under one of the cities of Turkey's real atmospheric conditions including solar radiation flux and wind velocities. The temperature variation of interior helium and mass transfer coefficient and diffusion coefficient with thermal effect have been analyzed and compared with the unpowered stratospheric balloon in summer season conditions. The maximum temperature, mass transfer coefficient and diffusivity of the interior helium for solar powered and unpowered balloon is obtained as 350.51 K, $1.74 \times 10^{-2} \text{ m/s}$, $0.83 \times 10^{-8} \text{ m/s}^2$ and 310.49 K, $1.48 \times 10^{-2} \text{ m/s}$, $0.78x10^{-8}$ m/s² respectively. These results will be helpful to design the solar powered balloon systems to stay at higher altitudes for longer durations.

Keywords

Mass Transfer, Diffusion, Solar Energy, High Altitude, Zero Pressure Balloons

1. INTRODUCTION

Stratospheric balloons filled with helium or hydrogen as lifting gases can reach to the higher altitudes 20.0 km to 36.5 km altitude or even higher providing a unique vantage point for civilian applications as a low cost alternative telecommunication platform to satellite, a continuous wide area coverage for key areas of interest for observation for the military, carrying equipments of several tons to desired altitude of the stratosphere for scientific experiments. Accordingly, it has been attractive goal for many years to gain the ability to the balloons controlling them for longer durations even years at high altitude. Renewable based power system is required to keep the balloon at high altitudes for extended duration. Solar energy which is power unit of photovoltaic (PV) array coupled to an energy storage system is the unique power choice for the stratsopheric unmanned platforms. Solar energy is converted into electrical energy via PV by photoelectric and photochemical effects during

62 Kayhan

daytime, and during night time, power to the balloon is supplied to the balloon by the energy storage system [1,2].

The PV can be positioned separately from the balloon as a load or mounted within the balloon envelope as seen in the Fig.1 [3]. When the photovoltaic panel is placed on the balloon's envelope, the heat transfer from the panel to the balloon envelope can cause the superheating and over-pressure of the balloon which affects the reliability, and duration of the balloon [4] and superheating effect on mass transfer mechanism should be investigated to predict the leakage amount of lift gas through the balloon's polymeric material before launch. In recent years, the energy problem and thermal performance of high-altitude unmanned vehicles has been analyzed by some researchers. Yang and Liu [5] introduced renewable power system's composition for stratospheric airships and established solar array's curved paving model. In addition, they proposed the high accuracy calculation method to obtain output power of solar array. Liu et al. [6] proposed a numerical model to simulate stratospheric airship's thermal performance with photovoltaic array and they developed an analysis code based on the thermal model and accomplished verification by experimental data. Zang et al. [7] proposed a simplified thermal model of a high-altitude hybrid airship with a photovoltaic module array (PVMA), and simulated based on computational fluid dynamics(CFD), using a user defined function (UDF) program, to analyze PVMA's thermal effects on the hybrid airship. Sun et al. [8] developed first multilayer insulation material (MLI), and they carried out low temperature environment test for verification of the insulation effect of MLI. Sun et al. [9] studied the influence of cracks caused by external forces as thermal stress on the output of solar arrays of stratospheric airships under different conditions. They proposed crack modeules for simulation method and analyzed relationship between output characteristics and the failure extent of cracked modules. Zhu et al. [10] suggested energy model and the solar radiation model for high-altitude solar-powered airships to compute their energy consumption and production. Dai et al. [11] proposed a new model to measure airship's thermal performance and presented three dimensional distribution and temperature variation of solar powered airship. Additionally, they did the description of solar array effects on the thermal performances of a stratospheric airship.

There is no research has been published about mass transfer mechanism of the solar powered balloon in real field in literature. Some researchers have neglected the variation of the inner pressure of a lift gas and regarded total volume as constant during the flight. In this research paper, solar-powered zero-pressure balloons based on a gas compress release system has been studied to analyze the effect of the thermal environment on the mass transfer mechanism in real seasonal regions. The real time analysis of mass transfer model of a solar-powered zero-pressure balloon has been set up and simulated in Fortran via iterative techniques.

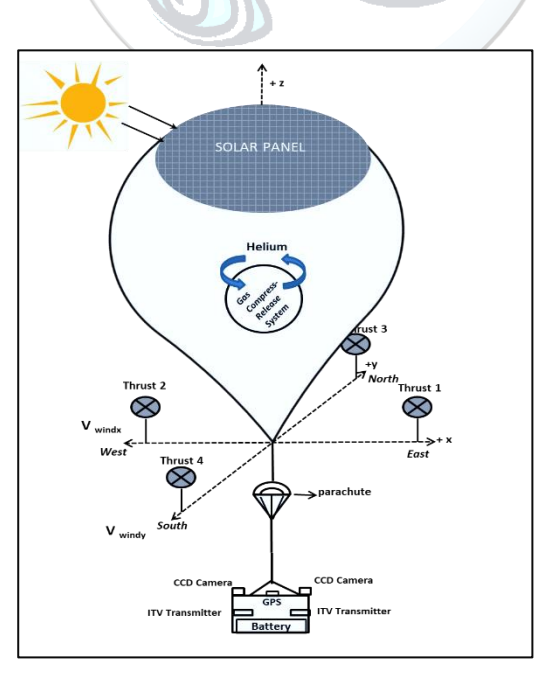


Figure 1. A sketch of the solar powered balloon system

2. MASS TRANSFER MECHANISM

In stratospheric balloons, the inner gas leaks out through the balloon material over time. Three steps can be determined for inner gas mass transfer mechanism: (1) inner gas transfers through the inner balloon surface by convection, (2) inner gas transfers from inner surface of the balloon to the outer surface by diffusion, (3) from outer surface of the balloon to the atmosphere by convection. The mass and the number of moles of inner gas are obtained by calculating the escape of the gas. The mass transfer mechanism of gas can be shown schematically on a balloon film of Δx thickness, as in Fig.2. The inner gas flux equation can be obtained as the following equation 1 considering Fig. 2 for small wall thicknesses.

$$N_g = k_{ci}(C_{gin} - C_{ins}) = D_{re} \frac{(C_{ins} - C_{os})}{\Delta x} = k_{co}(C_{os} - C_{go})$$
(1)

where " N_g " denotes the lifting gas flux (kmol/m². s), " k_{ci} " and " k_{co} " denotes the convective mass transfer coefficient at the inside and outside of the balloon surface, " D_{re} " denotes the real effective molecular diffusivity (m²/s), " C_{ins} " and " C_{os} " denotes lifting gas concentration (kmol/m³) at the inside and outside of the balloon wall, " C_{gin} " and " C_{go} " denotes the inside and outside concentration of the lifting gas (kmol/m³).

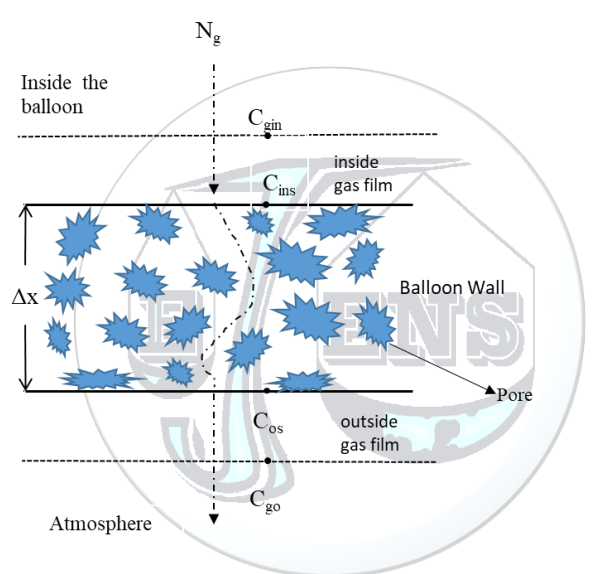


Figure 2. Mass transfer mechanism of lift gas through the balloon wall.

From Eq. (1), differential leakage amount of the lift gas can be obtained as follows

$$dn_{_{o}} = N_{_{o}}A_{_{e}}dt \tag{2}$$

where " A_e " is effective mass transfer area, "dt" is time step. Real effective diffusion coefficient, (D_{re}) is a parameter that critically affects the mass transfer rate. By using Chapman Enskog equation, molecular diffusivity of a gas can be calculated as follows[12,13]

$$D = \frac{1.85X10^{-7}T^{3/2}}{P\sigma^2\Omega} \left(\frac{1}{M_q} + \frac{1}{M_q}\right)^{0.5} \tag{3}$$

where "D" is molecular diffusivity (m^2/s) , " M_g " is molecular weight of lift gas and " M_a " is the molecular weight of the air, (kg/kmol), "P" is pressure (Pa), "T" is temperature (K). Balloon walls contain of pores. Considering gas diffusion through these pores, effective diffusivity (D_e) is calculated by [14]

64 Kayhan

$$D_e = (\mathcal{E}/\mathcal{T}) D \tag{4}$$

In porous structures, if the mean free path is larger than the pore size, the form of molecular transfer is Knudsen flow. In this case, molecules will collide with each other and the walls of the medium. Therefore, there will be a transition from molecular diffusion to Knudsen diffusion and Knudsen diffusion will be dominant and be calculated by Eq.(5) [15]

$$D_k = \frac{2}{3} r_p \sqrt{\frac{8R_u T}{\pi M_g}} \tag{5}$$

where " D_k " is knudsen diffusivity (m^2/s), " r_p " is pore radius (m). The effective diffusion coefficient is calculated by taking into account the effective Knudsen in Eq.6 and the real diffusion coefficient is calculated by Eq.7 [16]. Thus, the effect of Knudsen diffusion is reflected in the mass transfer mechanism.

$$D_{ke} = (\mathcal{E}/\mathcal{T}) D_k \tag{6}$$

In the Eq.(4) "ε" represents porosity of balloon wall material and "Ţ" represents tortuosity. Real effective regarding knudsen diffusion and molecular diffusion can be obtained as following equation.

$$\frac{1}{D_{re}} = \frac{D_e + D_{ke}}{D_e D_{ke}} \tag{7}$$

Convective mass transfer coefficients " k_{ci} " and " k_{co} " (m/s) are calculated by using dimensionless numbers from Eq. 8

$$k_c = \frac{D}{D_h} (2 + 0.6Re^{0.5}Sc^{0.33})$$
 $1 \ll Re \ll 48,000 \ 0.6 \ll Sc \ll 2.7$ (8)

Where "D_b" is balloon diameter (m), "Re" is Reynold Number, "Sc" is schmidt number [17,18].

3. NUMERICAL METHOD

The solar-powered zero-pressure balloon-assisted gas compress release system is developed and coded by combining some subroutines such as transport phenomena (momentum, mass, and heat transfer) by using Fortran Program. The iterative technique as a numerical method is used to solve the system. For the examination of the mass transfer performance of solar-powered zero-pressure balloons in real atmospheric conditions, Erzurum the city in Turkey has been determined as a flight station. As a summer day 14th day of August have been chosen for simulation. The balloon system has managed to reach the desired altitude of 16.785 km for the available wind data. To resist the wind drag acting on the solar-powered balloon system, thrust power is supplied to manipulate the wind force to establish station keeping.

In this research, the leading numerical program consists of subroutines to solve the mass transfer model of the solar-powered balloon is shown schematically in Fig.3, and design parameters are listed in Table 1. The differential equation of temperature changes in the program has been solved by an initial value method named the Euler method which calculates T at time step (t+1).

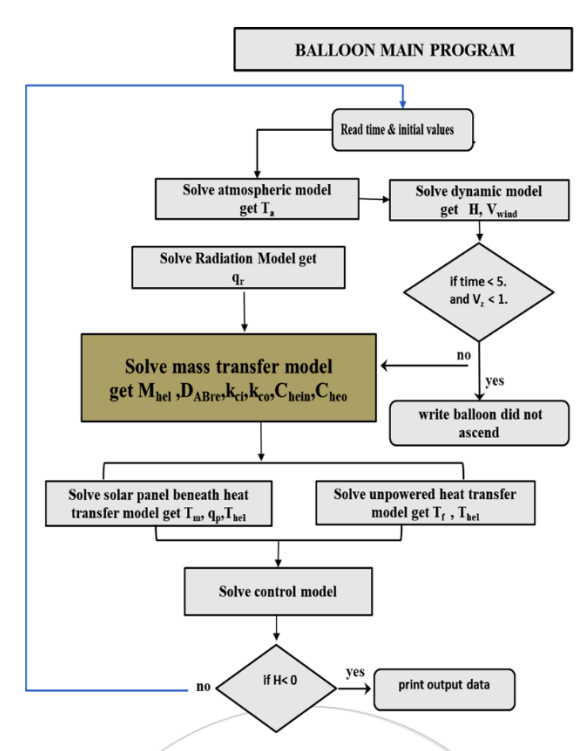


Figure 3. Balloon Main Program Flow Chart

Table 1. The design parameters of the solar powered balloon

Balloon		Solar Panel	
Volume, m ³ (max)	20,135	Absorptivity	0.9
Diameter, m (max)	33.754	Emissivity	0.9
Envelope area, m² (max)	3579.22	Type Flexible thin film amorphous silicon	
Absorptivity of envelope	0.33	Conversion efficiency	%7.5
Emissivity of envelope	0.8	Temperature coefficient, % 1/K	0.01
Thickness, mm	8.0	Thickness, mm	0.2
Helium Weight , kg 500			
Stored Helium Weight, kg 500			
Equipment Weight, kg 500			

4.RESULTS AND DISCUSSION

 14^{th} day of August balloon flight has been simulated in real environment and mass transfer model has been observed to analyze the performance of the balloon's mass transfer mechanism. Fig.4 depicts the simulation of the mass transfer model results during day-night cycle of the solar powered baloon flight at the target altitude. It can be seen from the Fig. 4, when temperature of helium increases and reaches to the maximum value at noon time, real molecular diffusivity of the helium through the balloon wall (D_{re}) and mass transfer coefficients of helium through the wall (k_{ci}) and mass transfer coefficient of helium (k_{co}) through the atmosphere increases and reaches maximum values of $16.75 \times 10^{-8} \, \text{m}^2/\text{s}$, $1.09 \times 10^{-2} \, \text{m/s}$, respectively as seen in the Table 2.

66 Kayhan

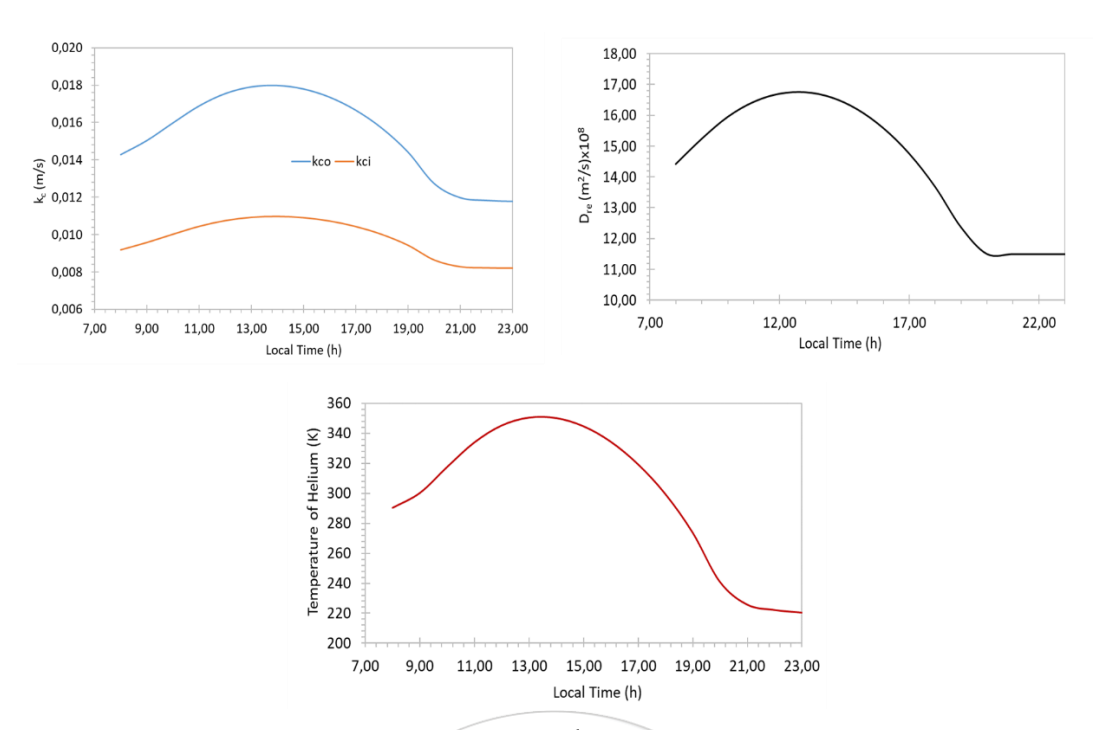


Fig.4. Mass Transfer output of 14th August flight at 16.785 km

As seen from the Fig.5. inner helium weight and concentration decreases till the noon time due to increasing of the mass transfer rate as seen in the Fig.4. When inner concentration of the helium decreases, from the storage helium is started to pump into the balloon with control manner not to loose the altitude control and keep the balloon at the target altitude. Therefore after noon time concentration of helium increases by gas compress release cycle unit of the balloom.

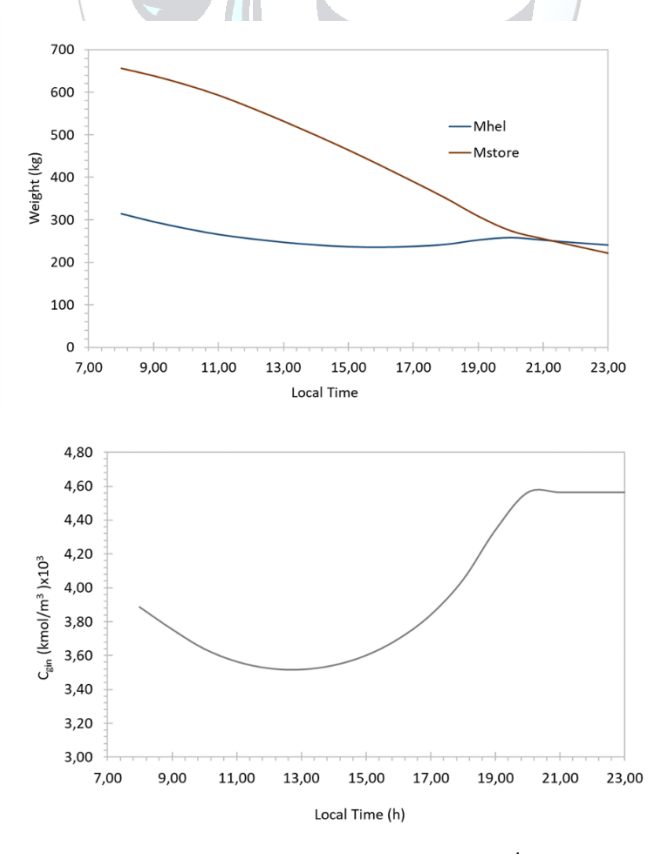


Fig.5. Concentration and weight of helium output of 14th August flight at 16.785 km.

To obtain longer flight duration, mass transfer coefficient and diffusivity of helium could be reduced by reducing the " ϵ /T". In real flight by the help of compress-release cycle of the helium, when the " ϵ /T" decreased from the 2.25x 10^{-4} to 1,125x 10^{-4} , the flight time could be increased 95 hours as seen in the Figure 6 and Table 2 and for longer duration as 26 days, " ϵ /T" should be available as 4.9 x 10^{-5} .

		32 Hours Flight a	it 16.785 km altitude			
Launch Day :14 th August	Local Time	Thel (K) (max)	K _{co} (m/s) (max)	Kci (m/s) (max)	D _{re} (m ² /s) (max)	(ε/ <u>T</u>)
solarpowered balloon	13:00	350,51	1,8x10 ⁻²	1,09x10 ⁻²	16,75x10 ⁻⁸	2,25x10 ⁻⁴
unpowered balloon	13:00	310,31	1,6x10 ⁻²	1x 10 ⁻²	16,75x10 ⁻⁸	2,25x10 ⁻⁴
		127 Hours Flight	at 16.785 km altitude			
		Thel (K) (max)	K _{co} (m/s) (max)	K _{ci} (m/s) (max)	$D_{re} (m^2/s) (max)$	(ε/ <u>T</u>)
solarpowered balloon	13:00	350,53	1,75x10 ⁻²	1,07x10 ⁻²	4,19x10 ⁻⁸	1,125x10 ⁻⁴
unpowered balloon	13:00	310,46	1,55x10 ⁻²	0,98x10 ⁻²	4,19x10 ⁻⁸	1,125x10 ⁻⁴
		26 Days Flight at	: 16.785 km altitude			
		Thel (K) (max)	K _{co} (m/s) (max)	K _{ci} (m/s) (max)	Dre (m ² /s) (max)	(E/T)
solarpowered balloon	13:00	350,46	1,74x10 ⁻²	1,06x10 ⁻²	0,83x10 ⁻⁸	4,9x10 ⁻⁵
unpowered balloon	13:00	310.49	1.48x10 ⁻²	1x10 ⁻²	0.78x10 ⁻⁸	$4.9x10^{-5}$

Table 2 Mass Transfer output data of August flights at 16.785 km

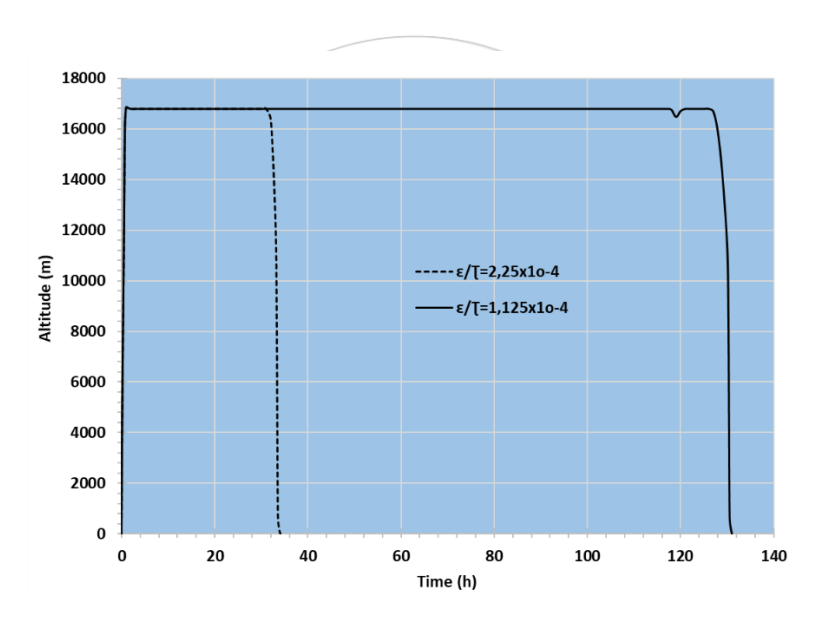


Figure 6. Trajectory of Balloon Flights

5. Conclusion

The flight time of solar powered balloon is a strong function of the real effective diffusion coefficient of lifting gas, " D_{re} " and porosity tortusity ratio, " ϵ /T" of balloon wall material. Compared with the unpowered balloon, the temperature variation of internal helium of the solar powered balloon is not notable for diffusivity of lifting gas during the day night cycle of the flight but it slightly effects the convective mass transfer coefficients, " k_{ci} , k_{co} " of the lifting gas. When " ϵ /T" is % 50 decreased, flight time extended 95 hours. The maximum temperature, mass transfer coefficient and diffusivity of the interior helium for solar powered and unpowered balloon is obtained as 350.51 K, 1.74 x 10^{-2} m/s, 0.83×10^{-8} m/s² and 310.49 K, 1.48×10^{-2} m/s, 0.78×10^{-8} m/s² respectively to reach 26 days flight. Up to the present, there is no study of mass transfer performance of solar powered zero pressure balloon to observe and control the helium lekage through the balloon wall. In conclusion, the outcomes of this research would be beneficial to plan solar energy system to keep the balloon at target altitude for months, even years. Future work involves doing the mass transfer experimentally and validate the result with the proposed mathematical mass transfer model.

68 Kayhan

CONFLICT OF INTEREST STATEMENT

The author(s) declare(s) that there is no conflict of interest.

REFERENCES

- [1] Ö. Kayhan and M.A. Hastaoğlu, Modeling of Stratospheric Balloon Based on Transport Phenomena and Gas Compress -Release System, Journal of Thermophysics and Heat Transfer, vol. 28, pp. 534-541, 2014.
- [2] Ö. Kayhan, A thermal Model to Investigate the Power Output of Solar Array for Stratospheric Balloons in Real Environment. Applied Thermal Engineering, vol. 53, pp.113-120, 2018.
- [3] Ö. Kayhan, Effect of Thermal Environment on Heat Transfer Mechanism of Solar Powered Balloon, Journal of Thermophysics and Heat Transfer (2024), accessed Oct 23, 2024: https://doi.org/10.2514/1.T6896
- [4] Q. Liu,, Y. Yang,, Y. Cui,, J. Cai,, Thermal Performance Analyses of Stratospheric Airship with Photovoltaic Array, *Advances in Space Research*, Vol. 59, pp. 1486-1501, 2017.
- [5] Yang, X., Liu, D., "Renewable power system simulation and endurance analysis for stratospheric airships," *Renewable Energy*, Vol. 113, 2017, pp. 1070-1076. https://doi.org/10.1016/j.renene.2017.06.077
- [6] Liu, Q., Yang, Y., Cui, Y., Cai, J., "Thermal performance of stratospheric airship with photovoltaic array," *Advances in Space Research*, Vol. 59, 2017, pp. 1486-1501. https://doi.org/10.1016/j.asr.2016.12.029
- [7] Zhang, L., Li, J., Meng, J., Du, H., Lv, M., Zhu, W., "Thermal Performance Analysis of a High-Altitude Solar-Powered Hybrid Airship," *Renewable Energy*, Vol. 125, 2018, pp. 890-906. https://doi.org/10.1016/j.renene.2018.03.016
- [8] Sun, K., Yang, Q., Yang, Y., Wang, S., Xu, J., Liu, Y. Xie, P. L., "Thermal Characteristics of Multilayer Insulation Materials for Flexible Thin-Film Solar Cell Array of Stratospheric Airship," *Advances in Materials Science and Engineering*, Vol. 8, 2014, pp. 1-8. https://doi.org/10.1155/2014/706308
- [9] Sun, K., Zou, T., Gao, J., Shan, C., Ji, X., "Impact of cracks in solar array on output power of stratospheric airship", Solar Energy, 2024, Vol. 267, pp. 112234. https://doi.org/10.1016/j.solener.2023.112234
- [10] Zhua, W., Zhanga B., Zhangb L., Xuc, Y., Yanga, K., "Spatial path analysis for high-altitude solar-powered airship with maximum net energy", Aerospace Science and Technology , 2021, Vol. 117, pp. 106922. https://doi.org/10.1016/j.ast.2021.106922
- [11] Qiumin Daia, Lin Caoa, Gaogao Zhanga, Xiande Fangb,* Thermal performance analysis of solar array for solar powered stratospheric airship, Applied Thermal Engineering, 171, 2020, 115077. https://doi.org/10.1016/j.applthermaleng.2020.115077
- [12] S. Chapman, and T. G. Cowling, "Mathematical Theory of NonUniform Gases," Cambridge Univ. Press, 1970, pp. 176–267.
- [13] J. O Hirschfelder, C. F. Curtiss,, and R. B. Bird, Molecular Theory of Gases and Liquids, Wiley, New York, 1964, p. 539.
- [14] M. A. Hastaoglu, "Transient Modeling of a Packed Tower: Mass and Heat Transfer with Reaction," Fuel, Vol. 74, No. 11, pp. 1624–1631, 1995.
- [15] J. M. Thomas, and W. J. Thomas, Principles and Practice of Heterogeneous Catalysis, VCH Publishers Inc., New York, 1997, pp. 294.
- [16] W. E., Stewart, and M. F. L. Johnson,, "Pore Structure and Gaseous Diffusion in Solid Catalysts," Journal of Catalysis, Vol. 4, No. 2, 1965, pp. 248–252.
- [17] W. E., Ranz, and W. R., Marshall, "Evaporation from Drops, Part I," Chemical Engineering Progress, Vol. 48, No. 3, 1952, pp. 141–146
- [18] W. E., Ranz, and W. R., Marshall, "Evaporation from Drops, Part II," Chemical Engineering Progress, Vol. 48, No. 4, 1952, pp. 173–180.

Hydraulic Rebound Stopper Affect For Passsenger Cars On Shock Absorber

Semih Calli¹

¹Maysan Mando, R&D Design Engineer, 16245, Osmangazi/Bursa, Turkey. *Corresponding Author email: scalli@maysanmando.com

Abstract

The vehicles driving on the road, road-related impacts affect the chassis. These impacts should not be transmitted to the cabin. The That absorbs these impacts between the chassis and cabin is the shock absorber. The shock absorber does this damping by converting motion energy into heat energy. During this energy conversion, the hydraulic flow inside the shock absorber is limited by piston valve. The valve damping force is adjustable according to vehicle type for the passive Shock Absorbers and occurs reaction forces during driving. However, the damping force must be variable in order to meet driving dynamics and driver expectations that change over time. Active shock absorbers are used to provide this variability. However, active shock absorbers are more costly and more difficult to implement. For this reason, different technologies such as hydraulic rebound stopper and hydraulic compression stopper are used in passive shock absorbers to ensure the variability of force. In this study, comparative numerical data were obtained by applying the hydraulic rebound stopper system to the shock absorbers used in small family cars and lower middle-class cars. In road conditions where the reaction force of the valve against the hydraulic fluid is not sufficient, the hydraulic rebound stopper is activated by creating extra force. With this extra force, disturbing vibrations to the vehicle and the driver are dampened, increasing driving safety and comfort.

Keywords

Shock absorber, Hydraulic Rebound stopper, Hydraulic flow, Piston Valve

1. INTRODUCTION

Shock absorbers used in passenger cars are hydro-mechanical parts that overcome road-related vibrations that occur during driving without breaking the wheel's contact with the road, with hydraulic reaction force, this increasing driving safety and comfort. Basically, it has an oil-filled cylinder group and a piston that can move vertically.

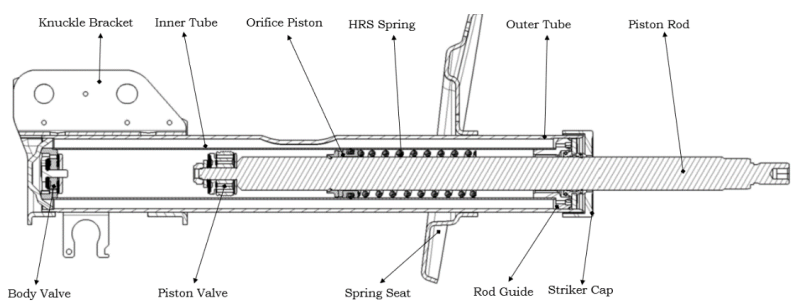


Figure 1. Shock absorber components

70 Calli

This piston rod moves up and down, compressing or releasing the oil in the shock absorber with the help of valves, providing damping. There are two types of valves working inside the shock absorber. These valves adjust the flow rates of the oil that will create the compression or rebound forces of the oil inside the shock absorber. Firstly, the piston starts its upward movement when the vehicle falls into a pothole. While this upward movement occurs, the washers in the piston valve make it difficult for the oil to passover. The oil is forced to pass through the washers, creating a rebound force. The rebound force may vary depending on the number of washers and the type of piston. The oil creates a rebound force as it is forced to pass through the valves for rebound. This makes the rebound force adjustable according to the weight of the vehicle and driving comfort. It dampens the force that will come to the vehicle with the rebound force before it reaches the driver. Driving safety and driver comfort increase with the damping of this force.

When the vehicle hits the bump, the piston starts moving in the opposite direction. It tries to compress the oil in the shock absorber with the help of valves by moving downwards in a variable direction according to the height of the bump. When the movement starts, the oil starts to create a compression force by passing through the washers. This force can be adjusted with the help of washers or the variability of the valves. As the compression force is formed, the piston rod starts to move down further. The force continues to increase to the lowest point of the shock absorber. The force creates a damping force in the vehicle in proportion to the compression of the oil. With the damping, the force that will come to the vehicle while passing through the bump is eliminated. In addition, the driver's control of the vehicle remains constant and driving comfort is increased.

When we explain the working principle of the shock absorber, there are force graphs where we measure the performance of the shock absorber, where we match the verbal expressions with scientific data. The reaction forces that form the curves in these force graphs are the reaction forces given by the valves to the measuring device. Performance graphs vary according to speeds and incoming forces, and the shock absorber completes the force data in the curve by completing an up-down movement.

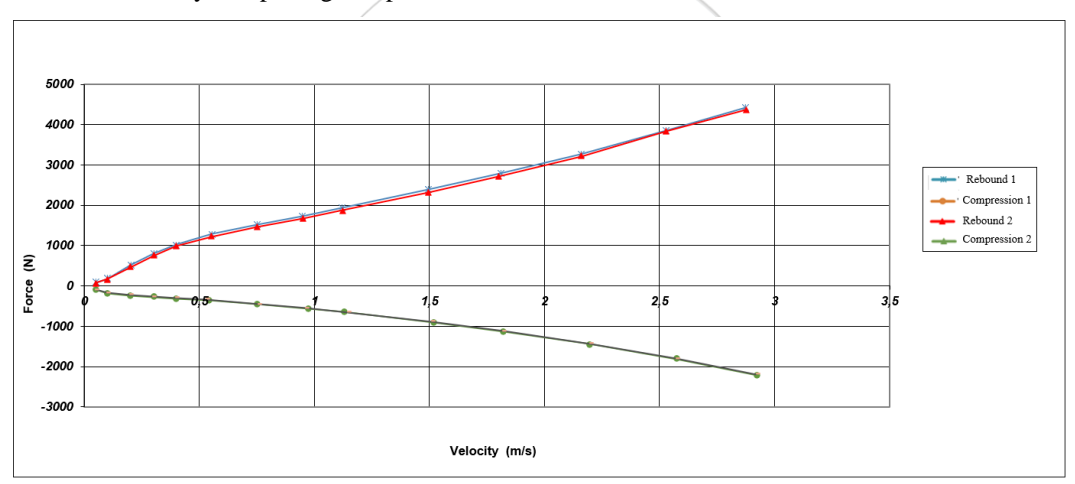


Figure 2. Shock absorber Damping Forces Chart

1.1 HYDRAULIC REBOUND STOPPER

Hydraulic Rebound Stopper is a hydraulic stop that dampens when the vehicle enters a pothole and is an add-on function for conventional shock absorbers. The hydraulic rebound stopper creates an additional damping force while working inside the shock absorber. It produces this additional force by compressing the oil with a different piston assembly and the compressive force of the spring used in the shock absorber. In this way, the high rebound stop forces that occur when the cars enter potholes are reduced in a controlled manner, this reducing the vibrations and noises coming to the driver. The graphic created by the hydraulic rebound stopper is defined as follows.

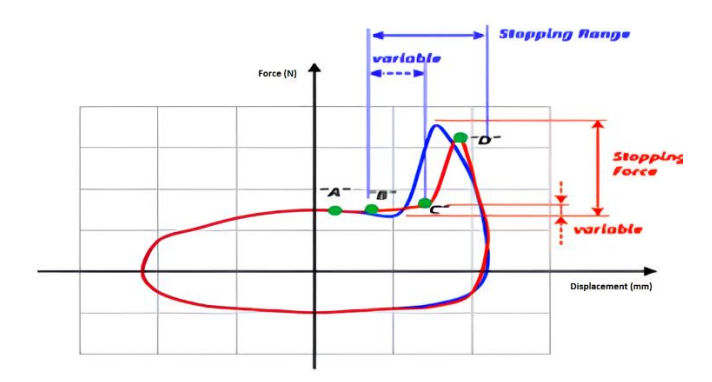


Figure 3. Hydraulic Rebound Stopper Diagram

2. MATERIALS AND METHODS

The most important titles for the HRS system are the amount of force and damping, HRS movement length, HRS starting point, adjustable force, sealing to create damping within the system and the fact that these features are easily adjustable or suitable for variability. A testing machine can obtain these parameters by measuring the shock absorber reaction force. Prototype production is important for this situation. Prototype production was produced with test springs and injection molded parts and tests and trials were carried out. After trying many designs, these trials were brought to dimensions suitable for placement in the shock absorber and tested. Adjustable shock absorbers made in the form of prototypes also provided fast testing opportunities.

2.1. HRS System Design of Parts

The most important factors affecting shock absorber designs are that the shock absorber performs its damping function as a suspension element well and provides durability and damping throughout the life of the vehicle. Other factors are its suitability for vehicle assembly, its adaptation to the flow and dynamism of the vehicle while working with the suspension in the vehicle, and its damping by providing the driver with road control without losing contact with the road during damping. While designing and developing this hydraulic rebound stopper system, a design was created to fit the inner tube inside the shock absorber. All parts in the system were designed in accordance with these limits and placed inside the shock absorber without hindering operation. The HRS system consists of a rebound spring, orifice piston, o-ring and hydraulic rebound bumper. Figure 4 shows the parts of the hydraulic rebound stopper system.

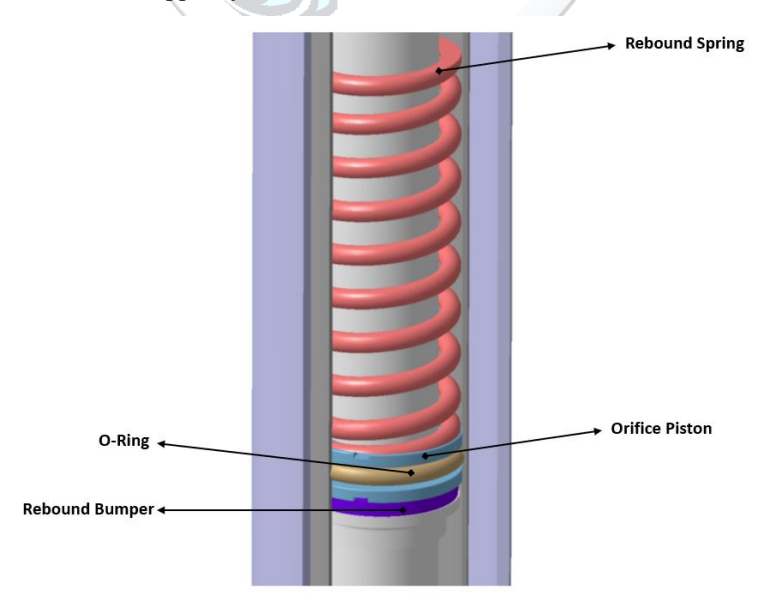


Figure 4. Parts Of Hydraulic Rebound Stopper

72 Calli

2.1.1 Rebound Spring

The most important factors in the design of the rebound stopper spring are the weight of the vehicle it is used in, the damping required while driving on the road, and the additional damping force it creates compared to a normal shock absorber. In addition, the height of the spring determines where the rebound stopper force will come into play. The number of spring coefficient determines how much force will increase or decrease in the vehicle. This number of spring coefficient and the height of the spring also determine the shock absorber damping force measurement graph. For this reason, the most optimum design was selected and an adjustable spring design was obtained according to the vehicle type.



Figure 5. Rebound Stopper Spring

2.1.2 Orifice Piston

The first priority in orifice piston design is to provide suitable dimensions that can be mounted inside the inner tube. Then, it provides this extra force by compressing the oil by providing sealing in order to create an additional hydraulic force inside the shock absorber. It increases the damping force by not allowing the oil to pass with the o-ring mounted on it. This damping force can be adjusted with the variable grooves on it. The most suitable groove size is determined according to the vehicle and a universally usable design is created and applied to the shock absorber.

Figure 6. Orifice Piston

2.1.3 *O-Ring*

The o-ring must have dimensions that can be mounted on the orifice piston and that will seal inside the inner tube. Therefore, when selecting the material, rubber material was preferred instead of a hard plastic. Then, the dimensions were determined so that the oil in the shock absorber would not leak under the orifice piston and this dimension was adjusted so that it could be mounted on the orifice piston.



Figure 7. O-ring

2.1.4 Hydraulic Rebound Bumper

The most important criterion in the design of the hydraulic rebound buffer is to minimize the force coming from the hydraulic rebound stopper system while it is working and to minimize the sound that will reach the driver without breaking during operation by withstanding high heat in every operation. Therefore, the selected material is of great importance. Here, a material that can provide long-term durability, is heat-resistant and reduces noise according to the vehicle is selected. The part under the orifice piston is designed in accordance with the inner tube and piston rod dimensions and made operational within the system.



Figure 8. Hydraulic Rebound Bumper

3. RESULTS AND DISCUSSION

After the designs were made, the hydraulic rebound stopper system was mounted inside the adjustable shock absorber located in Maysan Mando R&D Center for testing. The shock absorber, which was mounted and connected to the test device, required certain speeds to be entered in the test device for measurement. These speeds are as in Figure 9.

0.52 m/s 0.39 m/s 0.26 m/s 0.13 m/s 0.05 m/s
--

Figure 9. Measurement Value Of HRS

The measurement to be made on the Test Device measures the damping that occurs according to the speed difference at the lower and upper points of the shock absorber. The soft or hard shock absorber is measured by the forces obtained from here. Since the hydraulic rebound stopper system is adjustable according to the vehicle, it can be adapted to every vehicle. The force measurement values of the shock absorber without hydraulic rebound stopper are in Figure 10.

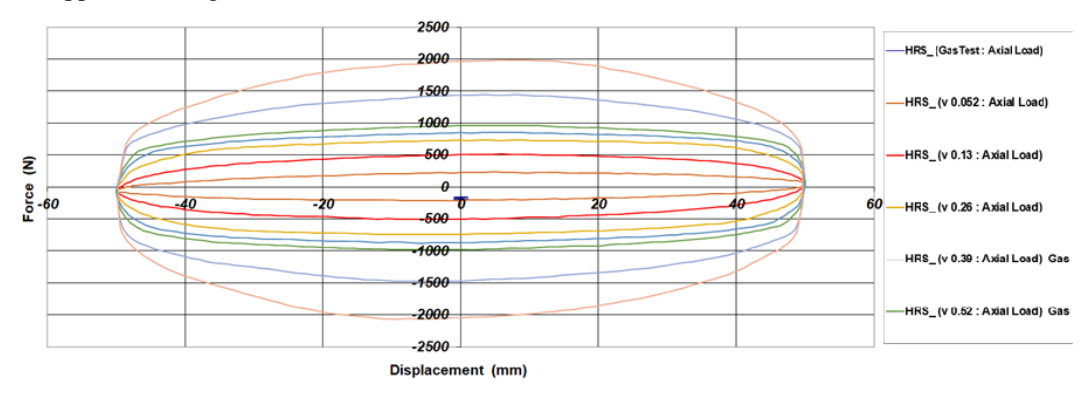


Figure 10. Damping Force Chart Without HRS

As seen in Figure 10, no additional damping force is obtained in the shock absorber without hrs. The graph of the measurement made with the test device also provides this. Shock absorbers in this form can transfer disturbing impacts to the chassis in very hard-entered holes.

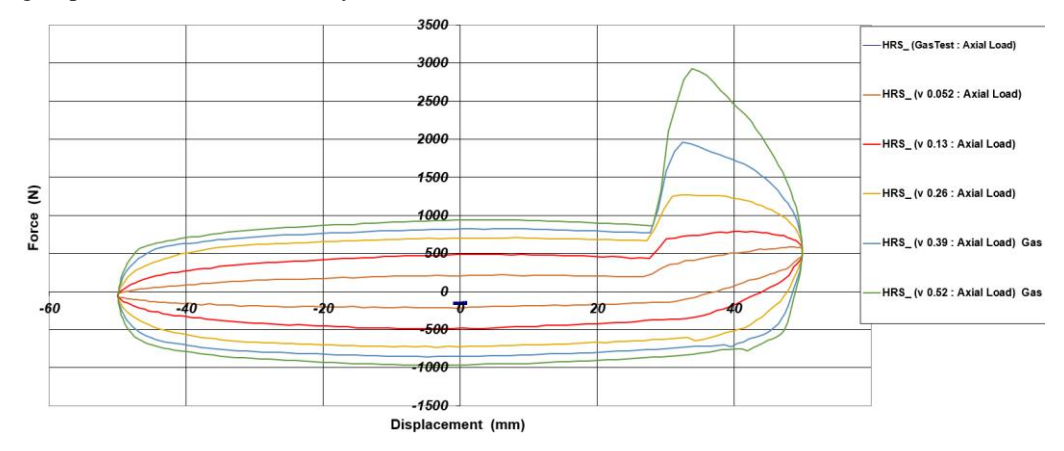


Figure 11. Damping Force Chart With HRS Setup 1

74 Calli

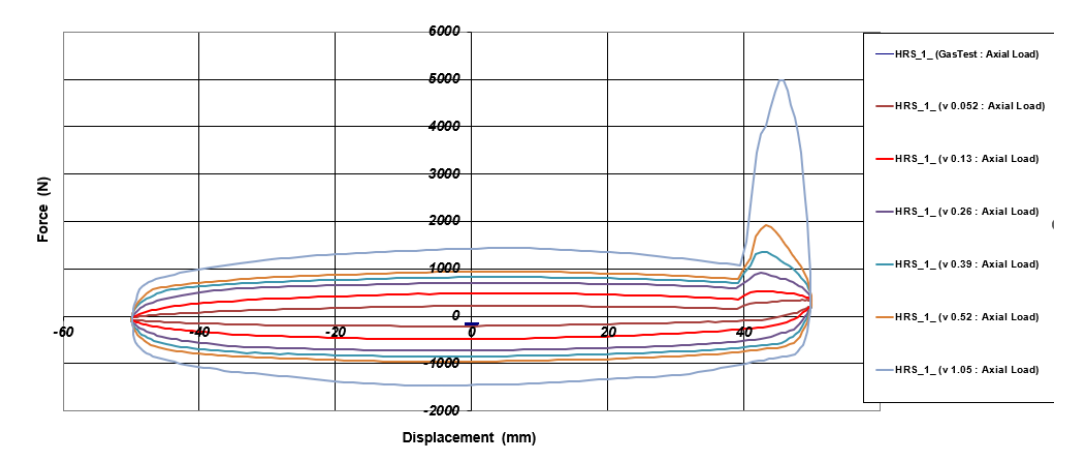


Figure 12. Damping Force Chart With HRS Setup 2

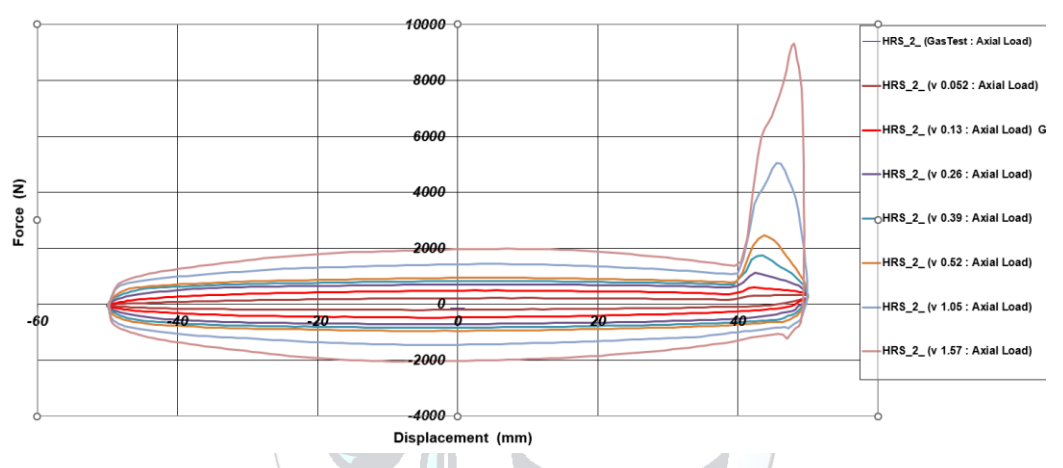


Figure 13. Damping Force Chart With HRS Setup 3

However, when we mount the hydraulic rebound stopper system we developed into the adjustable shock absorber, the effect of this technology on the shock absorber is revealed as a result of measurements. When we assembled the shock absorber with hydraulic rebound stopper to the test device, the force graph given by the test device is given in Figure 11. The additional damping force that appears in this graph occurs when the shock absorber starts to close. The graph, which normally does not create an additional force, creates an additional damping force at variable speeds when it starts to work with the addition of the hydraulic rebound stopper system. It works regardless of the operating speed of the shock absorber with this additional damping force. The height at which hydraulic rebound stopper is activated from the moment the vehicle starts to fall into the pithole. In addition, as seen in Figure-12-13, it has been observed that the adjustable hydraulic rebound stopper system can be obtained with variable forces in different tests.

4. CONCLUSIONS

In this study, the shock absorber can produce additional damping force during operation with the developed hydraulic rebound stopper. With these improvements, the newly developed system works and the benefits it provides to the vehicle have been determined in this study. According to the results obtained from the test device, the maximum rebound force that can be obtained without a hydraulic rebound stopper in the shock absorber is approximately 2500 N, while after the hydraulic rebound stopper is added, the maximum rebound force can be obtained from the same sample shock absorber up to approximately 10000 N. However, another advantage of the system is that this maximum force can be adjusted. The maximum force can be limited between 3000 N and 10000 N. In the 1st setup, the hrs channel height is 0.2mm and the maximum force received is 3000N. In the 2nd setup, the hrs channel height is 0.6mm and the maximum force received is 6000N. In the 3rd setup, the hrs channel height is 1mm and the maximum force received is 10000N. This allows the system to exhibit optimum performance in different vehicles. The newly designed hydraulic rebound stopper system was mounted on the vehicle with the results in the test device and this vehicle was tested dynamically on the roads. When the physical effects on the vehicle were examined after the test, a more comfortable and rigid ride was

obtained. The shock absorber, which works together with the hydraulic rebound stopper system that is activated when the vehicle enters a pothole, reduces the vibrations coming from the potholes that the vehicle enters at high or low speeds, together with comfort, and creates a more dynamic ride. The parts used in the hydraulic recoil stopper have reduced the sounds transmitted from the shock absorber to the chassis.

The forces that emerge with the additional damping prove that this system can also be used in new types of electric vehicles. Since the secondary damping force will be sufficient for heavier vehicles, it has made it possible to integrate it into vehicles with increased weight together with the battery.

REFERENCES

[1]. Robert N., (2017), "Shock absorber and vehicle", SAE International 2009-01-0223.



Optimizing Energy Efficiency in Urban 5G Wireless Communication Systems

Bünyamin Hatipoğlu^{1*}, Tayfun Acarer²

¹Istanbul Sabahattin Zaim University, Graduate Education Institute, Computer Science and Engineering, 34303, Küçükçekmece / İSTANBUL, TÜRKİYE.

² Piri Reis University, Maritime Transportation and Management Vocational School of Higher Education, Tuzla / İSTANBUL, TÜRKİYE

*Corresponding Author email: hatipoglu.bunyamin@std.izu.edu.tr

Abstract

The deployment of 5G technology in urban environments is recognised as a significant opportunity to revolutionise wireless communication across various sectors. This paper investigates strategies for optimising energy efficiency within urban 5G networks, emphasising the utilisation of beamforming technology and advanced antenna configurations. The impact of system parameters such as transmitter power levels, carrier frequencies, antenna heights, and construction materials on energy consumption and signal propagation is explored through comprehensive numerical results and scenariobased simulations. The findings reveal substantial signal attenuation and path loss variations across different frequencies, antenna heights, and materials. Moreover, they demonstrate the critical role of beamforming in enhancing signal propagation and reducing energy consumption through directed transmissions. The adoption of beamforming techniques not only minimises interference but also enables higher data rates, thereby improving network efficiency. The research identifies optimal deployment strategies, including selecting appropriate antenna parameters and integrating beamforming technologies. These strategies lead to significant improvements in energy efficiency within 5G networks operating in urban environments, offering practical solutions for network design and deployment efforts. This research paves the way for the seamless integration of 5G technology into urban infrastructures. This research significantly contributes to the growing knowledge of optimising 5G wireless communication systems in urban settings. By prioritising energy efficiency and leveraging advanced technologies such as beamforming, stakeholders in the field are empowered to harness the transformative potential of 5G. This research helps meet the evolving communication needs of urban populations while minimising environmental impact, a crucial consideration in today's world.

Keywords

Antenna Heights, Beam Steering, Frequencies, Material Types, Optimization, Wireless Communication

1. INTRODUCTION

The evolution of wireless communication technologies has continually reshaped the global connectivity landscape, enabling ubiquitous access to information and services across diverse sectors. Among these advancements, fifthgeneration (5G) wireless technology stands out for its promise of unprecedented speed, reliability, and

capacity. With the potential to revolutionize various aspects of daily life, from healthcare to entertainment and industrial production, 5G represents a pivotal milestone in telecommunications infrastructure. The deployment of 5G networks is supported by efforts from regulatory bodies and international organizations, such as the Federal Communications Commission (FCC) spectrum auctions [1] and determinations made by the World Radio Communications Conference 2019 (WRC19) [2].

Operating across a spectrum ranging from below 1 GHz to millimeter wave (mmWave) frequencies, 5G technology offers diverse possibilities, each with its tradeoffs between signal coverage and data capacity. Leveraging multipleinput, multipleoutput (MIMO) antenna technology, 5G user equipment can handle the complexities of mmWave frequencies, facilitating efficient data transmission and reception. Additionally, 5G deployment requires a shift towards smaller microcells, complementing traditional macro cell towers to provide seamless ultrahighspeed network coverage. Central to the efficacy of 5G deployment is beamforming technology, which enables targeted and efficient signal transmission by directing energy towards specific directions, thus minimizing interference and maximizing network performance.

However, deploying 5G networks in urban environments presents unique challenges. Densely populated urban landscapes pose obstacles such as high signal reflection and absorption, limited space for antenna installations, and complex propagation dynamics influenced by the surrounding environment. Understanding the interplay between system parameters such as transmitter power levels, carrier frequencies, antenna heights, and materials is crucial for optimizing energy efficiency and ensuring seamless 5G deployment in urban areas.

This paper aims to elucidate the dynamics of 5G deployment in urban environments, with a focus on optimizing energy consumption. Through numerical simulations and insights from existing research in wireless communication systems and urban network optimization, we seek to identify optimal deployment strategies and antenna configurations for energyefficient 5G networks. In subsequent sections, we delve into our analysis methodology, present our findings, and discuss the implications of our research. By offering actionable insights for network engineers, policymakers, and stakeholders, this study contributes to the advancement of sustainable, highperformance communication systems in urban environments, ushering in a new era of connectivity and innovation.

1.1. Motivation

Urban environments demand efficient 5G deployment strategies to handle dense populations and complex infrastructures. Understanding the interaction of various system parameters is essential for optimizing energy consumption and network performance. This research aims to bridge the gap between theoretical 5G concepts and practical urban implementation, addressing the growing need for highspeed, energyefficient communication systems.

1.2. Our Main Contributions

Our study offers a comparative analysis of different 5G deployment scenarios to identify configurations that enhance energy efficiency and signal propagation. We also explore strategies to reduce energy consumption through advanced techniques like beamforming and optimized antenna designs. Additionally, we provide practical insights for network engineers, policymakers, and telecommunications firms, helping them implement effective and sustainable 5G solutions in urban settings. This research contributes to the development of smarter, more connected cities while aiming to minimize environmental impacts.

2. RELATED WORK

In the field of wireless communication optimization in urban environments, various studies have been carried out to solve the challenges posed by complex propagation environments such as signal attenuation due to buildings, reflections, and diffraction.

The purpose of the study in [3] is to assess the accuracy of estimating radio coverage in 5G networks during the early deployment phase, which is crucial for effective network planning and optimization. The research examines the suitability of various path loss models and a new beamforming antenna model across different scenarios, including outdoor and indoor environments. The purpose of the proposed optimization algorithm in [4] is to address the challenge of energy consumption efficiency in the context of 5G mobile cellular networks. By maximizing energy efficiency through dynamic power allocation, the algorithm aims to enhance the performance of both indoor and outdoor users under various network conditions. The purpose of the survey in [5] is to examine the evolving landscape of energyefficient wireless communications, emphasizing its growing significance in the context of modern communication networks. It aims to provide a comprehensive overview of the field, including seminal and recent contributions, while also discussing the emerging challenges that researchers and practitioners need to address. The research in [6] proposes a methodology for designing green policies to manage the network

effectively, selecting operating points that balance energy efficiency and network performance. The research in [7] aims to optimize energy efficiency and coverage.

Through the lens of mean field game theory, the study focuses on maximizing the weighted energy efficiency of the BSs as a primary performance metric. The paper in [8] aims to reduce system power consumption and improve EE performance. Ultimately, the goal is to contribute to the advancement of energyefficient 5G IoT systems through integrated optimization strategies. The paper in [9] surveys recent research efforts focusing on enhancing the energy efficiency of both radio access and core networks in wireless communication systems. It explores various optimization avenues, including game theory and machine learning techniques, while also discussing challenges and open issues in the field.

These studies provide valuable insights and methodologies for optimizing wireless communication systems in urban environments. They address various aspects such as antenna deployment, power control, frequency selection, interference management, and energy efficiency, contributing to the advancement of urban wireless networks. Wireless communication systems are susceptible to signal attenuation caused by reflection and diffraction, particularly in environments with obstacles and varying material properties. Numerous studies have investigated the impact of these phenomena on communication performance and proposed various optimization techniques to mitigate their effects.

3. SYSTEM MODEL AND PROBLEM DEFINITION

The system model involves wireless communications in urban environments using isotropic antennas operating at various carrier frequencies. The system model comprises transmitter characteristics such as power levels (5W, 10W, 20W) and antenna height (10m, 2m, 8m), receiver characteristics including antenna heights (1m, 2m, 4m, 8m), frequency bands (2.5 GHz, 3.5 GHz, 3.7 GHz, 4.2 GHz, 5.5 GHz, 24 GHz, 28 GHz, 36 GHz, 37 GHz, 39 GHz, 47 GHz), and factors affecting propagation like reflection, diffraction, beam steering, and various obstacles such as concrete, metal, glass, wood, and brick, with the problem definition focused on assessing received signal strength at different receiver antenna heights while considering the impact of transmitter power, antenna height, frequency, obstacles, and beam steering effects.

3.1 Objective

The objective is to minimize signal attenuation, which refers to the reduction in signal strength as it propagates through a medium or encounters obstacles. Signal attenuation can occur due to various factors such as path loss, reflection, diffraction, and absorption. Minimizing signal attenuation is crucial for maintaining reliable communication links and maximizing coverage in wireless communication systems.

3.2 Problem Definition: (Mathematical Definition)

The problem aims to minimize signal attenuation in a communication system. Given specific parameters such as transmitter power, antenna heights, frequency band, reflection, diffraction, distance between antennas, building material, and path loss, the goal is to calculate the received power using the Friis Transmission Formula. Additionally, considering zero antenna gains for both transmitter and receiver antennas simplifies the calculation.

(2)

Lfs =
$$20 \log_{10}[6]$$
 [(($4\pi df$)/c)] Where:

$$d = 111 \text{ m (Distance between transmitter and receiver antennas)}$$

$$f = 24 \text{ GHz}$$

$$c = 3 \text{ [} x 10 \text{] } ^8 \text{ m/s (Speed of light)}$$

$$Lfs = 20 \log_{10}[6] \text{ [} ((4\pi \text{ x } 111 \text{ x } 24 \text{ x } \text{ [} 10 \text{] } ^9)/(3 \text{ x } \text{ [} 10 \text{] } ^8 \text{))} \text{]}$$

$$Lfs \approx 20 \log_{10}[6] \text{ [} (2960) \text{]}$$

$$Lfs \approx 20 \text{ x } 3.471$$

$$Lfs \approx 69.42$$
Applied and calculated Lfs as Eq. 2.
$$Lother = 2 \text{ dB}$$

Pr = 37 dBm + Gt + Gr - 69.42 dB - 2 dB

When an isotropic antenna is used, antenna gains are given as 0 dBi for both transmitting and receiving antennas.

Pr = 37 dBm - 69.42 dB - 2 dB

Pr = 34.42 dBm

The result is the received power expressed in dBm, which indicates the effectiveness of the communication link in terms of signal strength.

4. MATERIALS AND METHODS

In this study, we utilized an OpenStreetMap (.osm) file of Beyazıt Square in Istanbul to extract building information, which was visualized using Site Viewer. Small Cell Transmitter and Receiver were positioned at specified coordinates, equipped with isotropic antennas, and operated across various carrier frequencies. The impact of transmitter antenna height variations on signal reception was investigated by altering receiver antenna heights. Path losses for signal transmission and reception were computed using the ray tracing propagation model, considering interactions with building materials such as concrete, brick, wood, glass, metal, and perfect electrical conductors. The .osm file corresponding to Beyazıt Square in Istanbul was obtained from OpenStreetMap [10]. The building information extracted from the OpenStreetMap file was transferred to Site Viewer for visualization as shown in Fig. 1.



Figure 1. OpenStreetMap (.osm) file corresponding to Beyazıt Square in Istanbul

4.1. Configuration

The Small Cell Transmitter is equipped with isotropic antennas. It operates across various carrier frequencies: 2.5 GHz, 3.5 GHz, 3.7 GHz, 4.2 GHz, 5.5 GHz, 24 GHz, 28 GHz, 36 GHz, 37 GHz, 39 GHz, and 47 GHz. Transmitter power levels of 5 W, 10 W, and 20 W are considered. Different transmitter antenna heights are evaluated for their impact on signal propagation. Small Cell Transmitter is located at a latitude 41.00920 and Longitude 28.96668 is given by Table 1.

The Small Cell Receiver is located at Latitude 41.008871 and Longitude 28.967746. Receiver antenna heights are varied to observe their effects on signal reception.

Ray tracing propagation model using the shooting and bouncing rays (SBR) method is employed. The SBR propagation model uses ray tracing analysis to compute propagation paths and their corresponding path losses. Path losses are calculated considering freespace loss, reflection, diffraction, and antenna polarization loss.

Buildings in the area are characterized by surface materials, including concrete, brick, wood, glass, metal, and perfect electrical conductor. The influence of these materials on signal propagation is taken into account.

The Small Cell Receiver is located at Latitude 41.008871 and Longitude 28.967746. Receiver antenna heights are varied to observe their effects on signal reception.

Ray tracing propagation model using the shooting and bouncing rays (SBR) method is employed. The SBR propagation model uses ray tracing analysis to compute propagation paths and their corresponding path losses. Path losses are calculated considering freespace loss, reflection, diffraction, and antenna polarization loss.

Buildings in the area are characterized by surface materials, including concrete, brick, wood, glass, metal, and perfect electrical conductor. The influence of these materials on signal propagation is taken into account.

Table 1. Sample Output for Small Cell Transmitter

Key	Value
Name	Small Cell Trransmitter
Coordinate System	geographic
Latitude	41.0092
Longitude	28.9667
Antenna	isotropic
Antenna Angle	0
Antenna Height	10
System Loss	0
Transmitter Frequency	4.70E+10
Transmitter Power	10

Beam steering and the Phased Array System ToolboxTM along with MATLAB R2023b Academic use are employed for optimizing a nonlineofsight link. The optimization process aims to enhance signal quality and reliability under various environmental conditions and constraints.

The Received signal strength method in the MATLAB R2023b application was used for the calculation. This method returns the signal strength at receiver site RX due to transmitter site TX with the Propagation Model argument.

A coverage map is generated for a maximum range of 250 meters from the base station. Received power for ground locations within the coverage area is depicted on the map as shown in Fig. 2. The coverage map shows received power for a receiver at each ground location, but the received power is not computed for building tops or sides. Signal strengths between 120 and 5.



Figure 2. A coverage map that includes maximum number of reflections to 0. The building and terrain material types to model perfect electrical conductors (Latitude 41.00920; Longitude 28.96668)

A Transmitter Site was created using an isotropic antenna at 41.00920 Latitude and 28.96668 Longitude, Transmitter Power 5 W, Transmitter antenna height 10 m and Carrier Frequency 24 GHz.

The ray tracing propagation model was prepared using the sbr method, entering the maximum number of reflections, and also entering "perfectreflector" as Buildings Material and Terrain Material.

A Receiver Site with an antenna height of 1 m was created, similar to the Transmitter Site, at 41.008871 Latitude and 28.967746 Longitude.Later, the model was updated to Maximum Number of Reflections 1, Buildings Material and Terrain Material are "concrete". Later, the model was updated to Maximum Number of Reflections 1, Buildings Material and Terrain Material are "concrete" and Received power using concrete materials was calculated as 72.0665 dBm. By adding weather impairments to the propagation model and recalculating the received power and including weather loss, it was calculated as 72.7397 dBm.

The remarkable result here is that applying maximum number of reflections to 1 and maximum number of diffractions to 0. Define a custom antenna from Report [11], create an 8by8 uniform rectangular array and Use Beam Steering to Enhance Received Power. Received power with beam steering was calculated as 51.2664 dBm.

5. NUMERICAL RESULTS

In this section, numerical findings obtained according to 5G network deployment scenarios in urban environments are presented. Numerical results are organized according to different system parameters and their effects on energy efficiency.

The following study is given as an example and concrete is used as terrain material. The transmitter uses the default isotropic antenna and operates at a carrier frequency of 2.5 GHz with a power level of 5 W and antenna height 10 m. Some results are given as examples when the receiver antenna height is 1m and One Reflection is used, using various materials are given by Table 2. The resulting Received power is given in dBm.

 Material
 Value

 Perfect Reflector
 44.3644

 Brick
 54.0574

 Wood
 56.7979

 Glass
 51.7739

 Metal
 44.3662

 Concrete
 52.3975

Table 2. The results obtained using various materials are given in Received power dBm.

Additionally, when concrete was used as the material, 52.3991 dBm Received Power was obtained by including Weather loss. In addition, 51.1294 dBm Received Power was obtained in the case of Two Reflections and 52.4327 dBm in the case of Two Reflections and One Diffraction. when beam steering was applied, a Received Power of 30.9259 dBm was obtained in the case of One Reflection, 29.6805 dBm in the case of Two Reflections and 38.1374 dBm in the case of Two Reflections and One Diffraction. Finally, when concrete was used as the material, 52.5507 dBm Received Power was obtained by including Weather loss. In addition, 49.2416 dBm Received Power was obtained in the case of Two Reflections and 47.7694 dBm in the case of Two Reflections and One Diffraction. When beam steering was applied, a Received Power of 31.0514 dBm was obtained in the case of One Reflection, 28.2445 dBm in the case of Two Reflections and 34.4212 dBm in the case of Two Reflections and One Diffraction.

The remarkable result here is that after applying beam steering, there is a difference of approximately 3.7 dBm in the case of Two Reflections and One Diffraction.

In Table 3, we see that concrete has the lowest receiver power levels when used as a reflector. This shows that concrete can effectively manage signal reflections and propagation. In general, at higher frequencies (e.g. 24 GHz and above), receiver power levels are lower. This indicates that higher frequencies have greater barrier penetration and propagation loss. If the receiver antenna is high (4m), receiver power levels are generally low. This indicates

that higher antenna heights can improve transmission. Even at higher frequencies, receiver power levels are generally lower, but for frequencies of 24 GHz and above the difference is less pronounced.

Receiver power levels are generally lower when there is no Beam Steering effect. Generally, receiver power levels are lower at higher frequencies, indicating that higher frequencies have more propagation loss.

When there is a Beam Steering effect, receiver power levels generally increase. This ensures that the signal is directed more effectively into a targeted direction. Even at higher frequencies, receiver power levels generally increase due to the Beam Steering effect, but this increase will depend on the effectiveness of the Beam Steering and the characteristics of the medium used.

Beam steering refers to the ability to control the signal direction of antenna arrays. This parameter has significant effects on the received power. Beam steering provides the ability to control the signal propagation direction of antennas. This allows the signal to focus in a certain direction or avoid a certain direction. Directional antennas can enable the receiver to receive a stronger signal from a particular source. In this case, the received power increases. Additionally, beam steering can reduce interference and other signal distortions by targeting the signal in a specific direction, which can have a positive effect on the received power. Beam steering can reduce multipath effects by focusing the signal in a specific direction. This allows the receiver to receive a clearer signal and can increase the received power.

Table 3. Default isotropic antenna, and operates at a carrier frequency at any with a Transmitter power level of 5 W and antenna height 10 m. Receiver antenna height 1 m. Results in dBm (-)

			Freq	uencies	S								
Include Beam steering	Reflection and Diffraction	Building Materials	2.5 GHz	3.5 GHz	3.7 GHz	4.2 GHz	5.5 GHz	24 GHz	28 GHz	36 GHz	37 GHz	39 GHz	47 GHz
No	One Reflection	Perfect Reflector	44.36	47.28	47.76	48.87	51.21	64.00	65.34	67.53	67.76	68.22	69.84
No	One Reflection	Brick	54.05	57.00	57.48	58.59	60.94	73.74	75.08	77.27	77.50	77.96	79.58
No	One Reflection	Wood	56.79	59.71	60.20	61.30	63.64	76.43	77.77	79.95	80.19	80.64	82.26
No	One Reflection	Glass	51.77	54.69	55.17	56.27	58.62	71.41	72.75	74.93	75.17	75.63	77.25
No	One Reflection	Metal	44.36	47.28	47.77	48.87	51.21	64.01	65.35	67.53	67.77	68.23	69.85
No	One Reflection	Concrete	52.39	55.32	55.80	56.91	59.25	72.06	73.40	75.59	75.82	76.28	77.90
No	Two Reflections	Concrete	51.12	52.40	56.46	55.59	55.83	79.12	70.88	75.77	74.29	74.13	76.35
No	Two Reflections and One Diffraction	Concrete	52.43	50.62	55.69	57.06	56.98	79.07	71.08	73.65	73.99	75.15	76.11
Yes	One Reflection	Concrete	30.92	33.85	34.33	35.44	37.79	51.26	52.78	55.32	55.61	56.15	58.09
Yes	Two Reflections	Concrete	29.68	30.96	35.00	34.15	34.39	57.53	49.45	54.32	52.85	52.69	54.92
Yes	Two Reflections and One Diffraction	Concrete	38.13	37.25	40.09	43.45	42.04	64.75	57.43	59.55	60.03	61.32	62.78

Reflection and diffraction represent various media interactions during the propagation of electromagnetic waves. Both have significant effects on received power. Reflection is the reflection of the signal back when it encounters an obstacle. This allows the signal to reflect over the obstacle and reach the receiver. Reflection can increase the received power because the signal can reach the receiver via additional paths. This is especially important for buyers who are outside the direct line. However, reflection can sometimes cause multipath interference, which can cause interference and signal degradation problems at the receiver. Diffraction is the propagation of the signal

around the edges of obstacles. The signal refracted from the edge of the obstacle can reach the receiver. Diffraction often has an enhancing effect on the received power because it allows the signal to propagate around obstacles.

Lower frequencies generally have longer wavelengths, allowing them to penetrate obstacles better. This can cause the received power to increase because the signal can pass through obstacles more easily. Higher frequencies generally have shorter wavelengths and tend to interact with obstacles. This may reduce the received power because the signal may be further strained by obstacles. Increasing frequency generally results in increased propagation loss. That is, at higher frequencies, the signal may attenuate faster over distance. This may cause the received power to decrease. The effect of frequency is also related to the multipath effect. Higher frequencies generally experience more multipath effects, which can cause the received power to fluctuate. Lower frequencies can provide a more stable received power. Comparing the effect of Beam Steering on Received Power under current conditions reveals significant differences.

Shifting focus to the impact of Frequency bands on Received Power under similar conditions, with a Transmitter Power Level of 20W, Transmitter Antenna Height of 10m, Receiver Antenna Height of 1m, and concrete as the building material, it's evident that the 2.5 GHz frequency band yields higher received power (-46.3769 dBm) compared to the 28 GHz frequency band (-67.3858 dBm). This disparity can be attributed to the former's superior penetration through obstacles like concrete buildings and its lower susceptibility to attenuation. Furthermore, the lower frequency band is less affected by differences in antenna height between the transmitter and receiver. Consequently, the Frequency Band effect is approximately 21 dBm.

In conclusion, these numerical results offer valuable insights into the intricate dynamics of system parameters and energy savings in urban 5G deployments. Such insights are crucial for informing strategic decision-making processes and facilitating the development of efficient, sustainable communication systems tailored for the smart cities of the future.

6. DISCUSSION

Several academic studies have delved into optimizing wireless communication systems in urban environments, focusing on parameters such as transmitter power levels, carrier frequencies, antenna heights, and material properties.

Our study builds upon these researchs by incorporating additional factors such as carrier frequencies, material properties, and beam steering techniques to offer a comprehensive analysis of 5G network optimization. We propose optimization strategies to mitigate the adverse effects of material-induced attenuation. Our study aligns with these researchs by exploring the effectiveness of beam steering in reducing signal loss due to reflection and diffraction.

However, we provide a more comprehensive analysis by integrating beam steering with other optimization parameters such as antenna heights, frequencies, and material properties. While our study shares similar objectives in optimizing antenna heights, we expand upon these researchs by considering additional factors such as transmitter power levels, carrier frequencies, and material properties. By incorporating these variables, we provide a more holistic approach to network optimization in urban environments.

7. CONCLUSION

The study conducted in this paper sheds light on several critical aspects of 5G network deployment in urban environments.

Firstly, increasing transmitter power levels generally enhances signal strength and coverage, albeit at the cost of increased energy consumption.

Secondly, carrier frequencies significantly influence signal propagation characteristics, with higher frequencies offering higher data rates but being more susceptible to attenuation, particularly in urban settings with obstacles and interference.

Moreover, optimal antenna heights play a crucial role in signal propagation and coverage, especially in densely populated areas with tall buildings. Additionally, the choice of materials impacts signal attenuation, with materials like concrete exhibiting higher attenuation compared to others.

Energy-efficient communication strategies, such as beamforming and ray tracing, show promise in reducing energy consumption by optimizing signal transmission. As the receiver antenna height increases from 1m to 4m, the attenuation generally decreases across all frequencies and scenarios. This suggests that higher receiver antenna heights result in stronger received signals due to reduced obstruction.

Higher antenna heights may reduce the attenuation caused by obstacles such as buildings or terrain features, particularly in scenarios involving reflections and diffractions. Higher frequencies generally experience higher attenuation compared to lower frequencies. As the frequency increases, the attenuation tends to increase as well. This trend is observed for both antenna heights and is consistent with the behaviour of electromagnetic waves, where higher frequencies are more susceptible to absorption, scattering, and diffraction.

At each antenna height, higher frequencies (e.g., 24 GHz, 28 GHz, etc.) generally exhibit higher attenuation compared to lower frequencies (e.g., 2.5 GHz, 3.5 GHz, etc.). This demonstrates the frequency-dependent nature of signal attenuation in the given environment. The relative differences in attenuation between frequencies remain relatively consistent across antenna heights, indicating that the material properties of concrete have a consistent impact on signal attenuation across the frequency spectrum.

Materials like concrete and brick typically cause more attenuation compared to wood or glass. This analysis can provide insights into the suitability of materials for constructing structures in wireless communication environments. The number of reflections and diffractions also affects the attenuation values at different frequencies. Generally, more reflections and diffractions lead to higher attenuation, especially at higher frequencies where signals are more prone to scattering and absorption.

The comparison of deployment scenarios underscores the importance of considering multiple factors, including transmitter power levels, carrier frequencies, antenna heights, and materials, in designing and optimizing 5G networks in urban environments.

The findings of this study offer valuable insights that can inform strategic decision-making processes for network planning, deployment, and optimization, ultimately contributing to the development of sustainable and resilient communication systems for smart cities of the future.

Engineers can use this analysis to optimize antenna heights, select appropriate frequencies, select appropriate materials for infrastructure, and apply beam steering techniques to minimize losses and improve communications system performance. Through iterative analysis and optimization, engineers can fine-tune various parameters to achieve the desired balance between signal strength, coverage, and efficiency while minimizing losses.

CONFLICT OF INTEREST STATEMENT

The authors declare that there is no conflict of interest.

REFERENCES

- [1] Federal Communications Commission. (2024, March 1) America's 5G Future. FCC. https://www.fcc.gov/5G
- [2] ITU News. (2020, Jan 24). WRC-19 identifies additional frequency bands for 5G. https://www.itu.int/hub/2020/01/wrc-19-identifies-additional-frequency-bands-for-5g/
- [3] Sousa, M., Alves, A., Vieira, P., Queluz, M. P., & Rodrigues, A. (2021). Analysis and optimization of 5G coverage predictions using a beamforming antenna model and real drive test measurements. *IEEE Access*, 9, 168445-168457. https://doi.org/10.1109/ACCESS.2021.3097633
- [4] Smith, J., & Johnson, A. (2016). Optimizing the energy efficiency for future 5G networks. In *Proceedings of the 2016 International Conference on Systems, Signals and Image Processing (IWSSIP)* (pp. 100-110). IEEE. https://doi.org/10.1109/IWSSIP.2016.7502751
- [5] Buzzi, S., I, C.-L., Klein, T. E., Poor, H. V., Yang, C., & Zappone, A. (2016). A survey of energy-efficient techniques for 5G networks and challenges ahead. *IEEE Journal on Selected Areas in Communications*, 34(4), 697-709. https://doi.org/10.1109/JSAC.2016.2550338.
- [6] Salem, F. E., Tall, A., Altman, Z., & Gati, A. (2016). Energy consumption optimization in 5G networks using multilevel beamforming and large scale antenna systems. In *Proceedings of the 2016 IEEE Wireless Communications and Networking Conference* (WCNC) (pp. 1-6). IEEE. https://doi.org/10.1109/WCNC.2016.7564904.
- [7] Ge, X., Jia, H., Zhong, Y., Xiao, Y., Li, Y., & Vucetic, B. (2019). Energy efficient optimization of wireless-powered 5G full duplex cellular networks: A mean field game approach. *IEEE Transactions on Green Communications and Networking*, 3(2), 455-467. https://doi.org/10.1109/TGCN.2019.2904093.
- [8] Zhang, D., Zhou, Z., Mumtaz, S., Rodriguez, J., & Sato, T. (2016). One integrated energy efficiency proposal for 5G IoT communications. *IEEE Internet of Things Journal*, *3*(6), 1346-1354. https://doi.org/10.1109/JIOT.2016.2599852.
- [9] Usama, M., & Erol-Kantarci, M. (2019). A survey on recent trends and open issues in energy efficiency of 5G. *Sensors*, 19(14), 3126. https://doi.org/10.3390/s19143126
- [10] OpenStreetMap, "OpenStreetMap is built by a community of mappers that contribute and maintain data", 2024. https://www.openstreetmap.org

- [11] Report ITU-R M.2412, "Guidelines for evaluation of radio interface technologies for IMT-2020", 2017. https://www.itu.int/pub/R-REP-M.2412
- [12] Andrews, J. G., Buzzi, S., Choi, W., Hanly, S. V., Lozano, A., Soong, A. C. K., & Zhang, J. C. (2014). What will 5G be? *IEEE Journal on Selected Areas in Communications*, 32(6), 1065-1082. https://doi.org/10.1109/JSAC.2014.2328098
- [13] MacCartney, G. R., Jr., Sun, S., Rappaport, T. S., Xing, Y., Yan, H., Koka, J., Wang, R., & Yu, D. (2016). Millimeter wave wireless communications: New results for rural connectivity. *ACM Transactions on Wireless Networking*, 12(2), 1-25. https://doi.org/10.1145/2980055.2987353
- [14] Hoydis, J., ten Brink, S., & Debbah, M. (2013). Massive MIMO in the UL/DL of cellular networks: How many antennas do we need? *IEEE Journal on Selected Areas in Communications*, 31(2), 160-171.
- [15] Rappaport, T. S. (2002). *Wireless communications: Principles and practice* (2nd ed.). Horizon House Publications, Inc. Originally published in *Microwave Journal*, 45(12).
- [16] Rappaport, T. S., Sun, S., Mayzus, R., Zhao, H., Azar, Y., Wang, K., Wong, G. N., Schulz, J. K., Samimi, M., & Gutierrez, F. (2013). Millimeter wave mobile communications for 5G cellular: It will work! *IEEE Access*, 1, 335-349. https://doi.org/10.1109/ACCESS.2013.2260813
- [17] Boccardi, Federico, Raffaele Heath, Alan Lozano, Thomas L. Marzetta, and Petar Popovski. "Five disruptive technology directions for 5G." IEEE Communications Magazine 52, no. 2 (2014): 74-80.
- [18] Cakir, S., Ferguson, S., Sen, O., & Acarer, T. (2020). New Verification Methods for Low-Frequency Susceptibility Testing. Paper presented at the 2020 International Symposium on Electromagnetic Compatibility EMC EUROPE.
- [19] Acarer, T. (2023). "Yeni Nesil Mobil İletişim Sistemlerinin Gemi Kara Arasındaki Deniz Haberleşmesinde Kullanım Olanağı." Yıl 2023, Cilt: 6, Sayı: 1, 139-154.
- [20] Ucan, O. N., Acarer, T., Karacuha, E., Osman, O., Altay, G., & Yalcin, Ş. (2008). "Performance of the Systematic Distance-4 Codes Over Fading Channels." Istanbul University Journal of Electrical & Electronics Engineering, 8(2), 707-713.